TÉCNICO LISBOA

Integration and Testing of a Hydrogen Fuel Cell in a Hybrid Electric Propulsion System

Luís Miguel Martins Costa e Silva

Thesis to obtain the Master of Science Degree in

Aerospace Engineering

Supervisors: Prof. Afzal Suleman
Prof. Frederico José Prata Rente Reis Afonso

Examination Committee

Chairperson: Prof. Filipe Szolnoky Ramos Pinto Cunha
Supervisor: Prof. Frederico José Prata Rente Reis Afonso
Member of the Committee: Prof. Francisco Miguel Ribeiro Proença Brójo

December 2022

Acknowledgements

I would like to thank Prof. Afzal Suleman for providing me with the opportunity to work on this project for my thesis, and for working as my supervisor throughout this whole process. With this project I was given the chance to study new and exciting topics, and develop practical skills, which I had not had the chance to use before on my degree, constituting an ideal way to complete this cycle of my life. I also have to thank my co-supervisor, Prof. Frederico Afonso, who constantly offered his precious help, reading and re-reading this document several times, and whose feedback was invaluable to the completion of this work.

Furthermore, I would like to thank the University of Victoria Centre for Aerospace Research (UVIC-CfAR) for welcoming me in their workshop to do this project, and providing all the necessary space and resources to make this a successful journey. A particular note of gratitude goes to Jay Matlock, with whom I worked more directly, and whose work was, and is, essential for this hybrid project to exist and keep being developed. Despite his particularly tight work schedule, he always found the time to offer his assistance and guidance, and whose positive outlook and genuine interest in the project kept us all motivated. I have to extend my thanks to the other team members working at CfAR, all of whom directly or indirectly helped me with my project during these past few months, and who made going to work everyday an enjoyable experience.

I also have to thank my amazing friends, the ones who stayed back in Portugal after keeping me company during all these university years, the ones who I met in Victoria and made the time there more memorable, and, especially, the ones that accompanied me in every step of this journey and with whom I had the pleasure to share all the good, and not so good, moments these months had to offer. Thank you Carolina, Inês, António, João, and João.

Finally, last but by no means least, a special thank you to my family, who always gave me the support and encouragement to keep going, and the strength necessary to achieve my goals. To my parents, who saw their son go ten thousand kilometers away for a second time, with nothing but a smile on their faces and love on their hearts.

Thank you all, this would not have been possible without you.

Abstract

With the increasing environmental concerns and regulations, the aviation sector strives to find more sustainable propulsion alternatives. Hybrid electric propulsion systems and hydrogen as an energy source have been proposed as some potential solutions.

Hybrid electric propulsion systems can offer greater efficiency and reduce the amount of fuel burnt, while hydrogen could be a carbon-free energy-dense alternative to fossil fuels. Naturally, there are issues with its implementation in aircraft, and thus the research into these topics is of considerable importance.

This thesis studies the use of a hydrogen fuel cell as a power source for propulsion of unmanned aerial vehicle (UAV). A proton exchange membrane fuel cell system, with a 24-cell stack, was supplied with a compressed hydrogen gas cylinder, to generate electricity under different operating conditions. Its two operation modes were tested to power several different electric motors, with particular emphasis on UAV applications.

A parallel hybrid test bench, composed of two electric motors mechanically coupled, was used to compare the performance of the hydrogen fuel cell with Lithium-Polymer batteries. The performance metrics include the hybridization factor, different throttle signals and system loadings.

Keywords: hybrid electric propulsion, hydrogen fuel cell, unmanned aerial vehicles, proton exchange membrane fuel cell, parallel hybrid configuration

Resumo

Com o aumento das preocupações e regulamentações ambientais, o setor da aviação procura alternativas de propulsão mais sustentáveis. Sistemas de propulsão híbrido-elétricos e sistemas com o hidrogénio enquanto fonte de energia têm sido propostos como possíveis soluções.

Estes pretendem responder às limitações da propulsão elétrica alimentada a baterias, enquanto mantêm alguns dos benefícios destas últimas. Os sistemas híbridos podem permitir uma maior eficiência e reduzir a quantidade de combustível gasto, enquanto que o hidrogénio pode ser uma alternativa aos combustíveis fósseis, por ter uma densidade energética específica mais elevada e não emitir dióxido de carbono. No entanto, a integração destas soluções em aeronaves enfrenta diversos problemas e como tal deve ser foco de investigação.

Visando este objetivo, neste trabalho foi estudada uma célula de combustível com membrana de troca de protões alimentada a hidrogénio para a propulsão de veículos aéreos não tripulados (VANTs). A célula de combustível é constituída por 24 células e o hidrogénio é armazenado num tanque de gás comprimido. Os seus dois modos de operação foram testados para diferentes condições, e foi usada para alimentar vários motores elétricos diferentes, semelhantes aos encontrados em pequenos VANTs.

Esta célula de combustível foi ainda integrada num sistema propulsivo híbrido-elétrico em paralelo conjuntamente com uma bateria de lítio-polímero, no qual dois motores elétricos são acoplados mecanicamente. Vários parâmetros foram analisados de forma a aferir o desempenho do sistema híbrido-elétrico numa bancada de ensaios.

Palavras-Chave: propulsão híbrida-elétrica, célula de combustível de hidrogénio, veículos aéreos não tripulados, célula de combustível com membrana de troca de protões, configuração híbrida em paralelo

Contents

List of Tables

List of Figures

Nomenclature

Greek symbols

ΔH_f^0	Enthalpy of formation.
η_{el}	Electrical efficiency.
σ	Error.
ω	Rotational speed.

Roman symbols

I	Current.
K_v	Motor velocity constant.
$MTOM$	Maximum take-off mass.
$\dot{n}$	Molar flow rate.
P	Power.
p	Pressure.
Q	Torque.
$\overline{R}$	Perfect gas constant.
R	Electrical resistance.
T	Temperature.
U, V	Voltage.
$\dot{V}$	Volumetric flow rate.
w	Function of independent variables (x, y, z, ...).

Subscripts

0	No load.
A	Hybrid test bench side A.
B	Hybrid test bench side B.
m	Motor.
nom	Nominal.

Acronyms

AC alternating current. 22

APU auxiliary power unit. 17

BLDC brushless direct current. 23, 24

CfAR University of Victoria - Centre for Aerospace Research. 3, 4, 8, 20, 26, 30, 31, 33, 39, 40, 42, 58, 65

CO_2 carbon dioxide. 2, 10, 12

DC direct current. 22–25, 27, 55

DMFC direct methanol fuel cell. 11–13

EM electric motor. 2, 4, 8, 9, 15, 23–26, 39–42, 44–46, 48, 49, 51, 53, 55, 64, 65

EMF electromotive force. 25

ESC electronic speed controller. 24, 40–42, 44, 45, 49

FC fuel cell. 3, 4, 10–17, 22, 23, 29, 36, 39, 40, 45–47, 49, 51–54, 59–66

HEPS hybrid electric propulsion system. 2, 3, 7, 8

HEV hybrid electric vehicle. 7

ICAO International Civil Aviation Organization. 2

ICE internal combustion engine. 2, 3, 7–9, 15, 64, 65

ISR Intelligence, Surveillance and Reconnaissance. 7

LiPo Lithium Polymer Battery. 40, 42, 47, 49, 56, 60, 64

MOSFET metal–oxide–semiconductor field-effect transistor. 24

NO_X nitrogen oxides. 2

PEMFC proton exchange membrane fuel cell. 11, 12, 15–17, 19

PWM pulse width modulation. 27, 40, 42, 48

RPK Revenue passenger kilometres, one RPK means that one passenger is carried on one kilometre. 1

RPM revolutions per minute. 25, 27, 40, 53, 54, 56

SOFC solid oxide fuel cell. 11, 12, 15, 17

UAV unmanned aerial vehicle. 2–4, 7–11, 13, 15–17, 23, 29, 51, 58–66

VI Virtual Instrument. 4, 27, 40, 49, 66

VTOL vertical take-off and landing. 59, 60

Chapter 1

Introduction

In this chapter, a summary of the hybrid electric propulsion topic is given. The motivation behind this new type of propulsion system is explained, as well as the reason to include alternative power sources, such as hydrogen fuel cells, in aircraft. Keeping this overarching theme in mind, the thesis objective is described, alongside the methodology used during the experimental work.

1.1 Motivation and Overview

As the years pass, climate change and greenhouse gases emissions increasingly become a more pressing issue, with repercussions in all sides of daily life. As public awareness towards the issue grows, and political will shifts to more environmentally friendly policies and goals, the industrial world has to adapt. The aviation industry is by no means an exception in this need for change, and hybrid electric propulsion appears as part of the solution for this sector.

Globally, commercial aviation has experienced immense growth over the past decades (in 2019 the industry reached almost 8.7 billion revenue passenger kilometres (RPKs), while one decade before, in 2010, this number was just below 5 billion [1]), and it is expected to continue this path for the foreseeable future. Despite the toll taken by the aviation industry during the global pandemic, companies like Airbus still estimate that, until the year 2040, the global need for new aircraft is nearly 40,000, between those needed for replacements and to satisfy air traffic growth, with the total number of aircraft more than doubling (Figure 1.1a) [2]. This sustained growth presents itself as one more contributing factor to the global impact of this fossil-fuel-heavy industry. To counteract it, new configurations need to be further developed and implemented.

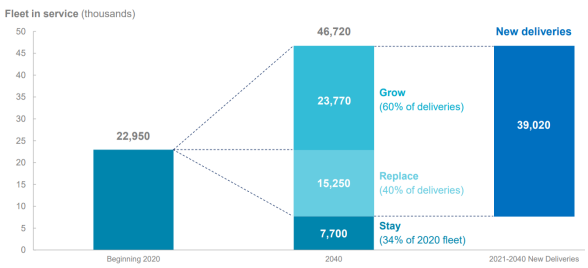

(a) Expected demand for large aircraft, until 2040 [2].

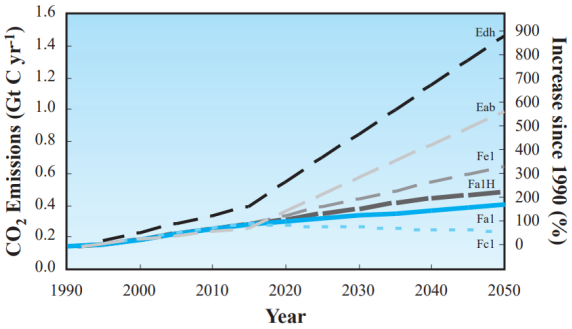

(b) Expected growth in CO_2 emissions from aviation, for different scenarios [3].

Figure 1.1: Forecasts for aircraft needs and CO_2 emissions.

The largest impact of aviation on the environment comes from atmospheric emissions of pollutant gases, in particular carbon dioxide (CO_2) and nitrogen oxides (NO_X). Carbon dioxide emissions are one of the main source for human-made climate change, and the aviation sector contributes significantly to emissions. By 1992 this sector already represented 2% of human emissions of this gas, and they are predicted to keep growing (Figure 1.1b). By 2010 it was the source of at least 3% of the total anthropogenic CO_2 emissions, showing a growth trend [4]. NO_X on the other hand is a pollutant that triggered the production of ozone, especially at the typical cruise altitude for modern aircraft [5]. Pollution emissions, besides their climate impact, also constitute a health hazard. An estimated 16 thousand premature deaths are caused annually. These can be mainly attributed to fine particles, $PM_{2.5}$, emitted during aircraft operation [6].

In light of these adverse byproducts of aviation, different entities have set targets to minimize or even reduce these negative impacts on the global climate. The International Civil Aviation Organization (ICAO) has the goal of achieving carbon neutral growth, from 2020 onward. The European Union has set the goal of reaching carbon neutrality in the region by 2050, and has passed regulations with the specific objective of curbing emissions in aviation [7][8].

Besides the evident environmental motivations for newer, more efficient propulsion systems, there are also clear financial incentives for airlines. By 2008, fuel costs accounted for just over 30% of airlines total expenses, after the increase in fuel prices [9]. As oil prices have gotten even higher, and are expected to remain expensive [10], and fossil fuel reserves shrink, these economic impulses will remain a push for greener aviation. Therefore, fuel efficiency has been, and will continue to be, one of the priorities of aircraft manufacturers, as they wish to remain competitive.

While the objective of the global research effort is the eventual application of more sustainable alternative propulsion systems in aircraft of all sizes, with the end-goal of tackling the most pollutant commercial aviation, unmanned aerial vehicles (UAVs) are of particular interest, before scaling up. Furthermore, the UAV market on its own has been rapidly growing, being expected to reach US$ 88.3 billion in the next decade [11]. Being unmanned, UAVs constitute a versatile and lower risk alternative to traditional aircraft, explaining their wide variety of applications. Given their multitude of possible missions, modern UAVs can range in size from small-scale aircraft, with less than 50 kg, to large and heavy vehicles, depending on their specific desired usage. They usually rely on either internal combustion engines (ICEs) or electric motors (EMs) propulsion systems.

With the goal of reducing emissions and saving fuel, hybrid electric propulsion systems constitute an attractive option being studied for eventual implementation in large-scale aircraft. A hybrid electric propulsion system (HEPS) refers to a system that draws power from two (or, potentially, more) different energy sources to generate the propulsive force for the aircraft, and at least one of them generates electrical power [12]. The objective is to combine the strengths of different types of propulsive systems, while minimizing their drawbacks.

For small aircraft and UAVs, a fully electric propulsion system, using an EM, presents a sensible solution to reduce emissions and achieve high efficiencies (commonly these can be as high as 96% [13]). It also offers other advantageous characteristics, such as low noise and vibration, low variation in operation with variables such as air temperature and density, and a high torque output over its operational range [14]. However, the drawbacks from electric-only propulsion usually stem from the energy storage - usually batteries. Due to the low energy density and specific energy of available batteries, there is a high weight penalty on the aircraft. This makes batteries uncompetitive with fossil fuels for long-range and high-endurance applications. In this types of long-range applications, thermal management can also become an issue, as large amounts of energy need to be dissipated. A purely fossil fuel-based solution, on the other hand, has disadvantages of their own. To begin with, it is the root of the problematic greenhouse gas emissions previously mentioned. Internal combustion engines, used in smaller aircraft and

UAVs, are also noisy and introduce vibrations in the system [14]. Despite using a more energy-dense fuel, which allows for a longer range and endurance, the efficiency of the engines are usually fairly low (even being theoretically limited to 40%, given thermodynamic considerations [15]). Also, given that the take-off and climb phases of the flight require a larger power, the ICEs tend to be oversized. This means that in the cruise and loiter phases, that take up most of the flight time, the engine being used is larger and heavier than necessary, because it had to be able to deliver more power in the previous flight phases, and it will be running in partial power most of the flight.

A HEPS aims to take advantage of each of these propulsion system strong points, by combining them. Therefore, the long endurance of an ICEs propulsion system during cruise can be achieved by an engine optimized for that flight phase, while the higher power demands during take-off and climb can be reached with the help of an EM.

In the context of hybrid propulsion research, one particular energy source that seems to have a lot of potential is hydrogen. This gas has a very high energy density, which makes it attractive as an alternative to fossil fuels since a small weight of hydrogen can store a lot of energy, an important aspect for aerospace applications. Being flammable, and very reactive, it can be burned directly with oxygen, or used in a fuel cell (FC) to produce electricity. This presents an alternative to traditional batteries for electricity-powered vehicles. This type of energy source comes across as a more environmentally friendly substitute for fossil fuels, as the product of the reaction with oxygen is just water, and hydrogen can be produced renewably from water as well. However, this type of energy source also present several challenges to its widespread implementation. Its low volumetric energy density in the gaseous state presents issues when it comes to onboard storage solutions. Besides, the production of renewable hydrogen is not yet economically competitive. These issues will need to be addressed for a successful utilization of this fuel in aviation, and justify the importance of further studying these technologies [16].

1.2 Objective

This project proposes to study the application of a fuel cell stack to power an UAV propulsion system, and its integration feasibility in a hybrid electric propulsion system. There is an existing hybrid propulsion test bench available at the University of Victoria - Centre for Aerospace Research (CfAR). The fuel cell stack apparatus was also available, and the objective of this research was to integrate and evaluate the fuel cell performance as an energy source for the propulsive system, and design and test a HEPS making use of the fuel cell.

The work attempts to answer the following questions:

- Can a FC stack effectively power a propulsion system for a small UAV?
- Can a FC stack bring advantages to a HEPS for a small UAV?
- What are the main challenges in implementing a FC stack in a small UAV?

To evaluate the effectiveness of the FC stack in powering the propulsion system, the total electrical power provided by the stack has to be quantified, and compared to batteries commonly used in UAVs. To adequately evaluate the performance and its advantages in a hybrid configuration, the mechanical power generated needs to be measured, and the hybridization factor in terms of power has to be evaluated.

1.3 Methodology

The procedures developed aimed to standardize the testing of the different systems, to ensure the validity of the results obtained and of the conclusions drawn.

First, the safety procedures for handling compressed gas cylinders had to be studied, and the cautions to have when using hydrogen in particular (a highly flammable gas) had to be thoroughly reviewed. Then, the test procedures could be written, following CfAR's guidelines, to ensure the correct execution of the experiments. They can be consulted in Appendix A. This made sure each test was performed in the same conditions, to allow for the results to be comparable. It also means that, in the future, the research work can be further developed, using the FC stack in similar test conditions.

The testing was conducted in separate phases, adding new elements in each stage. First only a programmable load was connected to the system, to measure its performance, and then different EMs were tested. Some adaptations had to be made to the system to allow for this, such as the integration of a diode in the wires connected to the fuel cell. Finally, the stack could be connected to a hybrid test bench, to verify the combination of power from different power sources. While the test bench itself had already been previously built, a dedicated LabVIEW Virtual Instrument (VI) had to be developed, lightly based on previous versions, to control the system and log data. This will also allow for easier testing with the system in the future.

1.4 Thesis Outline

When it comes to the organization of this document, there are the following chapters:

Chapter 1: Introduction Here a brief overview of the topic is presented, as well as the motivations behind it. The main objective of the developed project is described, and the methodology used is also explained. The current outline for the dissertation document is given, to disclose the contents of the different sections.

Chapter 2: Literature Review This chapter aims to present the current state of the art of both hybrid electric propulsion systems, and fuel cells in general. It covers topics from HEP system architectures, their application into aircraft, in particular UAVs, to the operating principles of fuel cells, their different types, and aviation applications.

Chapter 3: Experimental Setup In this chapter, each component used in the experimental test performed are presented. It goes through the different parts of the fuel cell system, and other necessary components for its operation, and the parts for the hybrid propulsion setup. Each component is identified, with their most relevant characteristics summarized. It also describes the integration of the fuel cell stack in a hybrid propulsion system, explaining the different considerations necessary for the design of this system, its configuration, and mode of operation.

Chapter 4: Experimental Tests The tests performed on the fuel cell are included in this chapter. This includes the experiments using only the fuel cell (and peripheral systems, necessary for its operation), with the intent of characterizing the FC stack performance before including it in a hybrid propulsion scheme, as well as the propulsion tests performed, before and after the hybrid architecture was implemented. The test procedures are briefly described, and the data gathered is briefly presented.

Chapter 5: Results Here, the results from the previous project are presented. The tests performed to confirm the hybrid system's function are explained, and the data gathered is reviewed. A brief analysis into aircraft integration is also included.

Chapter 6: Conclusion Given the work developed, and the results obtained, this chapters presents the conclusions drawn from this experimental study. It outlines how the objectives initially set were achieved, and proposes future work.

Chapter 2

Literature Review

In this chapter, a brief state of the art on HEPS is summarized, with a special focus on their application on UAVs. It intends to cover topics ranging from HEPS current usage, possible configurations, and operating modes.

Given the desire to use alternative energy sources to fossil fuels, and fuel cells in particular, in the hybrid system, this technology is also reviewed in detail. The objective is to frame the different types of fuel cells that exist and their working principle, as well as their current and intended applications in the aviation sector (again, with a special interest in unmanned aircraft), and other relevant aspects of their implementation, such as the issue of fuel storage on-board.

2.1 Hybrid Electric Propulsion

In general, any propulsion system that combines different energy types, including electricity, can be classified as a hybrid electric propulsion system. This first part focuses on aspects that combine an ICE with electrical power. This is because for UAV applications, this is the most relevant power combination to be studied. Another power source of interest is a fuel cell, which will be discussed later.

The use of hybrid electric systems to power vehicles has a long history of over 100 years, with early hybrid electric vehicle (HEV) designs being presented at the Paris Salon in 1899 [17]. These first vehicles already made use of the advantages of hybrid systems, by extending the power output or the range, when compared to a single power source. However, it took almost a century before HEVs became widely available, in the form of Japanese hybrid cars, the *Toyota Prius* (1997) and *Honda Insight* (1999) [18]. While this technology is more developed for these and other land vehicles, such as trucks and trains, there have been recent developments in the aviation industry.

In 2018 for example, Diamond Aircraft Industries and Siemens flew a multi-engine hybrid electric aircraft in Austria [19]. It used a series configuration (which will be described below) that allowed it to power two independent electric motors. Since 2019, Canada's National Research Council has been working to convert a Cessna 337 aircraft to use a hybrid propulsion system, with the first flight tests occurring in early 2022, flying for over half an hour [20][21].

As it was briefly discussed in the motivation of this work, hybrid propulsion systems are an attractive field of study for their promise to take advantage of the strongest points of different power sources, while minimizing their respective drawbacks. One good practical example of this is for military Intelligence, Surveillance and Reconnaissance (ISR) missions [18]. In these types of missions, the acoustic and thermal signature of combustion engines are largely incompatible with the need for the UAV to remain undetected. Therefore, for the ISR segment of the mission, electric propulsion is preferred. However,

the small endurance (and, therefore, range) of fully electrical UAVs is not ideal. A combination of both power sources can allow a stealthier operation when necessary, while having an improved range.

Naturally, these same advantages are relevant for civilian applications as well. At CfAR, UAVs with diverse goals, such as precision agriculture and magnetic anomaly sensors for submarine detection, are being developed [22][23]. Given the instrumentation used for data collection, it is necessary to keep vibrations of the system to a minimum, and electric propulsion presents a potential solution. A HEPS has the potential to increase the aircraft range, overcoming the primary limitation faced when only using batteries as a power source. More generally, the higher efficiency achieved by hybrid systems [18], reducing fuel burnt, and the redundancy they can provide, all contribute to its attractiveness for commercial aviation.

2.1.1 Hybrid System Architectures

There are several different ways to combine different power sources in a HEPS. There are essentially two distinct configurations, series and parallel, as well as combinations of the two approaches, the series-parallel configuration [24]. Their different strategies to combine different types of power are explained next.

Series Configuration

In a series configuration, there is no mechanical coupling between the ICE and EM. Instead, a generator makes the connection between the two, generating electricity from the ICE mechanical power, and feeding it to the EM (having the option to be stored in a battery). Only this latter is connected to the propeller which drives the aircraft. A schematic representation of these relations is represented in Figure 2.1.

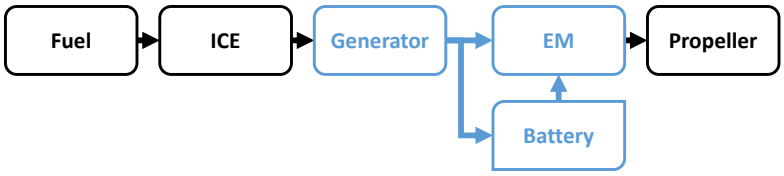

Figure 2.1: Series hybrid configuration.

By being mechanically decoupled from the propeller, the combustion engine can operate continuously in its most advantageous operating point. The simplicity of the system also means the propulsion control is easier than with other configurations [24]. However, the main disadvantages it presents lie in the added mass and the energy conversion losses. The need to satisfy peak power demands requires the system to have a large EM, as well as needing a second electrical machine, the generator, increasing the weight of the system. Besides, the fuel energy is converted several times, first into mechanical power, then to electricity, and then back into mechanical power to propel the aircraft. The successive conversion losses reduce the system overall efficiency [25].

One aspect of interest of a series hybrid configuration for aircraft propulsion is the possibility for distributed propulsion. This concept relies on a single ICE and generator, which can be located anywhere inside the aircraft, to generated electricity to power several EMs [26]. This is similar to what can be achieved with fully-electric propulsion, but with the added benefits of a hybrid configuration.

Parallel Configuration

A parallel configuration, depicted schematically in Figure 2.2, has the ICE and EM mechanically coupled. This connection allows for both to drive the propeller at the same time, with their torque being added by the coupling [24]. It may include one or more clutches, to disconnect one of the power sources, in case it is not being used.

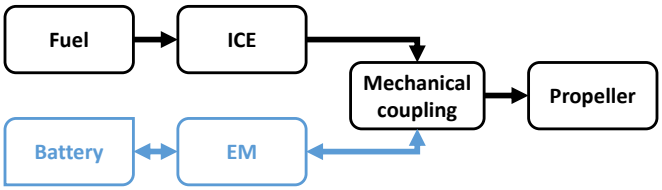

Figure 2.2: Parallel hybrid configuration.

The mechanical transmission in this configuration is more complex, and the controller design is not as simple. For example, it may not be possible to always operate the ICE at its most efficient point, as it is mechanically connected to the propeller [18]. However, this architecture can provide mass savings for the system. As the maximum power can be achieved by combining the motor and engine, they can both be downsized. Besides, the need for only one electrical machine (as opposed to the series configuration that has two) also reduces the total mass of the system. This reduction, for a 13.6 kg UAV was about 8% of the total mass, when compared to a series alternative [27]. The possibility of both power sources to drive the propeller independently also offers some redundancy to the system [24].

To address some of the drawbacks of such a configuration, particularly the difference in the ideal operating points for the ICE and propeller, a continuously variable transmission (CVT) can be implemented. Combined with an integrated engine controller, a greater level of freedom can be reached for selecting the engine operating point [28]. Once again, this comes at a cost of added complexity.

In a parallel hybrid system, distinct operating modes can be defined: ICE only, EM only, dash/hybrid, and regeneration mode.

As the name suggests, both ICE and EM only modes have a single power source driving the propeller, while the other is turned off. In case a clutch is present, the side not being used may be completely disconnected from the system. Otherwise, additional power will be consumed to rotate the inactive side [24].

During dash operation, both energy sources are combined, to achieve additional power. This mode has to be sized to fulfill the power requirements of the most demanding flight phases, such as take-off and climb. The regeneration mode also takes advantage of both energy sources, but this time it uses the ICE to charge the system's batteries, by using the EM as a generator, while also driving the propeller [24]. These capabilities can be used when the power required to generate thrust is lower than the optimal operating point of the ICE, thus using the extra power for onboard charging.

Series-Parallel Configuration

The series-parallel configuration, or power-split configuration, is essentially a combination of the two previous designs. Such a configuration is represented in Figure 2.3.

The electrical side, with two machines (generator and motor) and the ICE side are connected with a planetary gear, allowing for more flexibility in operation, with the engine being able to operate at its most efficient speed, regardless of the thrust requirements. It allows for the ICE to be disabled, without mechanically uncoupling it [24]. However, given the added mass and complexity of this configuration, it is not suitable for small UAV applications.

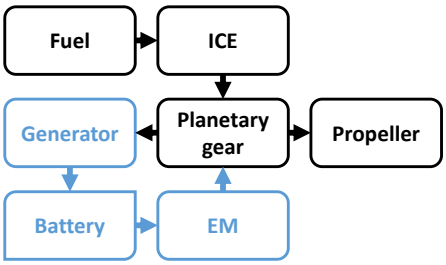

Figure 2.3: Series-parallel hybrid configuration.

2.2 Hydrogen Based Propulsion

Making use of hydrogen in aerospace applications is not a new concept. Initially, its very low density was used for balloons and airships, over one hundred years ago [29]. For many years, hydrogen has also been used in space applications. In particular, most rocket engines are powered making use of hydrogen as its fuel [30]. This makes use of the large amount of energy released during hydrogen reaction with oxygen, to generate the propulsive force. NASA has also made use of hydrogen fuel cells to generate electric power in their manned missions. Beginning in the 1960s, Gemini and Apollo missions have used this technology to generate onboard power. FCs have since replaced batteries as the main energy storage solution for NASA's manned vehicles [31].

Use of hydrogen as a propellant is not limited to space applications. Several research projects have focused on using hydrogen as a fuel to power aircraft, as an alternative to fossil fuels. Examples of this include Suntan, by the United States Air Force, in 1956; Tupolev Tu-155, made by the Soviet Union, in 1988; and CRYOPLANE, an Airbus and European Union project, started in the year 2000 [32][33]. This type of propulsion offers a cleaner burn, only emitting water, and small amounts of NO_X (much lower than during the combustion of kerosene) [34].

Currently, the vast majority of the world's supply of hydrogen is generated by extracting it from fossil fuels, such as natural gas and coal [29]. This is a well-established process, however, it comes with negative environmental impact. Production of hydrogen through these means is always responsible for emitting CO_2 and CO [35]. Despite this, there are other alternative sources, that tackle the environmental issues of hydrogen production. It can be extracted from renewable and clean sources, such as biomass, or even directly from water, in a process called electrolysis [36]. This consists in using electricity to trigger the oxidation-reduction reaction in equation 2.1:

$$H_2O + electricity \rightarrow H_2 + \frac{1}{2}O_2. \tag{2.1}$$

However, for both of these options to be truly considered sustainable there needs to be a sustainable source of biomass from which to extract hydrogen and, in the case of electrolysis, the electrical power necessary would need to be coming from renewable sources, such as solar and wind energy.

Another way to power aircraft making use of hydrogen high energy density, instead or burning it directly with oxygen, is by making use of fuel cell technology. These systems are more relevant to smaller aircraft, including UAVs.

Fuel cells are similar to traditional batteries, in the sense that they are sources of continuous electric power, generated through a chemical reaction. However, unlike a battery, fuel cells are open systems, needing a constant input of fuel and oxidizer do generate power. In batteries, the chemicals are self-contained in the battery itself, which discharges during its usage, possibly being rechargeable. This is not the case for fuel cells, which work as power sources, as long as there is fuel and oxidizer flow. They both generate direct current, but the specific energy of fuel cells is considerably larger than that

of batteries [16]. This addresses one of the main issues in battery usage in UAVs: the weight. Fuel cells can power flight for a longer time, and covering a longer distance, without the added weight to the aircraft. As of now, however, batteries remain much more attractive from an economic point of view, as they have a much lower price than FCs [37].

2.2.1 Types of Fuel Cells

There are three main types of fuel cells of interest for UAV application. These include proton exchange membrane fuel cell (PEMFC), solid oxide fuel cell (SOFC), and direct methanol fuel cell (DMFC). Each of these types are further described below, along with their main advantages and disadvantages [38].

Proton Exchange Membrane Fuel Cell

The PEMFC is essentially made up of three parts: anode, cathode, and the proton exchange membrane, or PEM, located in between the two sides. This central membrane is made of Nafion, which allows for protons (H^+) to pass from one side to the other [39]. Each electrode has a porous diffusion layer and a catalyst layer, to facilitate the chemical reactions in both the anode and cathode [40]. Equation 2.2a occurs in the anode, while the reaction in the cathode is in equation 2.2b.

$$H_2 \rightarrow 2H^+ + 2e^-, \tag{2.2a}$$

$$\frac{1}{2}O_2 + 2H^+ + 2e^- \rightarrow H_2O, \tag{2.2b}$$

with the overall reaction being simply equation 2.3:

$$\frac{1}{2}O_2 + H_2 \rightarrow H_2O. \tag{2.3}$$

The two protons created on the anode move to the cathode through the PEM, as mentioned, while the free electrons movement correspond to the electric current. A schematic representation of the PEMFC working principle is depicted in Figure 2.4a.

Currently, this type of fuel cell is the most used in UAV applications [41]. The main advantage PEMFC have over other possibilities lies with its low operating temperature, when compared to other types of FC (from 30 ℃ to 110 ℃). Besides, they are also small, and present comparatively high operating efficiency (40$\sim$60%) [41]. However, the main issue faced by this type of FC is the high cost. Both the PEM and the catalyst necessary are expensive [42]. Moreover, as it will be further discussed later, the storage of hydrogen can be a problem, given its low density, requiring large and heavy containers, if stored in gaseous form [43].

Solid Oxide Fuel Cell

The SOFC, as can be seen by its name, includes a solid oxide electrolyte. Next to this component, it has a ceramics porous cathode, and a ceramics porous anode [44]. It functions in a similar way to the PEMFC, however, instead of protons flowing from the anode to the cathode, it is negative oxygen ions (O^{2-}) that move, in the opposite direction. The reaction in the anode is in equation 2.4a, and in the

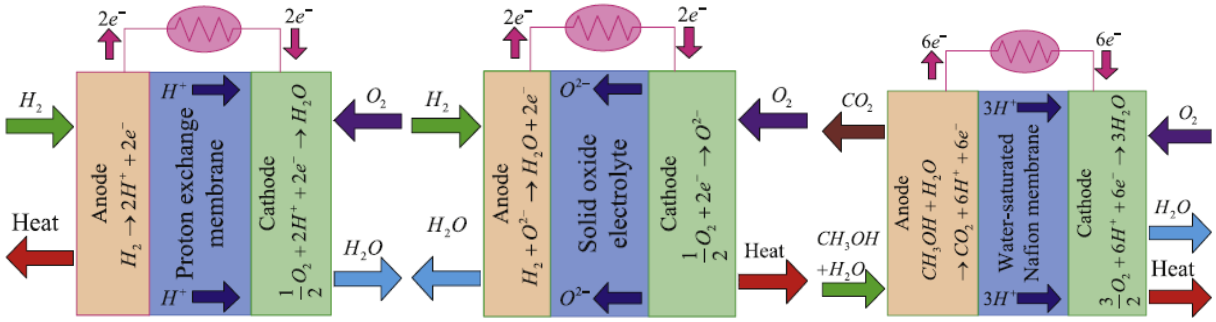

(a) PEMFC; **(b)** SOFC; **(c)** DMFC;

Figure 2.4: Fuel cell types representation (based on [38]).

cathode is equation 2.4b.

$$H_2 + O^{2-} \rightarrow H_2O + 2e^-, \tag{2.4a}$$

$$\frac{1}{2}O_2 + 2e^- \rightarrow O^{2-}, \tag{2.4b}$$

with the overall reaction being the same as in the PEMFC case, equation 2.3. In this case, the exhaust water created during the oxidation-reduction reaction is expelled from the anode side, instead of the cathode. The representation of this type of FC is in Figure 2.4b.

A SOFC operates at significantly higher temperatures than PEMFC, of up to 1000 ℃ [45]. This can bring some advantages, such as the higher efficiency without needing to use expensive catalysts, as well as making its integration with a jet engine possible [46]. SOFC can also operate using hydrocarbons, such as methane, instead of just hydrogen [47]. Using these fuels, however, will result in CO_2 emissions from the chemical reactions.

On the other hand, the high operating temperature of SOFC brings a few drawbacks as well. It requires a thermal management system capable of handling such high temperatures. Besides, this type of fuel cell can take a long time to start-up, as it warms up to its ideal temperature [48]. Another issue can arise from CO mixing with the hydrogen on the anode side, which can slow down the reactions, and produce toxic gases as byproducts [44].

Direct Methanol Fuel Cell

Unlike the previous two types, the DMFC does not use pure hydrogen as fuel, and instead resorts to methanol to function. It has a similar configuration to a PEMFC, meaning that is has a membrane permeable to proton between the anode and cathode [49]. In this case, the oxidation of methanol occurs in the anode (equation 2.5a), the protons travel through the PEM and the electrons through the electric circuit, and the reduction occurs in the cathode (equation 2.5b).

$$CH_3OH + H_2O \rightarrow CO_2 + 6H^+ + 6e^-, \tag{2.5a}$$

$$\frac{3}{2}O_2 + 6H^+ + 6e^- \rightarrow 3H_2O. \tag{2.5b}$$

In this case, the overall reactions can be written as in equation 2.6. The representation of this system is in Figure 2.4c.

$$CH_3OH + \frac{3}{2}O_2 \rightarrow CO_2 + 2H_2O. \tag{2.6}$$

As can be clearly seen from the above equations, using methanol as a fuel translates to emitting

carbon dioxide during the FC operation, negating the zero-emission benefits of pure hydrogen fuel cells. However, this fuel choice has its advantages. Given the possible storage solutions, liquid methanol has a higher energy density than compressed hydrogen, all the while being very stable under a wide range of conditions [39]. This makes it an attractive choice for long endurance applications.

However, the low efficiency of DMFCs is one of its main drawbacks. This value is lower than in other types, due to catalyst poisoning that occurs during methanol oxidation, and when part of the methanol crossing the PEM to the cathode leads to incomplete reactions [50].

2.2.2 Fuel Cell Hybrid Systems

Fuel cells, on their own, present a few limitations that hamper their usefulness as a propulsion power source. Their main issue is a relatively low specific power. This can limit the load it can power, affecting mainly the climbing rate and speed [16]. Also, the slower response time from a fuel cell system can hinder the propulsion system performance [51]. Therefore, a solution to this can be to combine two or more power sources in a hybrid system, to exploit the strengths of each source, while minimizing their drawbacks [16].

There are several different components that can be combined with a FC for a better performance. If a fully electrical configuration is desired, components such as batteries, superconductors, or solar cells can be used in the hybrid design. Alternatively, fuel cells can also be combined with a combustion engine, using configurations similar to the ones discussed in section 2.1.1.

Batteries, and in particular lithium-ion and lithium-polymer batteries, are a common source of power for UAVs. They outperform fuel cells when it comes to having a higher specific power and a faster response time. Therefore, when combined with a FC it can cover for the main limitations of fuel cells, while the whole system benefits from the higher energy density of the hydrogen. This way, the fuel cell can act as the main power source for the system, while the battery serves as a backup for peak power requirements [52]. Both components can be smaller than if they were sized for the full power demand of the mission, and the power output of the FC can be better controlled to ensure it operates in its most efficient conditions. The battery can be charged or discharged as necessary [16].

Supercapacitors, when compared with batteries, are able to output a much higher instantaneous power. This is ideal for emergency power demands. Supercapacitors can be combined in a hybrid architecture with both fuel cells and batteries, to achieve faster response time, and longer lifetimes for the different components by smoothing their power requirement [53]. However, they have the disadvantage of having low energy density and low rated voltage, needing overcharging protections [54].

Another attractive technology that can be combined with FCs is solar cells. During daylight, they provide unlimited electrical power in a renewable way, from the sun. This can significantly increase the endurance of a FC/battery-powered UAV [55]. In this situation, the solar cells, installed on the wings of the aircraft, would be the main source of power for flight, during daylight. This technology, however, has the clear issue of only being usable in good weather conditions, during a cloudless day [56]. For applications that require flight during nightime, or in regions with frequent adverse weather, solar cells are rendered useless by these external conditions. The efficiency of solar cells is also a drawback, with values around 20%, which generates as little as 200 W/m^2 [57].

Besides discussing which different power sources can be combined with FCs in a hybrid setup, it is also important to reflect on the different ways they can be connected, since there are several configurations possible. The examples given are of a fuel cell/battery hybrid system, but the same principles are applicable in the inclusion of other electrical power sources.

The simplest way to combine the different power sources is to directly connect them, in a parallel electric circuit, to the load [58]. While simple, this type of architecture does not allow for each power

source to be controlled separately from one another and, therefore, does not allow the full exploitation of each source specific strengths [59]. Particularly, the FC cannot provide effective electrical power until it reaches the same voltage as the battery pack connected to it [38].

A diagram of this direct hybrid architecture is given in Figure 2.5a. In this configuration, it is noticeable the addition of a diode to the cable connecting to the FC stack. This element is there to ensure the protection of the fuel cell, by guaranteeing there is no reverse current in the stack [38].

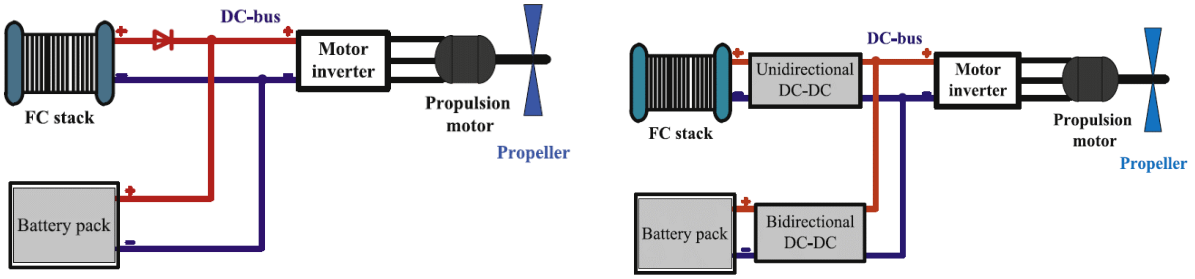

(a) Direct configuration; **(b)** Fully active configuration;

Figure 2.5: Different FC/battery hybrid configurations [38].

Figure 2.5b, on the other hand, shows the other extreme configuration, when it comes to power regulation: a fully active construction. This type of setup is indirect, meaning that the power sources and the load are not directly connected to each other, having DC/DC converters in between them. This means that all power sources have their output decoupled from each other, and each voltage can be actively regulated [60]. For the FC stack, a unidirectional DC/DC converted is used, since reverse current would damage the stack, while for the battery there is a bidirectional DC/DC converter. This allows the battery to be recharged with power from the stack if beneficial for the hybrid operation.

The fully active design described above has one major issue, however. The addition of DC/DC converters for every power source introduces a weight penalty for the propulsion system, which can decrease the overall performance of the system. It also increases the volume of the whole system [38]. Given these concerns, and intermediate semi-active configuration can be considered, such as the one on Figure 2.6.

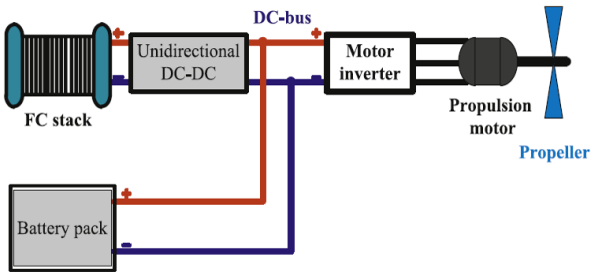

Figure 2.6: Semi-active FC/battery hybrid configuration [38].

In the construction shown, only the fuel cell stack is connected to a unidirectional DC/DC converter, while the battery is directly connected to the load. In this case, only the FC power can be actively controlled, and this element is protected by the converter. This way, there can be some control of the power output, with a smaller increase in the total weight of the system.

A design with a DC/DC converter on the battery output, instead of the FC stack, would also be called a semi-active hybrid architecture, as one power source would be actively controlled, and the other would not. Given that the FC stack is the main power source in the system, having it directly connected to the

load could reduce the energy losses from the DC/DC conversion. However, there would still be losses on the conversion on the battery side, which would also have to switch from charging and discharging modes frequently [38]. Therefore, the configuration from Figure 2.6 can be considered to be more advantageous. It has the added advantage that, because the battery is the element directly connected to the load, the output voltage of the system will be quite stable [61].

Besides the options discussed above, where all sources combined in the hybrid configuration have an electrical output, the FC power can also be combined with ICEs to form a hybrid system. In these cases, the ICE is the main source of propulsive power, which can maintain high power requirements for long endurance, but FCs are still important, particularly for the electrical requirements of aircraft [46]. One option is to integrate the FC internally, in the engine. One example of this is including a SOFC, which has a high operating temperature, in a gas turbine's bypass flow path [62]. This way, the SOFC can generate electricity for the turbine's compressor and the other needs of the aircraft, and its byproducts re-injected into the gas turbine and further burned and expelled through the nozzle. This can only be implemented in aircraft with turbine-based propulsion systems, which are larger than most typical UAVs.

More conventionally, the FC electrical power can also be integrated externally with an ICE, in the same architectures discussed in section 2.1.1 [63]. In this case, the FC stack can be powering the batteries that are, then, further connected to the EM, in either series, parallel or compound series-parallel configuration with the ICE.

For small UAVs, a series architecture, like the one exemplified in Figure 2.7, is the preferred option [38]. In this situation, both the ICE and FC stack generate electric power, to be stored in the battery. Then the battery supplies the power to EMs driving the propellers of the aircraft. In this way, both the ICE and FC can be operating in their most efficient conditions, independent of the power requirements for the thrust [63]. Naturally, depending on the application, this type of hybrid integration may not bring advantages, when compared to a fully electric alternative.

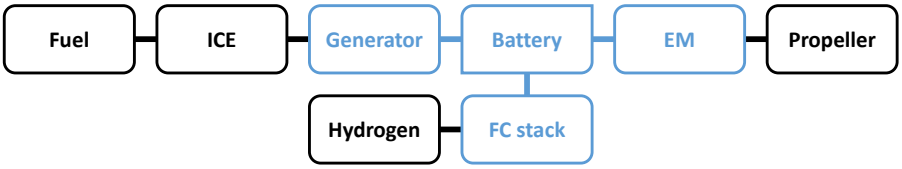

Figure 2.7: FC/ICE series hybrid configuration.

2.2.3 Applications

Given the characteristics previously described, it is only natural that fuel cell systems have been used, and continue to be studied, for aircraft application. FCs have been studied, to be the power source for aircraft in this century, but currently models including them are for smaller aircraft, with short ranges [64]. The first manned flights, using a FC as the main power source for the aircraft, were accomplished by Boeing Research & Technology Europe, in 2008. A small aircraft, with a PEMFC and batteries flew at an altitude of 1000 m. During the cruise phase, it used only the power generated by the fuel cell to fly at 100 km/h for 20 minutes [65]. Later, in 2016, DLR German Aerospace Center flew the first four-seat aircraft, powered by a FC system. With a maximum take-off weight of 1500 kg, it had a cruising speed of 145 km/h and a range of up to 1500 km [66]. Research continued to apply this technology to larger regional passenger aircraft.

Despite the previous examples, the most widespread use for fuel cell systems as power sources for aircraft propulsion lies in unmanned vehicles. As early as 2005, the American company AeroVironment successfully flew a FC-powered UAV, using liquid hydrogen as fuel. It accomplished more than one

flight, each lasting over an hour [67]. Another important step in this research effort was the aircraft developed and tested by Bradley et al. [68], at the Georgia Institute of Technology (Figure 2.8a). A PEMFC-powered aircraft was designed, with a span of 6.58 m and 16.4 kg of mass. It used compressed hydrogen gas to supply a 500 W FC. It flew under cruise conditions of 13.6 m/s, at an altitude of 10 m. Given the storage capacity, it would be able to fly 43 minutes.

There are some other examples of UAVs, using FC systems with an even smaller power output. In [69], it was shown that a PEMFC with a power as low as 100 W could power the propulsion system of a small UAV. In this aircraft, batteries were used for the take-off and climb phases, and then the fuel cell was used to power the UAV for a few minutes, in cruise conditions. In [70], a commercially available 200 W FC was used to power an UAV with 3 m wingspan. Lithium-polymer batteries were included to support current requirements of more than 6 A. It was subjected to flight tests (Figure 2.8b), lasting about half an hour.

(a) FC-powered UAV, developed by Bradle et al. [68];

(b) FC-powered UAV, developed by Dudek et al. [70];

Figure 2.8: Some FC-powered UAVs found in literature.

Another UAV, whose development is detailed in [71], shows a different hydrogen storage solution. Instead of using liquid or gaseous hydrogen, like in previous cases, it resorted to a hydride solution, using $NaBH_4$. That way, through the hydrolysis reaction depicted in equation 2.7 hydrogen was generated on board, and then used to power a 100 W PEMFC.

$$NaBH_4 + 2H_2O \rightarrow NaBO_2 + 4H_2. \tag{2.7}$$

Since hydrogen is the only gas product of the reaction, it could be separated to be used in the FC stack. The hydrogen generation system has a mass of about one third of the total FC system mass, being lighter than the stack itself. The UAV was tested by performing a continuously circular pattern, for an endurance of about 2 hours, with 360 g of $NaBH_4$ solution.

Looking into hybrid configurations, several of the constructions mentioned above have been experimented in different UAVs. In [72] a direct hybrid system is developed and extensively tested, while in [73] an active architecture is studied, as a propulsion solution for small UAV.

The integration of other components has also been successfully achieved. In [55], an UAV with a hybrid propulsion system including both a fuel cell stack and solar panels was able to fly for nearly 14 hours, cruising at 17 m/s, about twice the endurance when compared to the same configuration with only the fuel cell. In [74], the same electrical power sources - fuel cell, solar cells, and battery - were connected in a direct configuration. It showed that the UAV powered by this hybrid configuration could fly for over 22 hours. As this flight test started at night, the FC was essential to maintain power during the first hours of flight, and when weather conditions required it. During daylight, the solar cells worked as the main source of power. This combination showed how the strengths of these different sources can

be combined to better the performance of the UAV propulsion system.

Research into fuel cell applications and usage in UAV propulsion systems continues, with promising results. For example, in 2022 [75] designed and tested a power supply system for multi-rotor UAV based on a hybrid FC/battery architecture. The flight tests, performed at 200 m of altitude, showed a four fold increase in the UAV range.

Besides their recent development in UAV, there is another use for fuel cells in aviation that is worth mentioning. While not used for propulsion purposes, FCs have been studied as auxiliary power units (APUs), to provide the electrical needs of larger aircraft, specially during ground operations. Traditional APUs utilize a gas turbine to provide electrical power to the aircraft on the ground, and to start the main engines. It is generally turned off during cruise [48]. Fuel cell technology could be used to replace or complement traditional APU, in order to reduce fuel consumption and emissions. Both PEMFC and SOFC have been studied for this type of application [76]. Companies such as Airbus and Boeing have shown interest in this alternative technology to replace conventional APUs [32].

2.2.3.1 Challenges

Despite the several advantages of using FCs to power UAVs previously discussed, as well as of hydrogen-based propulsion in general, this technology obviously does come with some drawbacks. Probably the most pressing issue comes from hydrogen storage. Hydrogen, at standard temperature and pressure conditions, has a very low volumetric density of only about 0.09 kg/m^3. Combined with the tight requirements for mass and volume in aircraft, storing this fuel can be a challenge.

One option, possibly the simplest, is to store it as a gas, increasing its density by submitting it to high pressures, which can be of the order of magnitude of 10 MPa using pressure vessels made of composite materials [43]. Pressure tanks made of metal are a cheaper and more mature technology, but also come with a greater weight penalty (only about 1 wt% of hydrogen), and are limited to 50 MPa. Besides, the process of filling compressed hydrogen vessels to very high pressures is energy demanding, and comes with a rise in temperature that can become a challenge [32].

Given that, for large amounts of hydrogen storage, keeping it in the liquid state allows to reach a higher density than as a pressurized gas. However, for hydrogen to be liquefied, temperatures of -253℃ need to be reached and maintained. This process is associated with great energy losses, about 4 times greater than compressed hydrogen [43]. To properly storage hydrogen in these conditions a highly specialized cryogenic tank is needed.

The final alternative to store hydrogen is by having it chemically bound to different elements, creating hydrides. Examples of these compounds include $LiBH_4$ and $NaBH_4$, which have a theoretical hydrogen content of 18.4 wt% and 10.6 wt%, respectively [43]. The main disadvantage of this storage method lies with the need to chemically regenerate the hydrogen, before it can be used in a fuel cell system, and the need to treat the other byproducts of the chemical reaction. In the case of $NaBH_4$, this reaction has already been presented, in equation 2.7.

Besides the storage of hydrogen, the production of this product can also be considered a barrier to its widespread adoption. Hydrogen for fuel cell application requires a high level of purity. This level of purity increases the cost of production. As mentioned before, currently the most used technology for hydrogen production relies on extracting it from fossil fuels [29]. This type of production causes the emission of more carbon dioxide and, therefore, does not address the environmental issues that motivate the usage of hydrogen technology in the first place. Greener production alternatives have a higher associated cost of production, hindering their growth [32]. The production of the fuel cell themselves is also not fully sustainable, making use of heavy and rare metals, for example in the catalyst layer.

Finally, on a larger scale, to use hydrogen as a fuel for aviation, is challenging from an infrastructure

perspective. The fuel transport to airports, its storage there, and refuelling aircraft, all require different infrastructure than the ones currently used for fossil fuels [32]. If hydrogen is to become commonplace in aviation, the necessary investments in adequate infrastructure will need to be made.

Chapter 3

Experimental Setup

This chapter describes in detail the different components that make up the experimental apparatus used to perform the tests. It also includes some safety considerations that had to be taken when utilizing these systems. In particular, the use of a compressed hydrogen cylinder comes with several precautions to avoid accidents, given the flammable nature of hydrogen and high pressure of the gas inside the cylinder.

Both the fuel cell system and its integration into the hybrid test bench are described.

3.1 Fuel Cell System

The fuel cell stack is the main component to be tested, but its operation is not independent of other peripheral systems that support its operation. The PEMFC stack tested came integrated in a larger test setup, the HP 600 fuel cell system, which contained within it most necessary subsystems to run the fuel cell. Besides this main component, the system also demanded a hydrogen source to operate. As per the manufacturer's requirements, the hydrogen supply should have a purity of at least 5.0, and could come from a compressed gas tank, metal hydride storage, or an electrolyzer. A compressed gas cylinder was deemed the most convenient solution. Before entering the system, the gas pressure had to be reduced using a compatible pressure regulator. These components are described next.

3.1.1 Hydrogen Supply

Hydrogen Cylinder

The hydrogen cylinder used was a Praxair Ultra High Purity 5.0 Hydrogen Cylinder, Figure 3.1, whose specifications are in Table 3.1.

Hydrogen is classified as a hazardous material. It is an extremely flammable gas, and when mixed with atmospheric air it can self-combust at fairly low concentrations - it creates an explosive mixture if concentrations are between 4% and 76%. It is an invisible gas, with no smell, and it burns with invisible flame. Moreover, being stored in a compressed gas cylinder presents its own risks. In case the valve is broken, the cylinder can become a projectile as the gas escapes. It can displace oxygen and cause suffocation [77].

Given these potential hazards, proper storage and handling is essential to ensure the safety of the test operators, people in surrounding areas, and physical infrastructure. The cylinder should be stored and used in a well ventilated area, away from ignition sources. It should be maintained in an upright position, and firmly secured, as shown in Figure 3.1a. When not in use, the safety cap must be installed.

(a) (b)

Figure 3.1: Praxair Ultra High Purity 5.0 Hydrogen Cylinder, and respective label.

Table 3.1: Praxair Ultra High Purity 5.0 Hydrogen Cylinder specifications.

Ultra High Purity 5.0, type T	HY 5.0UH T
Hydrogen Purity	99.999%
Max. concentration of other elements	O_2 1 ppm H_2O 3 ppm THC 0.5 ppm
Dimensions	139.7 x 23.5 cm
Connection CGA/DISS	350/724
Pressure	2400 psig (165.5 bar)
Volume	7.24 m^3
Gross Weight	66 kg

The cylinder valve should not be opened without a compatible regulator connected to it, to reduce the pressure to a safe level [77][78].

The test operators had to be aware of these handling instructions. A fire extinguisher was kept nearby when the cylinder was opened, and all CfAR personnel on the building was made aware when tests were being run. The test operators used personal protective equipment: safety glasses and gloves. The cylinder was electrically grounded, and the test operators ground themselves as well, to avoid static electricity sparks. All elements were inspected for damage prior to opening the cylinder valve, and leak tests were performed to guarantee there was no hydrogen flowing to the ambient air.

Pressure Regulator

As required for the hydrogen cylinder connection, the regulator was a 350 CGA-724 DISS pressure regulator, produced by Harris, model KH1130, Figure 3.2. The regulator outlet was coupled to hydrogen-compatible tubing, with a Parker Quick connector used to link to the fuel cell system.

Figure 3.2: Harris KH1130 pressure regulator, with attached hose.

The function of the pressure regulator is to allow for the hydrogen pressure to be set at a specific value, by adjusting the central valve. It has pressure gauges indicating both the cylinder pressure and the delivery pressure. The model used was rated for a maximum inlet pressure of 3000 psi (206.8 bar), and a cylinder gauge that read values between 0 and 4000 psi (275.8 bar). On the delivery side, the pressure gauge was marked from -30 inHg (-1 bar) to 200 psi (13.8 bar). This low pressure side of the regulator had a vent valve, in case the pressure was higher than 250 psi (17.2 bar).

This pressure regulator satisfied all the needs for the experiments conducted. The maximum cylinder pressure (2400 psi) was well below the maximum value the regulator could handle, and the recom-

mended fuel cell system inlet pressure range (2 to 8 bar) was within the values it could support.

3.1.2 HP 600

The HP 600 fuel cell system is an experimental module designed for educational and research purposes, distributed by Heliocentris Energy Systems GmbH. The core component of the system is the BZ 130 fuel cell stack, produced by the German manufacturer Ulmer Brennstoffzellen-Manufaktur GmbH (UBzM). The whole system can be better understood by subdividing it in several subsystems, like shown in Figure 3.3, and Table 3.2, each of which are described below [79].

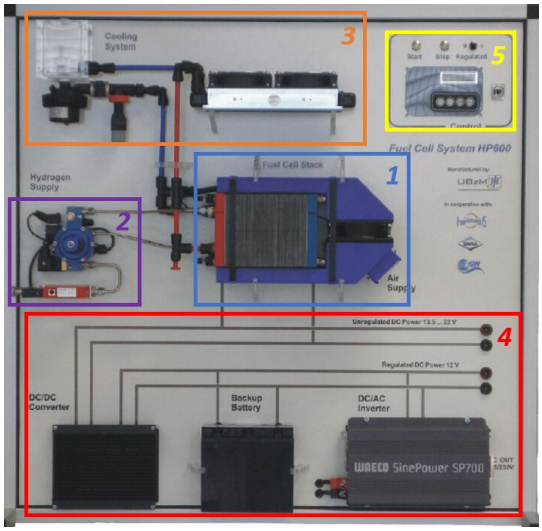

Figure 3.3: HP 600 fuel cell system.

Table 3.2: HP 600 subsystems.

#	Function
1	Fuel cell stack
2	Hydrogen supply circuit
3	Cooling system
4	Power output system
5	Control panel

Fuel Cell Stack [1]

At the centre of the HP 600 system there is the fuel cell stack (BZ 130). The stack is composed of 24 PEM fuel cells, each with 126 cm^2 of area. On the right side of the stack there is the air intake system. The cathode of the stack utilizes oxygen from atmospheric air. Prior to entering the system, the air passes through a filter, and trough a fan that adjusts the amount of air necessary. This mechanism creates a simple air recirculation channel, allowing for the system to be self-humidified by the cathode air. On the left side, at the top there is the exhaust air outlet, where the water generated in the hydrogen oxidation process can leave the system as moisture. Below it, there are the inlet and outlet for the coolant fluid, as well as the hydrogen inlet and its outlet, necessary for purging the anode.

The fuel cell stack is rated for a power of 600 W, has an open circuit voltage of 23.5 V, and a maximum current of 45 A. As previously mentioned, it requires a hydrogen purity of at least 5.0 (99.999%), and it consumes 9 L/min of hydrogen at 600 W of power. Its recommended operating temperatures are between 45 ℃ and 60 ℃. The system will show an error message if the stack temperature exceeds 65 ℃, and will automatically shutdown if it reaches 73 ℃.

Hydrogen Supply Circuit [2]

The hydrogen supply enters the system through a Parker Quick connector, at the bottom left side of this circuit. Before entering the fuel cell anode, the hydrogen passes three different components: a hydrogen flow meter, to detect and communicate how much hydrogen is entering the system; a pressure regulator, to reduce the hydrogen pressure to the correct value for the fuel cell operation; and a

solenoid valve, to open or close the hydrogen supply to the system according to the state of all necessary parameters. The system can receive hydrogen with a pressure between 2 and 17 bar (2 to 8 bar recommended), and the pressure regulator will reduce it down to 300 mbar. There are over-pressure blow-off-valves, in case the inlet pressure exceeds 30 bar, or the integrated regulator outlet exceeds 500 mbar.

On the fuel cell anode outlet, there is a purge outlet, which can blow out small amounts of hydrogen and water, in case there are too many impurities in the anode. This occurs occasionally during the fuel cell operation, and more frequently during the startup and shutdown procedures. As small amounts of hydrogen are released to the ambient air, it is important to guarantee enough ventilation of the test location.

Cooling System [3]

As the chemical reactions that occur in the FC stack produce heat, there is a water-based cooling circuit to dissipate the heat and control the temperature of the stack. The system requires a non-conductive coolant (with a conductivity of less than 1 µS/cm), which is stored in the reservoir in the top left side of the system. In the experiments performed, deionized water was used, which typically has a conductivity of 0.05 µS/cm.

Below the reservoir, a water pump draws cooling water into the stack (passing through a flow meter), which heats up and then passes the aluminum water/air heat exchanger. There, the heat can be dissipated directly into the ambient air. If the cooling water temperature is high enough, the electric fans above the heat exchanger start spinning to help remove the heat from the system.

To guarantee this system works as intended, the liquid level must be maintained at least above the sensor height in the reservoir, and the water should be replaced every six months, or 50 hours of operation, to prevent its conductivity from increasing beyond acceptable levels.

Power Output System [4]

The electrical power generated by the fuel cell stack can be connected to a load by three different means: unregulated direct current (DC) power, regulated DC power, or alternating current (AC) power. Their output capabilities are specified in Table3.3.

Table 3.3: HP 600 power output options.

	Unregulated DC	**Regulated DC**	**AC (50 Hz)**
Voltage [V]	13.5 to 22	12	230
Maximum Current [A]	45	42	2.5

The unregulated power output corresponds to the electrical power generated directly by the FC stack, depending on operating conditions and load. It can be used connecting directly into the sockets above. The connection below provides the regulated DC power, which can deliver a constant voltage of 12 V regardless of the voltage of the stack. It is achieved by the 700 W DC/DC converter on the left, which also ensures the backup battery in the centre (connected in parallel to the regulated DC output) is charged. This type of power output corresponds to a semi-active FC/battery hybrid configuration, as previously explained in Section 2.2.2, and represented in Figure 2.6.

For applications requiring AC power, the DC/AC inverter on the bottom right, which is also connected in parallel to the regulated DC power, is able to supply 230 V of AC power by connecting the load directly to the sockets on the right side of the inverter.

Control Panel [5]

The FC system has an internal microprocessor control unit that manages startup and shutdown procedures, and constantly monitors system variables such as temperature, voltage, and current, to take action if necessary. The control panel on the top right corner of the system allows for the user to interact with this unit. The first two buttons at the top read *Start* and *Stop* and, naturally, are used to turn on the FC system and to shut it down, respectively. The switch to their right allows to select the desired power output type: *R* for regulated DC power, and *U* for unregulated.

Below the buttons, there is a small LCD screen where the system variables can be displayed, as well as possible error messages. To its right, the USB port facilitates the connection to a computer, where the data could be visualized in a graphical interface, with the help of the *HP 600 Software*, which was not available at the time of testing. This software would also simplifies data recording and, additionally, would allow the test operator to choose a setpoint value for the stack temperature and humidity level. This could not be done directly on the FC system, as its screen has only visualizing capabilities.

3.2 Electric Load

In order to test the fuel cell, some type of electric load had to be connected to the output of the system. In the first phase of testing, described in Chapter 4, a programmable load was used. Later, the system was connected to different electric motors and propellers, to simulate a real propulsion application. These loads are described below.

Programmable Load: To characterize the fuel cell stack performance, it was necessary to test its behaviour over a large range of current and voltage. For such, a programmable electronic load (KIKUSUI PLZ1004WH) was used, in the continuous current mode. This means that a current value was selected on the load, and the DC voltage would adjust to make sure the correct current was delivered to the load. The load would display the values of current, voltage, and power it was consuming from the electric circuit.

Electric Motor: To better simulate real UAV applications, it was necessary to perform tests using electric motors, attached to propellers. Throughout the experimental campaign, the following EMs were used: XING2 1404 Toothpick Ultralight Build (Figure 3.4a); E-flite Power 46 BL (Figure 3.4b); AXI 2826/10 Gold Line V2 Long (Figure 3.4c). All of them are outrunner brushless direct current (BLDC) motors, and their specifications are compiled in Table 3.4. These motors were chosen to operate roughly in the same range of voltage and current as the fuel cell could provide.

Table 3.4: Electric motors specifications.

Parameter	XING2 1404	E-flite 46	AXI 2826
Number of LiPo cells	3-4S	4-5S	3-5S
Number of poles	12	14	14
Weight [g]	9.1	290	187
$\mathrm{K_v}$ **[RPM/V]**	3000	670	920
Max. Power [W]	220.8	800	740
Max. Current [A]	13.8	40	43
No Load Current [A]	$<$0.36	3.88	1.7
Internal Resistance [mΩ]	309	40	20

Electric motors have the purpose of converting electrical power to mechanical power. As the name

(a) XING2 1404 Toothpick Ultralight Build; **(b)** E-flite Power 46 BL; **(c)** AXI 2826/10 Gold Line V2 Long;

Figure 3.4: Electric motors used.

indicates, and contrary to brushed DC motors, brushless motors do not make use of brushes to conduct current and help generate the rotational movement. This means they have a higher durability, as bushes wear relatively quickly from the continuous contact, and require frequent maintenance. Therefore, even if they are typically more expensive and complicated to build, BLDC motors offer a more reliable and efficient alternative to brushed DC motors [18].

In this type of motor, the current only moves through the stator, while the rotor is made up of permanent magnets. The rotor moves due to the changing direction of the magnetic fields created by the fixed coils in the stator. This is achieved by constantly changing which coils are conducting current. This recreates an approximated sinusoidal three-phase current, by replicating a pattern like the one shown in Figure 3.5a. This action is performed by an electronic speed controller (ESC). This device uses metal–oxide–semiconductor field-effect transistors (MOSFETs) to let current through only the appropriate phases, by switching which transistors are active and which ones are not. It detects the position in which the EM rotor is on and selects the correct state, with the help of a microcontroller, like shown in the diagram of Figure 3.5b.

In the testing campaign, different ESCs were used, for the different motors. In particular, a Castle Phoenix Edge HV 120 and a T-Motor Flame 70A LV were used. They covered the necessary range of voltage and current for the motors tested.

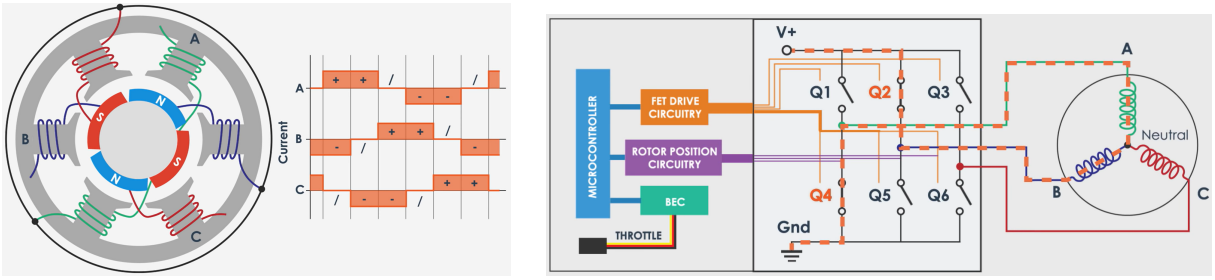

(a) **(b)**

Figure 3.5: BLDC and ESC working principle (from [80]).

Like mentioned before, all motors used were outrunner as well. BLDC motors are classified based on the location of their rotor. In the outrunner configuration the rotor is located around the stator, while inrunner motor have the rotor inside, with the stator surrounding it. Given that the rotating part of the EM is further away from its axis in an outrunner arrangement, this type of BLDC motor gives higher torque,

but at a lower rotational speed, given the added inertia.

Regardless of these differences, the operation mode of different types of DC motors is essentially the same, and can be better understand with the help of the diagram in Figure 3.6. It represents the equivalent circuit of a DC electric motor, where V is the supplied voltage; I is the applied current; R_m is the internal resistance of the motor; I_0 is the no load current; V_m is the motor's internal back electromotive force (EMF) voltage; and ω_m and Q_m are the output rotational speed and torque, respectively. From a direct visualization of the circuit, the back EMF can be calculated, using equation 3.1,

$$V_m = V - IR_m. \tag{3.1}$$

The motor speed constant, K_v, is calculated making use of this previous value, following the relation in equation 3.2,

$$\omega_m = V_m K_v, \tag{3.2}$$

where K_v can be given in rad/sV or, more usually, in revolutions per minute (RPM)/V.

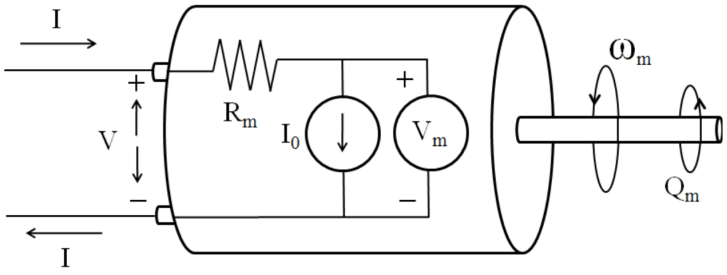

Figure 3.6: DC motor equivalent circuit (from [18]).

The torque output of the EM can be calculated using equation 3.3,

$$Q_m = \frac{I - I_0}{K_v}, \tag{3.3}$$

where K_v must be in SI units (rad/sV).

Finally, it is relevant to remember that the electrical power supplied to the EM is given by the product of the current by the voltage supplied, while the mechanical power it is producing is simply the product of ω_m by Q_m. The efficiency of the motor is naturally given by the ratio between these two quantities.

Propeller: The propeller is the component that, by being turned by a rotating shaft, generates a force, which can be used as the necessary thrust force in an aircraft. It functions basically as a rotating wing: the lift force creates by the blade contributes to the thrust, while the drag on each blade contributes to the overall torque necessary to rotate the propeller [24].

Different propellers were used for the different electric motors, given their different speed and torque outputs. For the smaller XING motor, a Nazgul T4030 propeller was used. It has two polycarbonate blades, measuring a total of 10 cm. As for the E-flite and AXI motors, the propeller used was a 12"×6 propeller.

As the propellers would be rotating at high speeds, it was important to ensure they were balanced. This helps to prevent unwanted vibrations during the rotation, due to asymmetries in the weight distribution of the propeller, protecting the system from potential failure. Therefore, this component was placed in a propeller balance, which uses magnets to allow for frictionless rotation, to check if the propeller was unbalanced. In case it was not, sandpaper was used to remove small amounts of material from the tip of

the heaviest side, maintaining the aerodynamic shape of the airfoil, until the component was balanced. The results from this process can be seen in Figure 3.7.

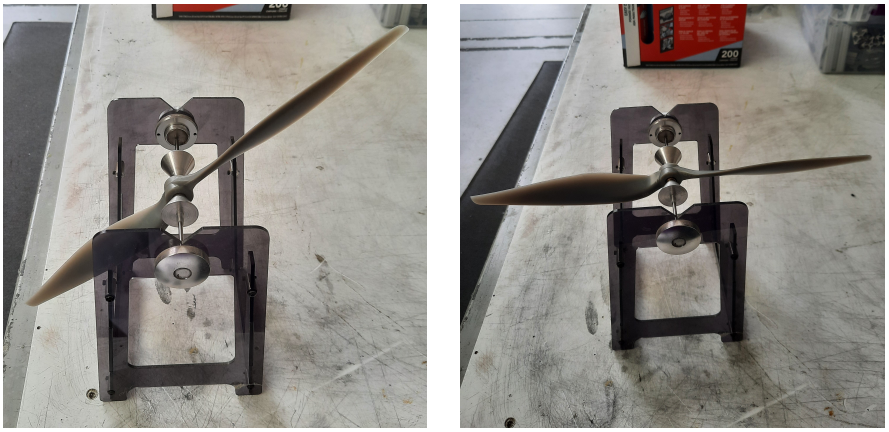

(a) Before balancing; **(b)** After balancing;

Figure 3.7: Propeller balance.

3.3 Hybrid Test Bench

To test the fuel cell stack as the power source for a hybrid propulsion system, the hybrid test bench available at CfAR was used. It had been previously developed by different student groups in phases, as part of the continued efforts to study hybrid electric propulsion [81][82][83]. This test rig is picture in Figure 3.8. It is a parallel hybrid configuration, which had two different EMs to produce the mechanical power that could be combined.

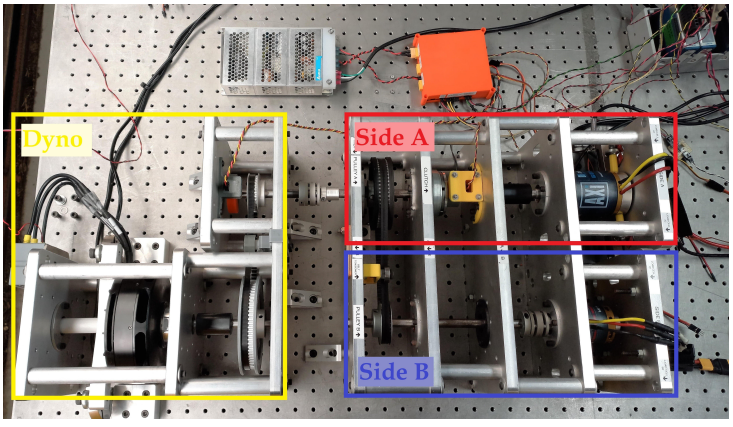

Figure 3.8: Hybrid test bench.

This setup was custom made for CfAR, to allow for hybrid propulsion tests to be performed, and this configuration was designed to house two AXI electric motors of different sizes: 5345/16 HD 3D Extreme V2, and 4130/20 Gold Line V2. As marked in the picture, each side of the parallel system is labelled with a different letter, with side A having the larger of the two motors. The two sides are coupled with a rubber band, which is connected to two gears of the same size on each side, meaning an unitary gear ratio. Side A of the test bench also included an electromagnetic clutch, allowing the test operator to connect or disconnect this side at will. This power-generating module was connected to the dynamometer (dyno) side of the test bench, whose central piece is the T-Motor U15II KV100, working

as a generator, whose power output was converted by a rectifier into a DC signal. This gave an extra degree of flexibility to the system: instead of having its load tied to the geometry of a single propeller or set of propellers, the load was instead the power output of the dyno, determined by the electrical load demanded by a programmable load. The dynamometer axis was linked to the side A axis by a gear ratio of 2.25, meaning it was rotating 2.25 times slower than the rest of the system.

The hybrid test bench included a series of sensors to measure relevant data to characterize its operation. All three motors were equipped with a pair of load cells, which allowed for the torque to be measured. Two hall effect sensors gave RPM measurements. Since they were both installed on the axis connected to side A, they offered a way to double-check their readings were correct, while the dyno RPM could be easily calculated based on the known gear ratios. Besides, being on opposite sides of the electromagnetic clutch, if consistently different measurements were noticed, it could indicate the clutch as slipping.

The hybrid test bench setup allows for four basic operating modes: side A only, side B only, hybrid, and regeneration mode. The electromagnetic clutch allows the side B only mode to operate truly independent from the side A, while in side A only operation the clutch has to be engaged and, therefore, the motor on the side A has to spin the (unplugged) side B motor. Both other operating modes use the two motors and thus can only work while the clutch is engaged.

All the variables related to the test bench were programmed in a LabVIEW VI (Figure 3.9) that had to be developed as part of this experimental work, but will only be briefly described. The VI includes control functions, to set the pulse width modulation (PWM) signal to be sent to each of the motors, as well as a button to engage or disengage the electromagnetic clutch. It has plots that show, in real time, the different parameters being measured and calculated, such as RPM and torque. When each test is complete, the program saves the data logs from all these variable, to later be analyzed. Further information oh this VI can be found in [84].

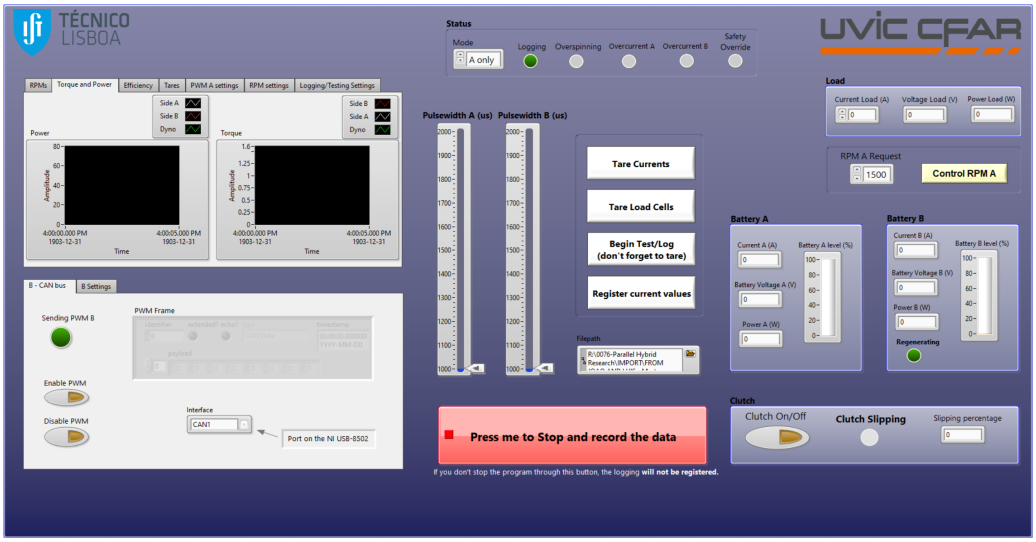

Figure 3.9: LabVIEW VI graphical user interface developed for hybrid testing.

Chapter 4

Experimental Tests

In this chapter, the experimental tests performed and the data collected are presented. It begins by describing the initial phase of testing conducted on the fuel cell system, to characterize its performance. First, the checking of the entire hydrogen inlet circuit for leaks is discussed, and the standard cycle performed to obtain a baseline current-voltage polarization curve is explained. Finally, the determination of important characteristic parameters of the stack such as rated power and efficiency are presented.

For the experimental setup described in Chapter 3, it is important to first test the FC stack to confirm its performance, and to gather the necessary data for later usage in different operating conditions, as well as under its two operating modes, before moving on to implement a hybrid propulsion configuration. These tests were conducted in accordance with the manufacturer's specifications, and following test procedure recommendations found on the European Union's FUERO Project report, which seeks to establish a standard methodology for testing PEMFC stacks [85].

Then, simple propulsion tests were conducted, to verify the system's performance when powering electric motors, typically used in the propulsion systems of small UAVs. These tests aimed to confirm the stack's response when being used in real applications, rather than just arbitrarily setting the desired output current. Then, the FC was included as one of the energy sources in the hybrid system. The tests performed are briefly described, while the results are later presented in Chapter 5.

4.1 Fuel Cell Characterization Tests

4.1.1 Leak Tests

The first step to begin characterizing the FC system was checking the condition of each component. In practice, this meant verifying that the different parts of the hydrogen supply circuit were not leaking, for both safety and efficiency reasons, and that the HP 600 fuel cell system was functioning. With this in mind, it was essential to first review applicable safety measures, and develop adequate test procedures, according to operating guidelines.

The test procedure essentially consisted in tightly connecting all necessary parts, and then gradually opening the relevant valves for each segment of the hydrogen circuit. In the regulator a pressure test was first performed. This was done by opening the hydrogen cylinder valve and adjusting the pressure in the regulator, with its output valve closed. Then, the hydrogen supply was closed, and over a few minutes the pressure gauges were checked to verify if the pressure was stable (if there was a leak, the pressure inside the regulator would decrease). In all connections in the hydrogen circuit a bubble test was conducted as well. This test was accomplished by applying a soap-water solution at points of interest, and checking for bubble formation. If any bubbles started appearing, it would mean there was a

leak in that location. In the entire hydrogen circuit, twenty-two test locations were identified, as illustrated in Figure 4.1.

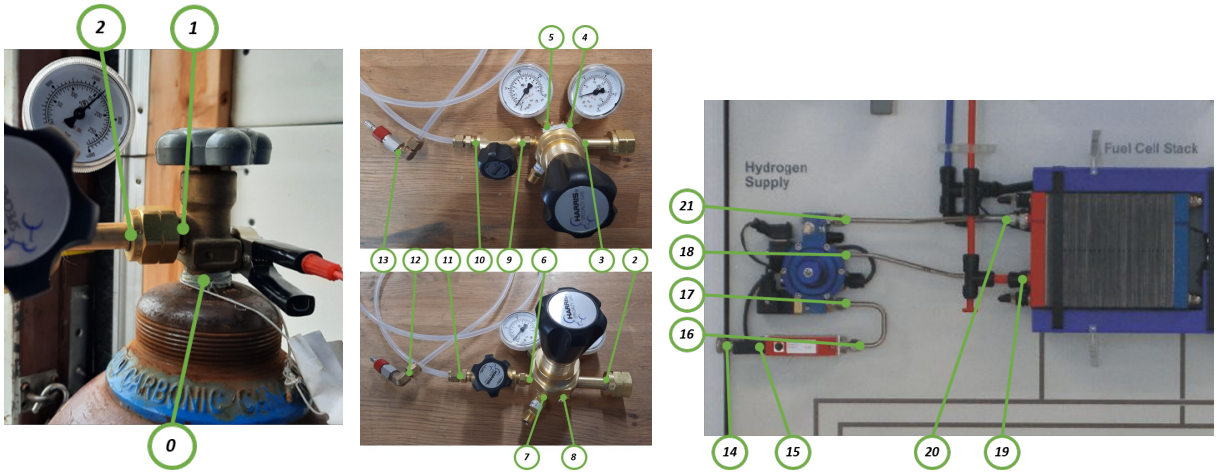

(a) Test points in the hydrogen cylinder.

(b) Test points in the pressure regulator and hose.

(c) Test points in the HP 600 hydrogen supply system.

Figure 4.1: Test points in the hydrogen circuit.

The leak tests were performed in two separate phases: first, only the hydrogen cylinder, regulator, and hose connections were tested, to ensure there were no leak points upstream of the FC system hydrogen inlet, and only after the hydrogen circuit in the fuel cell system itself was tested, which had to be done with the system already turned on.

Cylinder and Regulator: As both the hydrogen cylinder and the pressure regulator had not been used previously, it was important to inspect these components, to guarantee that neither of them were faulty. Since this also represented the first experiment conducted at CfAR with the compressed hydrogen cylinder, there was an extensive review of safety protocols.

The test, as described above, began with a simple pressure test on the regulator. As the hydrogen cylinder had not been used before, the cylinder pressure gauge read 2400 psi, as expected. The regulator valve was adjusted to provide a delivery pressure of 8 bar, since that was the highest value predicted to be used, as recommended by the FC system manufacturer for the hydrogen supply. When the cylinder valve was closed, the regulator maintained these pressure values, indicating the absence of leaks.

A bubble test was then conducted, first encompassing only test points 0 to 9, and then for test points 10 to 15, after opening the regulator output valve. No bubble formation was observed, so the test were considered successful, and there was no leaks in the components analyzed.

Fuel Cell System: For the test of the hydrogen circuit on the FC system, the whole system had to be turned on to provide hydrogen circulation to the fuel cell. To be able to start the system, some general maintenance activities had to be completed, namely refilling the cooling fluid circuit with deionized water, and recharging and reinstalling the backup battery. Then the system was restarted and points 14 to 21 were tested for leaks. Again, as no bubble formation was observed, the tests were considered successful, and no leaks were identified.

This testing phase also allowed to confirm that the different components of the fuel cell system were working properly, allowing the production of electric power from the PEMFC. Both regulated and unregulated power outputs were connected to a programmable load, and the power generation was

verified. All sensor readings were checked in the system's LCD screen, as well as the cooling circuit function and the charging of the battery were confirmed.

4.1.2 Standard Cycle - Polarization Curve

To properly characterize the performance of the FC stack, the first test to be performed was a standard polarization curve. This allowed for the development of a benchmark current-voltage curve, which reflects the way in which the fuel cell behaves in reality. This also permitted a comparison between the experimental values obtained, and the data provided by the manufacturer, as well as with the MATLAB model for the same fuel cell, developed at CfAR by Philipp Sharikov [86].

The test consisted in setting the current of the stack, with the help of the programmable load connected to the system's unregulated power output, and measuring the corresponding stack voltage. With this data, the current-voltage curve can be drawn, and the power can be calculated for each point to complete a current-power curve. These are the two performance curves for which there was manufacturer's data to compare to. Prior to any data measurement, the fuel cell system had to be run for about an hour, to have enough time to warm up to its reference operating temperature, of 55 ºC, and to guarantee it was in stationary conditions before each test. This procedure aims to make sure each time measurements were taken, the stack was in similar conditions.

To obtain the benchmark current-voltage curve the standard cycle was performed three times, to confirm the reproducibility of the results. The data collected directly from the FC system sensors during the three test runs, and the power calculated by $P_{stack} = U_{stack} \times I_{stack}$, is presented in Figure 4.2, along with the average value for all the tests. In Figure 4.3, the same average values are presented alongside the current-voltage and current-power curves given by the manufacturer, where both power and potential are adjusted per cell, and the current is given in the form of current density.

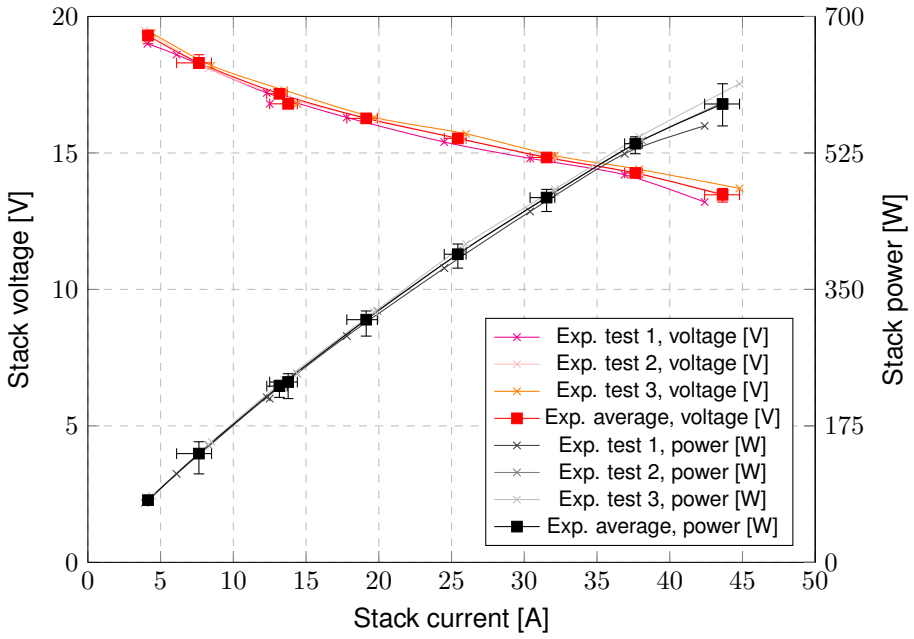

Figure 4.2: Experimental data polarization curve, with average.

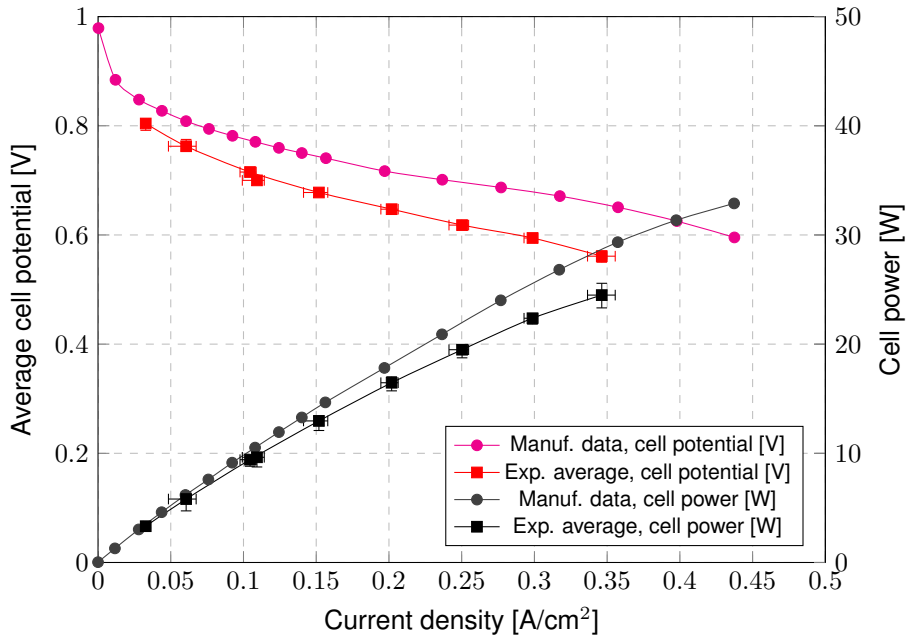

Figure 4.3: Polarization curve, with experimental average and manufacturer's data.

As can be clearly seen, the results for each of the experiments were very similar with one another, confirming that the fuel cell stack has a predictably behaviour, given the same operating conditions. The area of the plot where the voltage curves move further away from the average values are at the highest current end. In particular, on the first polarization curve performed, it was not possible to reach the highest values of current the FC stack can produce, and the voltage values were below expected. During this test, as the load was progressively increased, the FC system started displaying a *single-cell error*, and began disconnecting the load automatically. This error indicates that one cell group (each composed of 3 cells) is performing 25% below average, and it can occur for a few different reasons. The first explanation could be stack being at a too low temperature, which was discarded immediately, as the

temperature was well above the minimum recommended. The second reason could be due to defect or degradation of a single cell. This seemed unlikely, as the FC system did not have too many hours of lifetime operation previous to the testing at CfAR, which would not justify such degradation. This was confirmed in the following two tests, as the stack was able to deliver its maximum current of 45 A without encountering the same error. Finally, the problem could be caused by an excess of water blocking single cells, due to too high humidity in the air supply. This was the most plausible explanation to the behaviour encountered during the test. As it was the first extensive run of the fuel cell in several months, the behaviour during this experiment was not as consistent as in future tests, particular when it came to maintaining temperature and humidity levels. During the warm up phase, the cathode air measured humidity levels of up to 100%, maintaining high values for the first few test points, with high loads. After operating at lower loads, the humidity decreased, and in the following tests the FC did not report this issue again, giving confidence in it stemming from the long time without operation. This clearly showed that, just like the manufacturer had warned, previous operating conditions, and the membrane humidity in particular, can have an important impact on the fuel cells' performance.

Despite this difference between the tests, the results are still very close between experiments, justifying using the average of these three runs as a benchmark for the FC stack performance. When comparing this average curve with the data made available by the manufacturer, it can be seen that in reality the average cell potential (and, therefore, its power) is consistently smaller than indicated. This difference is more pronounced at higher currents, being close to 14%, while for the smaller current values this voltage drop is only about 4%. True OCV conditions (0 A current) could not be analyzed, as even with no load connected, the FC stack is still powering the electronic systems in the HP 600 (sensors, coolant pump and fans, control unit, etc.) and sustaining the battery charge, justifying not reaching current values below a minimum of about 4 A.

For a better visualization of potential and power separately, Figure 4.4 is present, where the results taken from the computational MATLAB model are also included for comparison.

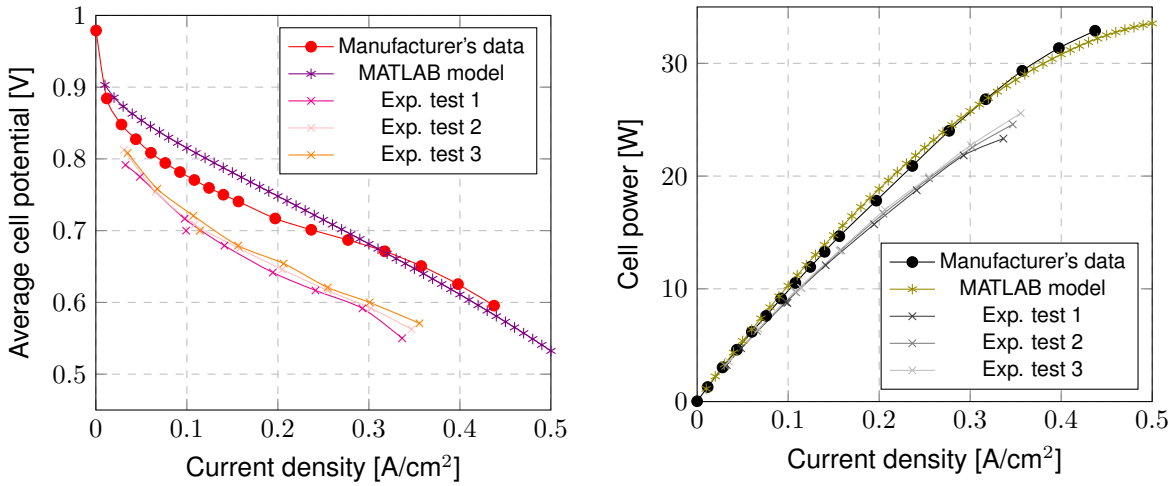

(a) Voltage polarization curve.

(b) Power polarization curve.

Figure 4.4: Experimental polarization curves.

Despite the difference in values already described above, the experimental results were in line with the rated power of the fuel cell system as a whole. When the fuel cell was operating at its rated current of 45 A, it was indeed producing 600 W. However, not all that power could be delivered to the external load. Not only were there the voltage losses due to resistance in the connections, but also part of the current was being used internally to power the system. Therefore, the maximum power reached by the

FC stack is not the same as the maximum usable power for an external load. A further discussion of the power reaching the load is presented in the following section.

4.1.2.1 Load Power

In this first round of testing, it was noticeable that the values of current requested by the programmable load did not match with those that were being read by the system in the FC stack. The current in the stack was significantly higher than the one measure by the load, whose values are plotted in Figure 4.5a. The current drop seemed to have an unpredictable behaviour, with no clear trend over the three tests performed. While with no load the system showed a stack current of about 4 A, the current difference was higher than that for higher loads, reaching values as high as 6.5 A. However, given the relation between the load current requested, and the actual stack current, in Figure 4.5b (in this case for the third experiment), it seemed that this current drop was not affecting the linear relationship between these two variables. In this plot, the fitted line showed a value for R^2 of 0.9997, with a slope of nearly 1 as well (0.97).

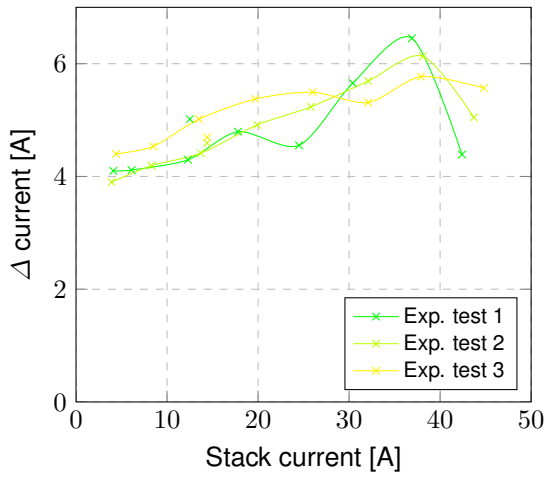

(a) Current difference between FC stack and programmable load.

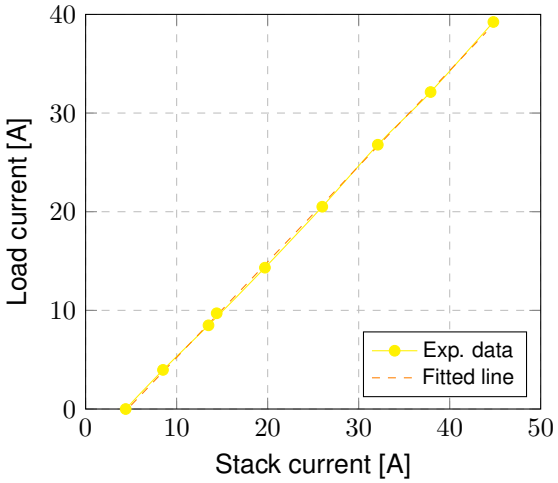

(b) Programmable load current trend.

Figure 4.5: Programmable load current behaviour.

Just like the current, the voltage also presented a significant difference between what was measure by the FC system at the stack and what the programmable load was receiving, which at is highest was nearly 40% of the total stack potential. As visible in Figure 4.6 (also from the third experiment), the relation between the voltage drop observed and the current showed a linear behaviour ($R^2 = 0.9924$), which would be consistent with Ohm's law, $U = R \times I$. With the trendline slope, a resistance of 0.148 Ω was estimated. Similar behaviour was observed in the first two experiments. This value was too small to be confirmed experimentally with the available ohmmeters.

Despite being a fairly small resistance value, given the high currents being reached (above 40 A), nearly 300 W was being dissipated in the connections, and the wiring was getting extremely hot. The value of resistance found is considerably higher than what would be expected for the wires being used (14 AWG), which can be theoretically estimated as 0.058 Ω for two 3.5 m cables [87]. However, this estimate is for wires at 20℃, while the cables were well above that. It was recognized that these wires were not rated to carry such high values of current for sustained periods of time, which could explain the bad performance encountered. Given that, the wiring was replaced with much thicker wires (4 AWG) to prevent potential further issues. With these new cables, it was confirmed that there no longer was

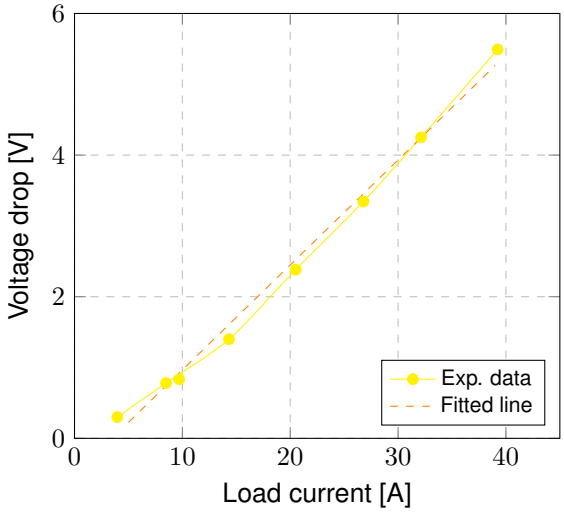

Figure 4.6: Voltage drop between FC stack and programmable load.

a significant voltage difference between the value measured by the system in the stack, and the one received by the electric load. These difference measured around 0.1 V, which is negligible given the uncertainty associated with the measurements made.

The difference in the power transmitted from the stack to the electric load is depicted in Figure 4.7a, where it can be clearly seen the difference the thicker wires made. In this last test, the lost power corresponds only to the power associated with the difference in current measured. This power is internally used by the FC system. The ratio between the produced power and the one that reached the load is represented in Figure 4.7b. After the voltage drop was corrected, it was possible to reach an efficiency of more than 80%, for the higher power conditions, with 500 W reaching the programmable load.

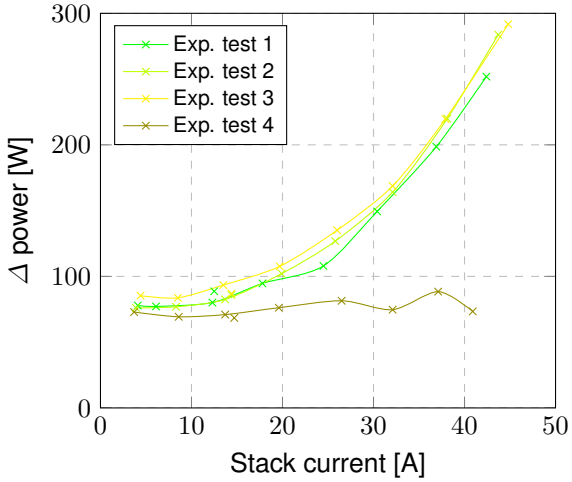

(a) Power difference between FC stack and programmable load.

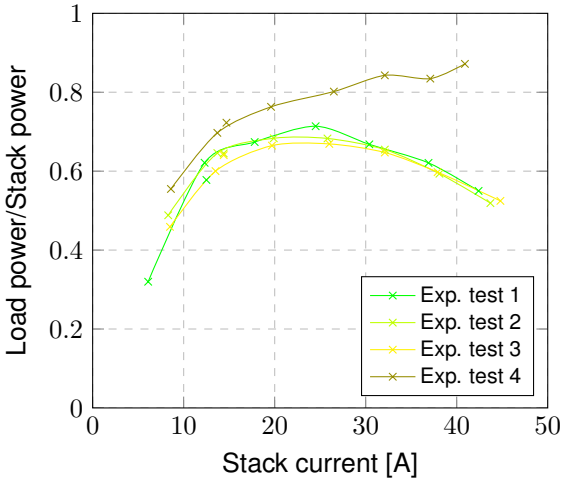

(b) Transmission efficiency between FC stack and programmable load.

Figure 4.7: Power losses to the electric load, and efficiency.

Despite these significant gains in terms of available power to the load, the stack behaviour along the polarization curve developed remained the same, as its performance was not affected by these external elements. This confirmed the validity of the previous results, as well as the values calculated further down this section, which were based on data taken from the same experimental tests.

4.1.3 Characteristic Parameters

The following tests allowed for a better characterization of the stack performance. The basis of each test was performing a polarization curve, like in the previous section, to obtain the FC performance. Given the educational nature of the HP 600 fuel cell system, not all parameters that affect a FC performance could be tested, as they were not adjustable. Namely, pressure and stoichiometry could not be performed, while temperature and humidity would be the only variables whose reference value could be controlled by the test operator, if the FC system software had been available. The tests focused on the power and efficiency of the stack, as well as the system's regulated operating mode.

4.1.3.1 Power Density Test

The first test, to determine the rated power of the fuel cell stack, was performed directly after each of the previous polarization curves were completed. It consisted in adjusting the load in such a way that the stack was at its nominal voltage, which corresponds to an average cell potential of 0.7 V, or 16.8 V for the 24-cell stack. With the experimental data gathered, the rated stack power was calculated, given that $P_{rated} = U_{nom} \times I(U_{nom})$. The values obtained are in Table 4.1.

Table 4.1: Experimental values for the stack's rated power.

Test run	Power [W]
1	210.00
2	241.92
3	241.92

As can be seen, the value in the first test run, despite being in a similar order of magnitude, is quite different from the other two. As the voltage was adjusted to be 16.8 V, this variation comes solely from a different value of current measured. Given the more erratic behaviour already mentioned when it came to the first test, it is fair to think that this value is not as reliable as the others. In the first test run, by the time this value for the nominal voltage was measured, the temperature and humidity had already dropped quite significantly, so the conditions in which they were taken are not truly the same as in later experiments. When compared to the manufacturer's data, the calculated value is essentially half of the expected one. This happens because, given the lower voltage shown by the stack, the current for which the stack is at 16.8 V is half of the one in the manufacturer's datasheet. Looking at the difference in power for the current density actually measured, the value is only about 9%, consequence of the voltage difference mentioned in Section 4.1.2.

4.1.3.2 Electrical Efficiency Test

Another test that could be completed simultaneously with the polarization curves is the electrical efficiency test. This test is based on equation 4.1 [85].

$$\eta_{el} = \frac{U_{stack} \times I_{stack}}{\dot{n}_{hydrogen,supplied} \times \Delta H_f^0 \left(H_2O(g)\right)} = \frac{U_{stack} \times I_{stack}}{\frac{\dot{V}_{hydrogen}}{1000 \times 60} \times \frac{p}{\overline{R} \times T_{273}} \times \Delta H_f^0 \left(H_2O(g)\right)}, \tag{4.1}$$

where η_{el} it the electrical efficiency of the stack, U_{stack} and I_{stack} are the stack voltage [V] and current [A], respectively, $\dot{n}_{hydrogen,supplied}$ is the hydrogen supplied to the stack [mol/s], and $\Delta H_f^0 \left(H_2O(g)\right)$ it the enthalpy of formation of steam, 241.82×10^3 J/mol. The values of p, $\overline{R}$, and T_{273} are constants as well, equal to 101325 Pa, 8.3145 J/(mol K), and 273 K, respectively. Finally, $\dot{V}_{hydrogen}$ is the hydrogen flow,

in l/min, whose value is measured directly by the flow meter in the FC system. Given these values, the expression can be further simplified to equation 4.2.

$$\eta_{el} = \frac{U_{stack} \times I_{stack}}{\dot{V}_{hydrogen} \times 179.911446}, \tag{4.2}$$

where all variables can be measured directly.

Therefore, when the polarization curves were performed, the hydrogen flows were measured as well, and the electrical efficiency of the FC stack was estimated. These calculations are reflected in Figures 4.8a and 4.8b, which also include the results taken from the MATLAB model for comparison.

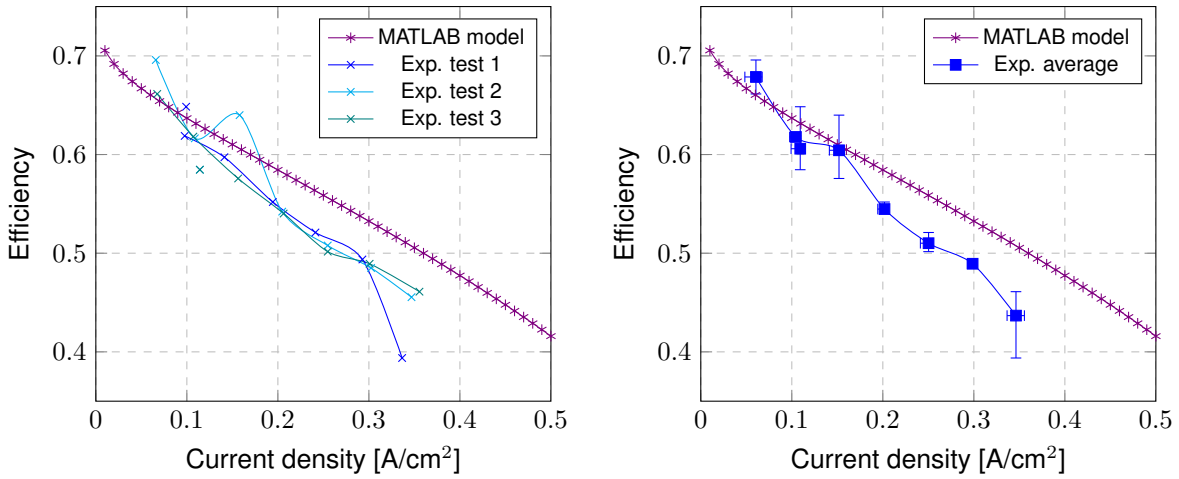

(a) Experimental values for electrical efficiency.

(b) Experimental average for electrical efficiency.

Figure 4.8: Experimental efficiency curves.

One clear aspect of the plots that should be noted is that the measurements were not as close to each other for efficiency as they were previously for voltage and power. This stems, in part, from the more significant oscillations in the value read by the flow meter sensor, when compared to voltage and current readings. The internal controller of the fuel cell system also seemed to affect the results in certain cases. In particular, for the lowest current experimental point in the polarization curve the hydrogen flow that was read was only 0.12 or 0.13 l/min, which corresponded to a calculated efficiency of 360%. Given this unreasonable result, in the last test this point was observed with special attention, and an unsteady behaviour was identified. It was observed that the hydrogen intake would briefly take in a much higher flow of gas (above 2 l/min), and then quickly go back to consuming only about 0.12 l/min for a long period. Given that most of the time (when the purge valve is closed) the system does not lose hydrogen, working as a dead-end stack, it seems that for very small loads the system's controller occasionally lets in a larger-than-necessary amount of hydrogen and then operates with an intake flow much lower than what would be necessary if there was no excess hydrogen already inside the stack system. For this reason, the efficiency values obtained using these very low hydrogen flow rates were disregarded as not valid, and are not represented in the previous plots.

It is also relevant to take note of the general trend the experimental data shows. As predicted by the computational model, the fuel cell stack shows higher efficiency for smaller load, where it reaches values greater than 60%, and reducing as the current increases, getting close to 40% for the maximum current of the system. This happens because, as the current drawn increases, the different types of voltage losses become more significant, meaning the fuel cell is not able to provide the entire energy potential provided by the hydrogen. These losses come from the the activation energy barrier that has to be reached; the ohmic losses from the internal resistance of the stack; and the concentration losses

due to slow mass diffusion process, all of which are greater for higher currents [88]. Nevertheless, the range of efficiency found is in line what is expected from a PEMFC such as this one [41], and much higher than the efficiency of combustion engines.

4.1.4 Regulated Operating Mode Test

Besides the previous tests, that aimed at confirming the performance of the fuel cell stack, on its own, the behaviour of the system as a whole was also tested, by making use of the regulated power output of the FC system. This test was performed in a similar way to the previous ones, making use of a programmable electric load, to be able to test operating points along the entire interval of output currents of the system. Just like in the experiments before, it was necessary to let the FC stack warm up to its operating temperature, before starting to gather data.

The relevant variables from the stack were measured, and the corresponding output conditions at the load were recorded as well. Firstly, the current-voltage curve from this test is presented in Figure 4.9a, alongside the benchmark curve develop in Section 4.1.2. Next to it, in Figure 4.9b, the efficiency of the stack is shown, calculated from the hydrogen flow measurements.

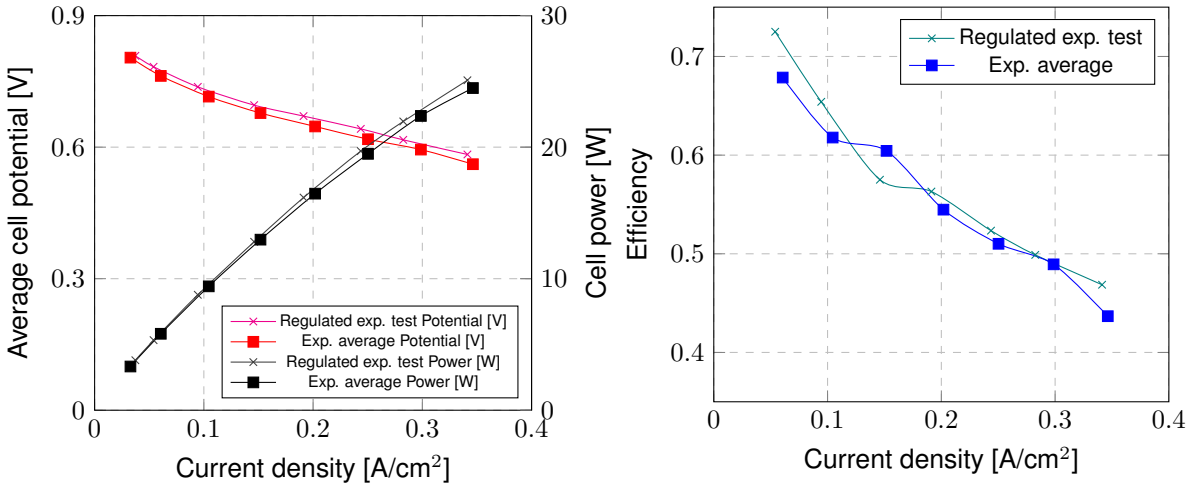

(a) Regulated test current-voltage curve.

(b) Regulated test efficiency, with average.

Figure 4.9: Stack polarization and efficiency curves.

As it can be clearly seen, the stack behaved in a similar way to before. The voltage readings were just slightly above the average polarization curve, and the efficiency values in which it was operating was in line with previous tests. This results are natural since, regardless of the operating mode, the FC stack always operates along its characteristic curve, providing the same voltage output for the same current request. The difference between this operating mode, and the unregulated one previously used, relies with the way the power is delivered to the load, passing through a converter, and being combined with a battery, before being outputted.

Given this fact, it is relevant to analyze the values for the different variables at the load. As the range of current values was swept, the voltage measured by the load remained fairly constant, as shown in Figure 4.10a. This behaviour is according to what was expected from this configuration, since the output power, connected to the load, is in parallel with the backup battery of the system and, therefore, that is the value that was being felt at the electrical load. For most test points, this value remained around 13.5 V, with the notable exception of the highest current test point. For this last point (which was the first to be measured, as the current was first set to the highers value, and then gradually decreased) the potential

was visibly lower, at 12.4 V. This meant that, at such high current demands, the battery voltage dropped, as it discharged.

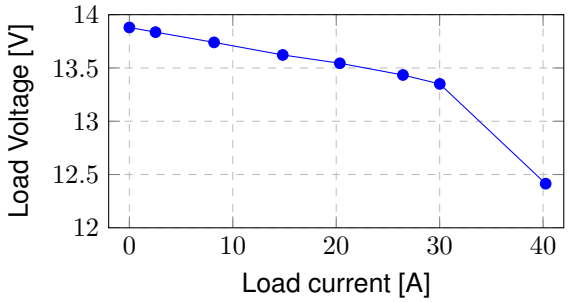

(a) Programmable load voltage, in regulated mode test.

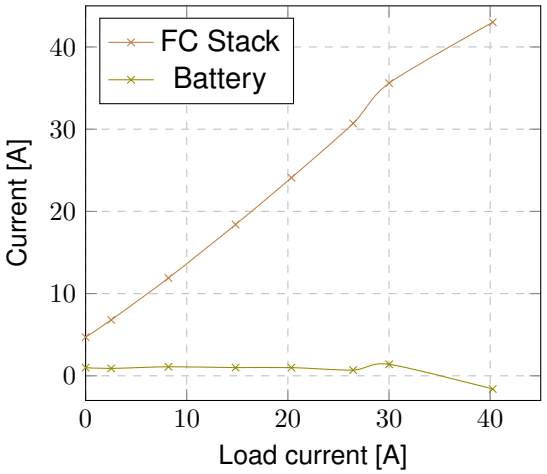

(b) Stack and battery current behaviour, in regulated mode test.

Figure 4.10: Voltage and current curves, in regulated mode.

To analyze the current behaviour of the system, Figure 4.10b is provided. In this plot, the relationship between the current received by the electrical load, and the one provided by both the FC stack and the battery is provided. As can be clearly seen, the current demand is essentially covered by the fuel cell stack. The battery showed a constant current, of around 1.0 A throughout most of the test. Once again, the exception to this behaviour is the highest current test point, in which the battery current showed a negative value. This corresponds to a charging state for the battery. In this case, as the battery discharged for the high power demand (as shown by the corresponding voltage value), the system automatically recharged it, using the available power produced by the fuel cell.

The behaviour observed during this test, confirms the power management strategy used by the internal controller of the system. This corresponds to a charge sustaining philosophy, in which, as the name indicates, the state of charge of the battery is maintained, consuming power generated by the fuel cell if necessary. This energy management strategy is what allows the system to have a constant output voltage. Moreover, the existence of the battery in a constantly charged state means it can provide backup power whenever necessary. This contrasts with a possible charge depleting strategy, in which the battery state of charge would be allowed to be depleted, making most use of previous external charging [27].

4.2 Propulsion Tests

After the previous round of testing was completed, it was time to utilize the fuel cell power in a propulsion application. For such, it was necessary to connect the FC system power output to an appropriate EM and propeller. As mentioned in Section 3.2, three motors, with different characteristics, were tested. First, the tests were performed using batteries, to have a reference against which the FC testing could be compared. Then, the fuel cell system was used to power the motors, in both regulated and unregulated output mode. The tests performed were all static thrust tests, as both the motors and the ambient air around them were at rest. No dynamic tests were conducted.

The tests could be performed using the thrust test stands available at CfAR, which came in two

different sizes. The smaller one was used to test the XING motor, as shown in Figure 4.11a. It was the RCbenchmark motor test stand, 1580 series, and was operated using the same company's software. It could handle up to 2 kgf of thrust, and a maximum current and voltage of 40 A and 35 V, respectively. For the larger EMs, a bigger custom test stand was used, which had been previously developed at CfAR to perform this type of propulsion tests, along with the necessary LabVIEW VI to operate and record data. Given stress analysis made at the time of development, it should be able to handle more than 80 N of thrust. This test stand, with the E-flite motor installed, is in Figure 4.11b. Both setups allowed to measure the electrical power feeding the EM, giving voltage and current readings, as well as the thrust force and torque they were applying in the test stand. Along with the time, these were the main parameters measured. Given technical limitations, rotational speed measurements could not be made. In particular, the larger test stand did not have a functioning RPM sensor, while the smaller test stand did have a sensor, however the ESC used did not allow for the connection to the sensor to be made.

As mentioned, both test stands had their own associated software that allowed for the motors to be operated. Firstly, they required the operator to select the safety thresholds for the voltage and current supplied. Then, the ESC could be enabled and, according to the desired throttle percentage, the appropriate PWM signal would be generated and provided to the motor. The data measured by the different sensors in the test stands could easily be recorded and saved in an spreadsheet, for later analysis.

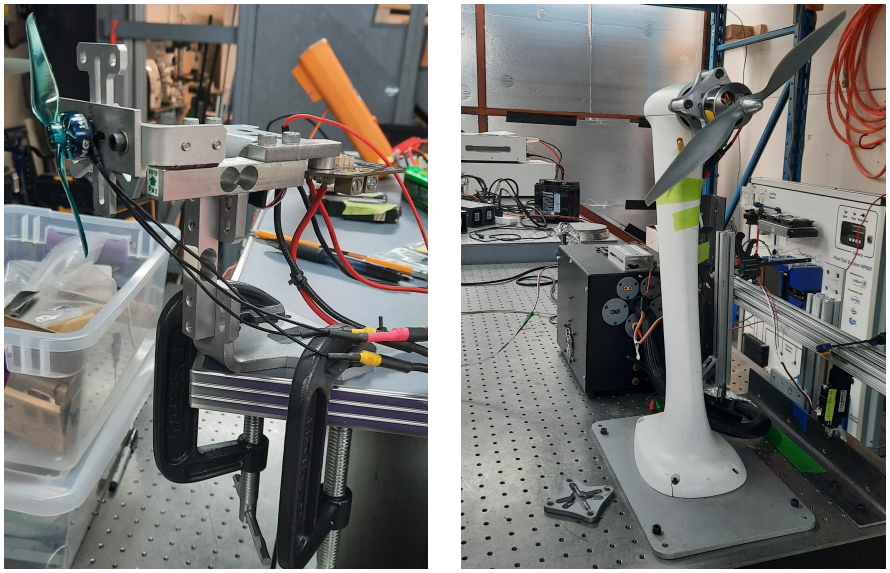

(a) Smaller test stand, with XING motor; **(b)** Larger test stand, with E-flite motor;

Figure 4.11: Static thrust test stands used.

4.2.1 Battery Testing

The first tests conducted used Lithium Polymer (LiPo) batteries as a power source, to measure the EMs performance. Given the FC stack average potential, both 3S and 4S batteries were used, to obtain results in the relevant range. This means that the batteries had 3 and 4 cells, respectively, translating to nominal voltages of 11.1 V and 14.8 V. To verify the repeatability of the results, and the reliability of the motors performance, each test was conducted at least two times. In the case of the XING motor, the test was even repeated with a second motor, as there were several of the same model available.

During each test, the throttle was successively increased from 0 to 100%, while the measured data was being logged. Each throttle step was set for a few seconds, to capture the steady motor behaviour,

and not just the transient phase. The steps were of either 5% or 10% (in the case of the XING motor), depending on the software used to communicate with the ESCs and EMs.

For each of the three EMs tested, the thrust generated, as a function of the throttle percentage, is presented in the plots of Figure 4.12. For each throttle value, the corresponding thrust shown is the last value measured for that throttle step, to capture the steady-state value. The error bars present in the graph show the variation in the force measured during the time interval in which each throttle step was requested. The first couple of test points for each request were not considered, as they were clearly in a transient phase. It is important to notice that the units for thrust presented are the ones in which each test stand gave its measurements: kilogram-force for the smaller stand (with the conversion to Newton in the right side), and Newton for the larger one. Moreover, while the XING motor presents positive values of thrust, the other two show negative values, with the axis direction flipped to be easier to visualize its behaviour. This is simply because, for these latter ones, the propeller was installed in a pusher configuration, for safety reasons, to prevent the risk of this component uncoupling from the motor during the tests. Since on the XING motor the propeller was bolted to the EM this was not a concern and, therefore, a traditional puller configuration could be used.

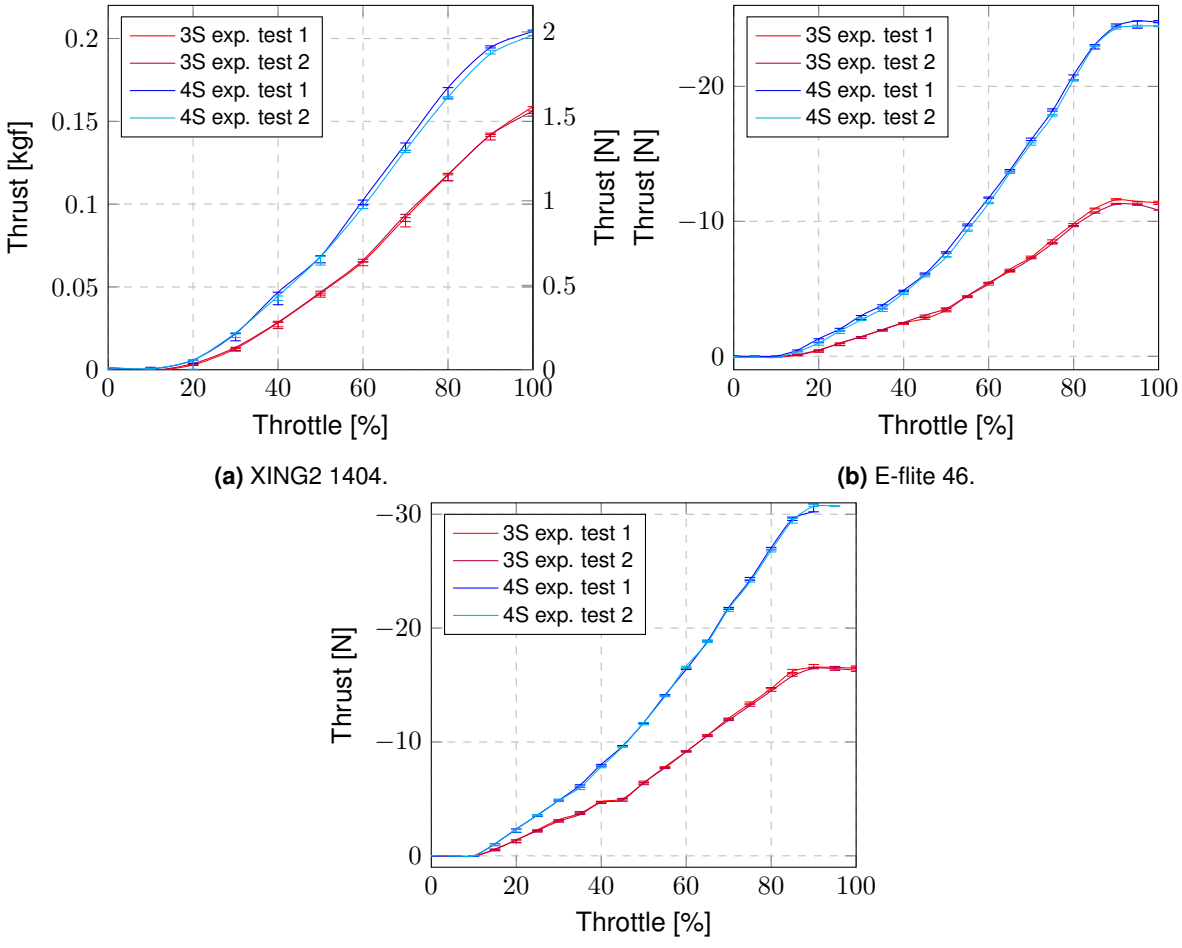

(a) XING2 1404.

(b) E-flite 46.

(c) AXI 2826/10 Long V2.

Figure 4.12: Thrust curves, using batteries as power sources.

The first thing that can be taken away from the previous data is the consistency between the two tests performed with each type of battery, given that the different tests present reults within each other's error bars, which themselves show a small interval of thrust fluctuation. This gives confidence that the results are correct and, as it was confirmed that for the other parameters both tests show similar data

as well, from here onwards only the test data from the first experimental test for each battery type will be shown, as a representative behaviour for the motors with this power source.

None of the motors produced any thrust for the lowest throttle settings. Only around 15% did they start rotating, and generating any force. In the case of the E-flite and AXI motors, it is also visible that their performance maxed out at around 90% throttle. This, however, does not correspond to the maximum thrust output the EM is capable of providing. For example, when tested using a 3S battery, the maximum thrust reached was 11.5 N, for the E-flite motor, while it is evident that the motor can produce more thrust, as was seen in the 4S tests. This seems to be due to the way the ESC used functions, and is in line with other tests performed at CfAR with the same ESC (Castle Phoenix Edge HV 120). This effectively means that the useful range of throttle that can be used is from 15 to 90%. On the contrary, the XING motor, which was tested using the T-Motor Flame 70A LV ESC, shows an increase in thrust right until the last throttle step, to 100%.

Another interesting aspect to address is the difference in thrust achieved when using the 3S and the 4S battery. As it is natural, the thrust generated when using the lower voltage batteries was below the one during the 4S tests. As explained before, the voltage supplied to an EM is essentially related to the rotational speed of the motor, which, in turn, reflects on the torque necessary to spin it, and the thrust it generates. Given the way the PWM signal is generated for different throttle percentages, the average voltage for different points in the 3S and 4S curves can be compared. For example, when looking at the maximum thrust achieved by the XING motor using the 3S battery, it is 0.154 kgf, which, by looking at the plot in Figure 4.12a, seems to be about the value the 4S curve would have at 75% throttle. By taking the average between the 70 and 80% test points, in the 4S curve, it is confirmed that a 0.153 kgf can be estimated. By analyzing the voltages in this respective points, it was verified that, for the 3S battery, the voltage was of 11.94 V, which is 75.8% of the estimated 15.76 V the 4S battery would be supplying in the mentioned throttle percentage. Moreover, given that the 3S battery has 3 LiPo cells, while the 4S has 4, it is evident that the the maximum voltage of the 3S battery is 3/4 of the one provided by the 4S, therefore these values observed are natural. This confirms that, when supplied with the same average voltage, the EM produces the same thrust, as it is spinning at the same speed. Similar results can be found for the other motors.

Besides these considerations, the measured data can also be compared with the available data taken provided by the manufacturers. Starting with the XING2 1404 motor, its specifications sheet can be found in [89], and is presented in graphical form in Figure 4.13, along with the experimental data. Given that the 4S battery had a similar voltage to the one used as a reference in this documentation (16 V), it would be expected that the EM would produce a maximum thrust in line with the one present there as well (0.489 kgf). However, it only reached a maximum value of 0.204 kgf, while being powered by 15.23 V. This value is only 41% of the reference given by the manufacturer. It is important to note that the propeller used for testing this motor was the same as the one on the specifications data (T4030). Given this fact, it was also noticed that the motor was not consuming as much current (and power) as described by the manufacturer. These were, respectively, only 65% and 62% of the maximum current and power presented in the specifications. This means that, when compared with the data made available in the manufacturer's website, the XING motor was consuming significantly more electric power for the same amount of thrust, and overall producing a maximum thrust much smaller than advertised. For the test points between 60 and 80% throttle, the power consumed by the motor is essentially the same as indicated by the manufacturer (only about 6 to 9% smaller), but still, the thrust output is about half of what would be expected. As the tests were performed with two different motors of the same model, with similar results, this does not seem to be a manufacturing issue specific to the EM tested. It is also consistent with previous tests performed at CfAR with different EMs from the same manufacturer, which also seemed to be underperforming, only outputting about 40 to 50% of the thrust indicated on their

online specifications.

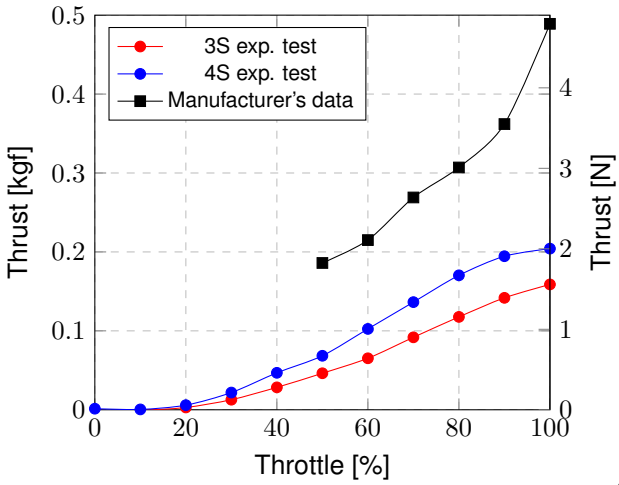

(a) Experimental thrust generated, with manufacturer's data.

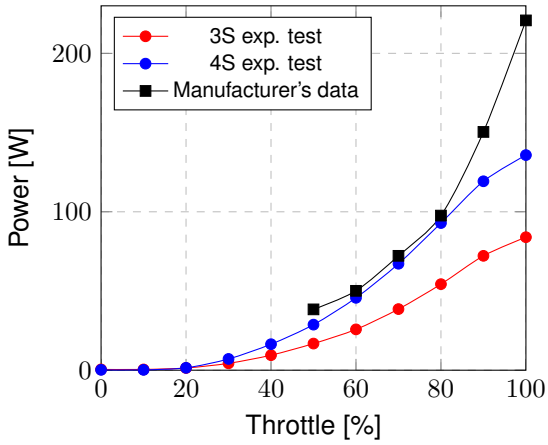

(b) Experimental power consumed, with manufacturer's data.

Figure 4.13: Thrust curves and power curves, for the XING motor.

As for the E-flite motor, the information given by the manufacturer, available in [90], does not mention the maximum thrust the motor can generate. It does, however, give values for current and power. With these in mind, the plots in Figure 4.14 are introduced, which contain the current and power behaviour for the motors tested. Particularly, Figure 4.14b shows the data for the E-flite motor. It can be seen that the maximum current drawn had the value of about 30 A, corresponding to an electrical power of 440 W. These values are below the ones presented by the manufacturer, for the same voltage, which go above 40 A. However, the test data provided by the manufacturer was taken using a larger propeller, with 13 in, while the one tested had 12 in, as previously mentioned. This justifies that, to rotate it, a smaller torque would need to be provided by the motor and, therefore, less current would have to be drawn.

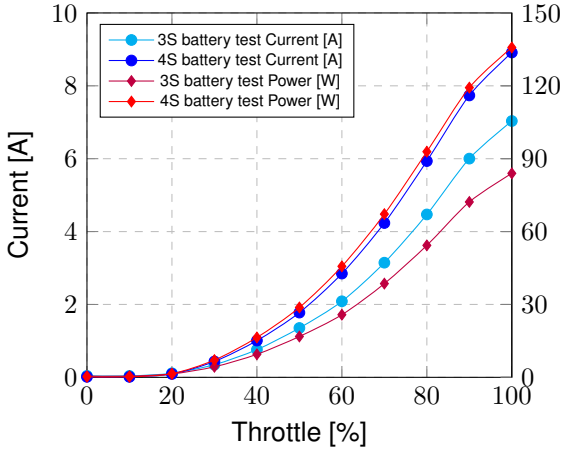

(a) XING2 1404.

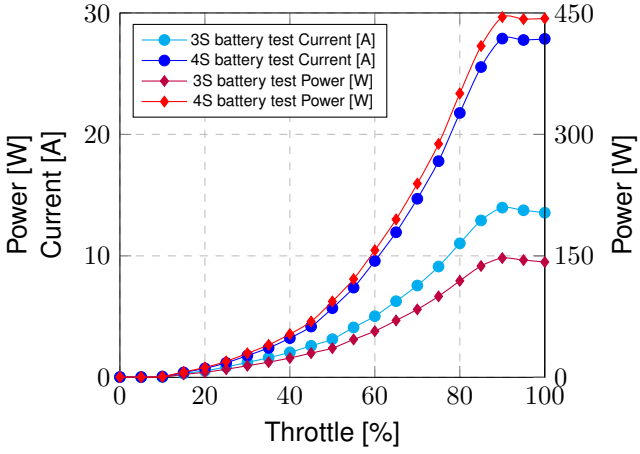

(b) E-flite 46.

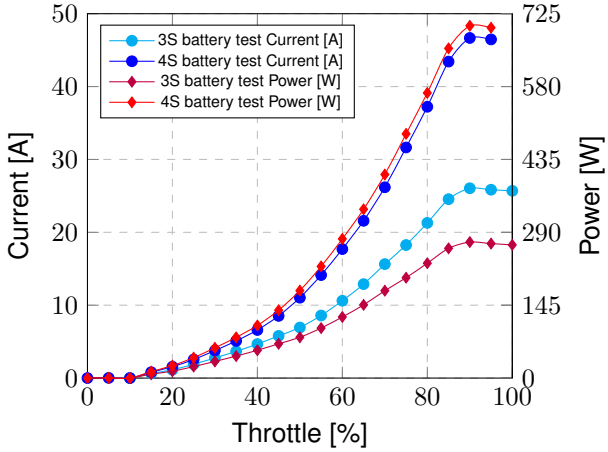

(c) Axi 2826/10 Long V2.

Figure 4.14: Current and power curves, using batteries as power sources.

The AXI motor also had a recommended propeller slightly larger than the one used, as can be seen in the manufacturer's website, [91]. However, even with this smaller 12 in propeller, the maximum current of the motor was reached when using the 4S battery in the higher throttle settings (90-95%), for which the ESC reaches the maximum power delivered to the EM. A current as high as 46.5 A was reached for this higher throttle setting. After about a second and a half sustaining this value, the testing software cut off the power to the motor, as it was above the continuous current threshold set for this motor. The power, however, did not go above the specified maximum of 740 W, having only reached about 700 W. No further information is provided by the manufacturer to compare to.

To confirm the dependency between torque and current, the plot in Figure 4.15 is presented. This

plot in particular shows data from the 4S battery test for the AXI EM, but the results are similar for the other tests. Once again, as a pusher configuration was used in this test, the torque values are negative, but the axis is flipped for easiness of reading. The data seems to show a slight non-linear behaviour, particularly for the lower torque and current values. This can be attributed to the typical lower efficiency that EMs have for very low rotational speeds and torque. The latter test points can be well adjusted to a linear trendline: considering only the points with a current grater than 7 A, the trendline had an R^2 equal to 0.991. The test points that deviate the most from this line correspond to the transient phase, when the EM was drawing more current to accelerate, before stabilizing at a lower value. The main value that can be taken from this fitted line is its slope, which has the value of (negative) 0.0091. Theoretically, it is known from equation 3.3 that this slope is $1/K_v$. This motor's K_v was 920 RPM/V, or 96.342 rad/sV, which gives a calculated theoretical slope of 0.01038. Therefore, the experimental value shows an overall deviation from theory by 12%. The other EMs showed similar behaviours, with both types of batteries tested.

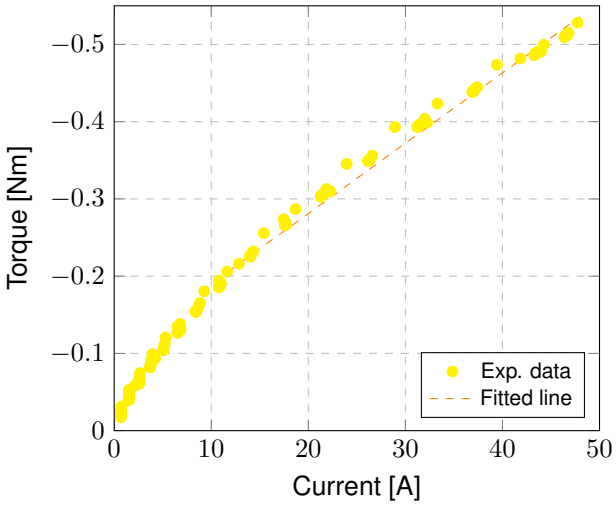

Figure 4.15: Torque current dependency, for the AXI 2826 motor, using a 4s battery as a power source.

Finally, it is just important to realize that, from the data collected during these battery tests, the power and current necessary for these EMs tested is, in general, within the capabilities of the fuel cell stack, previously determined. This gave confidence that the stack was in good conditions to power these motors, and allowed for the next round of testing to begin, as described in the following section. The exception would be the maximum power drawn by the AXI motor, which is above what the fuel cell is capable to provide. This is due to the fact that, for the high current values observed, the voltage of the fuel cell is significantly below that of a 4S battery. This already shows one of the limitations of the fuel cell used, as a mean to power EMs.

4.2.2 Fuel Cell Testing

After this initial tests, to set the benchmark EM performances, it was time to use the fuel cell stack as the power source for these motors. For this, the motors were tested in a similar way as before, but with the FC stack as a power source, in both regulated and unregulated mode.

Unlike with the previous fuel cell tests, which only had the programmable load consuming the electrical power produced, these tests had the stack connected to the ESCs and the thrust test bench sensors. Therefore, as discussed in Section 2.2.2, a diode was included to protect the FC from any possible reverse current. The diode used was a Vishay General Semiconductor VS-85HFR60, which could handle

a maximum average forward current of 85 A.

The tests proceeded similarly as before, with the fuel cell first being run for several minutes, for it to warm up to its operating temperature, before beginning the data gathering. Firstly, the smaller and less powerful XING motor was tested, and only later the E-flite and AXI motors were connected to the FC. For each EM the regulated power mode of the fuel cell system was used in the first propulsion test, followed by the unregulated power mode. Between each test round, the fuel cell was left running for about 10 minutes, to allow for the temperature and humidity re-stabilize to its operating point. This way, the FC was in similar conditions before each test was performed.

The thrust data collected during these propulsion tests is displayed in Figure 4.16, alongside the previous values taken during battery testing.

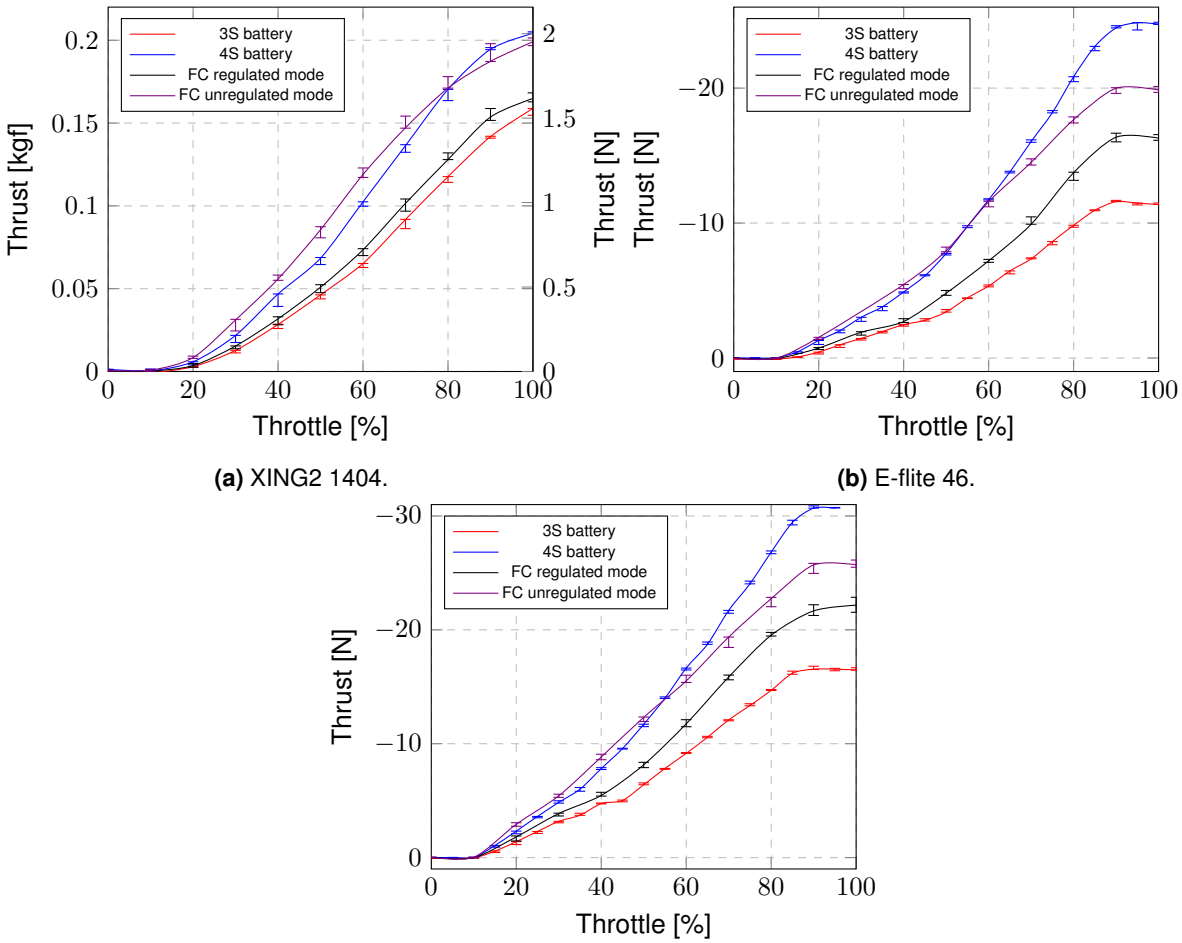

(a) XING2 1404.

(b) E-flite 46.

(c) AXI 2826/10 Long V2.

Figure 4.16: Thrust curves, using different power sources.

The three plots show generally a similar behaviour: the thrust generated when connected to the regulated power mode is in-between the performance for the two types of battery; while the unregulated power mode produces results that begin above the ones from the 4S battery, but a lower thrust is generated for the highest throttle settings. Once again, this behaviour can essentially be explained by the difference in voltage each power source is able to provide. Therefore, it is important to visualize the voltage supplied to the EMs during these tests. As an example, Figure 4.17 shows the data for the tests using the E-flite motor, which is in line with the other motors.

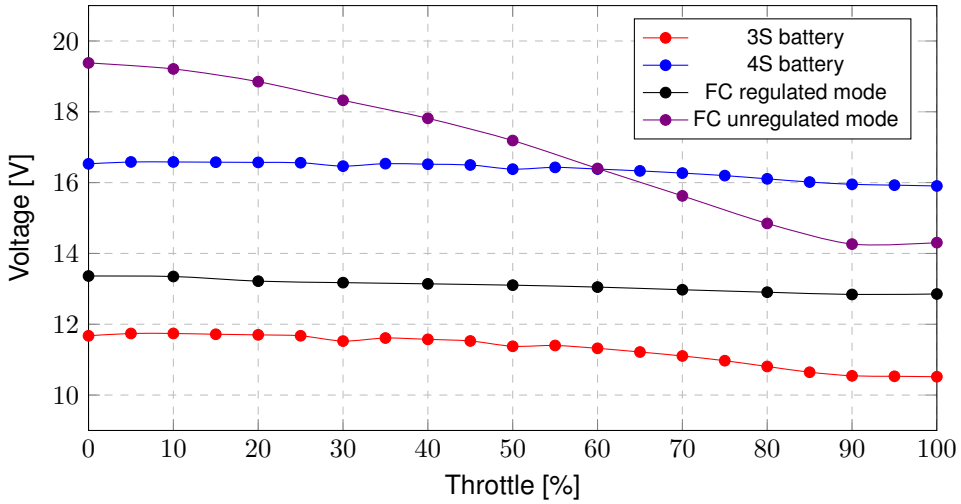

Figure 4.17: Voltage observed during the thrust tests on the E-flite 46 motor.

It can be clearly observed that both batteries and the regulated power mode of the fuel cell show little variation in the voltage they supplied to the motor. Out of these three, the 3S battery is the one that shows a larger voltage drop, of about 1 V, while the others decrease only 0.5 V. On the other hand, the unregulated power mode had a much greater voltage variation throughout the test, dropping 5.1 V from 19.4 V when there was no load, to 14.3 V at maximum throttle. The difference in the behaviour of these two modes of the fuel cell system can be justified by the way they operate.

When the electric load is connected to the regulated power mode, it is in parallel with the backup battery of the system. As previously discussed, this ensures a very low variation in voltage output, which remained close to 13 V. This value, which is in-between those of the two batteries, explain why the thrust observed with this power source was slightly higher than the one using the 3S battery, but still well below that of the 4S battery.

In the case of the unregulated output mode of the system, the electric load is connected directly to the terminals of the FC stack. The stack, as was observed in Section 4.1.2 has a much greater drop in voltage, as the current increases, than a LiPo battery, from above 19 V with no load, to below 13.5 V at maximum power. During the test with the E-flite motor, as the current drawn was not the maximum the stack can produce, the lowest voltage observed was slightly above that minimum. It was still, however, lower than the voltage of a 4S battery, which justifies that the thrust generated at maximum throttle was below the one observed using this type of battery. For the lower loads, as the stack voltage is closer to that of a 5S battery, the thrust created was the highest among the 4 power sources, even if the difference is small, given the low throttle command. The point where the stack voltage drops below the 4S battery is at 60% throttle, which corresponds to the point in Figure 4.16b where both thrust curves intersect, as expected.

It is also worth remembering that, even in the unregulated power mode, where the load is connected directly to the stack, the voltage and current of the stack are not exactly the same as the ones being supplied to the motors. These losses have already been discussed in Section 4.1.2.1, but it is worth noticing that additional losses are introduced by the diode, that were not present before. The voltage felt by the motors was usually about 0.5 V lower than the stack's voltage, and the current was around 5 to 6 A lower. Still, the AXI 2826 motor, as the only that covered the full current range of the FC, was consuming over 500 W of power at full throttle, which was observed as the maximum that could be provided to an electrical load connected to the FC system.

Figure 4.18 contains the data relative to the fuel cell data taken during these propulsion tests. Once again, it can be confirmed that the FC operates along the polarization curve previously determined, in

both operating modes. Most test points are in the lower load region of the plot, as the current drawn was generally small. Only the AXI motor truly used the full range of current of the stack.

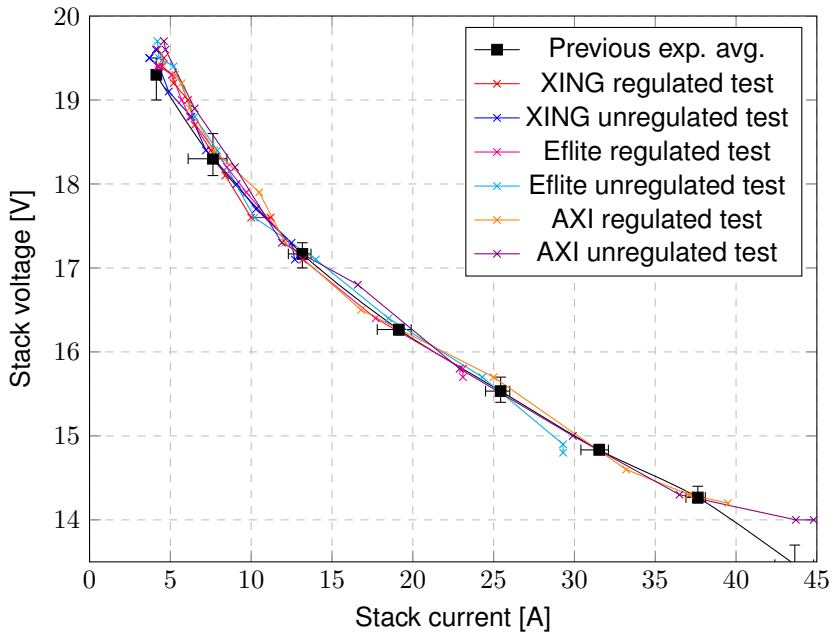

Figure 4.18: Fuel cell current-voltage behaviour during the propulsion tests.

4.2.3 Response Time

One other aspect that was analyzed, besides the stationary response of the motors in each throttle setting for the different power sources, was the transient response, in particular the time taken by each source to deliver the necessary to the EM.

With this purpose the AXI motor was tested, in the same test rig as previously, using the 4S battery, as well as both operating modes of the fuel cell system. The PWM signal was changed to produce 50% throttle, from zero, without any steps. The time response was recorded, at a rate of 10 Hz. In Figure 4.19 the plots for the thrust and power delivered to the motor are presented, for the time around the 50% throttle demand.

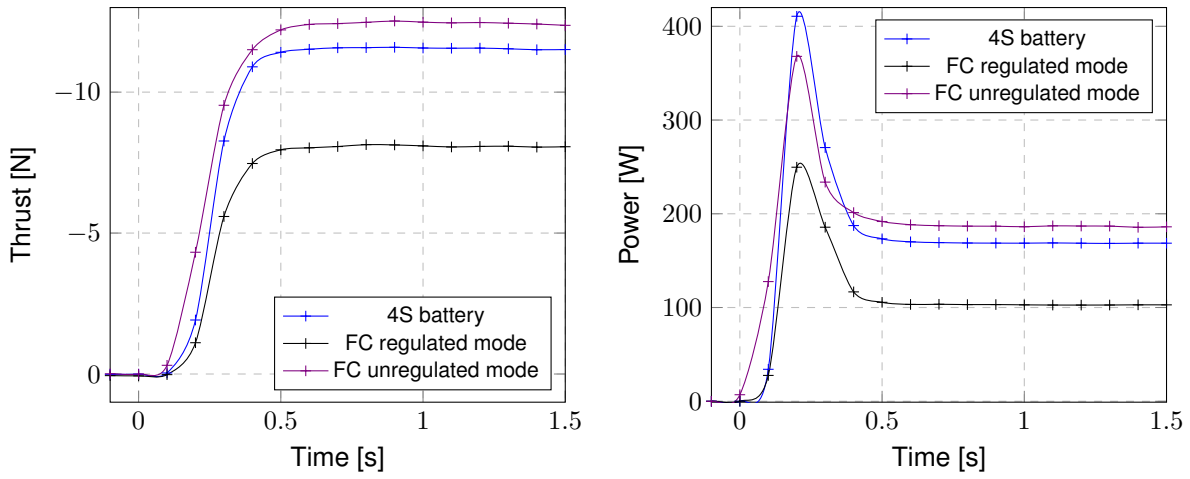

(a) Thrust transient response.

(b) Power transient response.

Figure 4.19: Time transients, for the AXI motor, for 50% throttle and different power sources.

As it can be clearly observed, for this power demand, there does not seem to be a significant difference in the time response for the motor when powered by the three different sources. As discussed previously, given the different voltage of each source, the thrust reached for each is different, however the time interval for the EM to reach such value is essentially the same. By 0.5 seconds after the new throttle demand, the motor has reached over 98% of its stationary thrust for the three power sources.

This behaviour can be achieved by a brief period where the power being supplied to the motor is very high, to accelerate the EM from its static position, before it reduces again to a constant value. In this case, despite having a lower stationary value, it can be seen that the peak power given by the 4S battery is higher than that for the unregulated mode of the FC system. Still, in all three tests the power was within 3% of its final value by 0.5 s.

Even with these results, it can still be observed that the FC system, in its unregulated mode, is slightly slower than the LiPo battery and the regulated mode (which also uses a battery). Mainly, the 4S battery is able to reach a higher peak value for power faster, and then reduce again, reaching less than 0.5% error from its stationary value in 0.7 s, while the stack takes about 1 second. While it is a small difference, it is important to notice that it would probably grow bigger if the power demand had been higher. In particular the battery is able to provide more power than the FC stack: in previous tests nearly 720 W peak power was reached for the battery, while the FC system can deliver little more than 500 W. Thus, if the burst power necessary to accelerate the motor had been much higher, the stack would reach its maximum power more easily, possibly slowing down the acceleration phase for the EM, which would not happen as soon if a battery was being used.

4.3 Hybrid Tests

Following the previous propulsion tests, the fuel cell stack was tested as a power source in a hybrid system. Similarly to above, the FC system was used to power an electric motor. However, this motor was not directly connected to a propeller, it was instead integrated in the hybrid test bench configuration, described previously in Section 3.3.

The fuel cell system was connected to the side B of the test bench, where the smaller AXI motor was installed. Given that the motor is designed to be powered by a 6S-8S LiPo, corresponding to 24-32V, the regulated power mode was not tested due to its low voltage (the ESC would not even activate when this output was used). Side A of the test bench was powered using two 6S batteries, connected in series - corresponding to a 12S battery. To begin the test, the stack was first warmed up as before to its operating temperature. Then, the FC system could be connected to the hybrid test bench, while the programmable load, used to heat the system, was connected to the test bench to dissipate the power generated by the dyno.

For each test, a full throttle sweep of side B was performed, with 10% steps. As for side A, the throttle started at 20%, given that there was no activation for a lower setting, and was increased to 30% and then 40%. To avoid overspinning side B, higher throttle settings were not used. Given that the FC cannot be connected to an external power input and store its power akin to a battery, the regeneration mode was not explored, only the hybrid mode, with both EMs producing mechanical power. Each test was conducted once, the test bench data was logged automatically by the associated VI, at a rate of 20Hz, and the stack variables were recorded manually, as previously. As the programmable load was being used for the test bench, the FC stack could not be reheated in-between tests, so they could not all be performed at the same starting temperature. Throughout the tests the stack temperature was monitored to verify how it was changing as time went on. The first test runs were unloaded, so the programmable was not drawing any current from the system. Then two loads, of 5 and 10 A were tested.

As this experiment represents the final hybrid integration that was the goal set out at the beginning of this work, the results from the tests with the different loads and side A throttle setting will be presented and analyzed in the following section.

Chapter 5

Results

This section presents the data gathered during the hybrid tests performed. It includes both the data logged by the hybrid test bench, as well as the one measured by the fuel cell system used to power it. The data is presented in graphical form to enable visual interpretation of the results.

The data shown for each throttle step refers to the steady value of each parameter, with the error bars indicating the time variation present in each step. In the case of the hybridization degree, which had to be calculated, the error was determined based on equation 5.1 [92]:

$$\sigma_w^2 = \left(\frac{\partial w}{\partial x}\right)^2 \sigma_x^2 + \left(\frac{\partial w}{\partial y}\right)^2 \sigma_y^2 + \left(\frac{\partial w}{\partial z}\right)^2 \sigma_z^2 + ... \tag{5.1}$$

where w is a function of the independent variables $(x, y, z, ...)$, and their errors are, respectively, σ_w, σ_x, σ_y, σ_z, ...

Here, the hybridization degree was defined as the ratio between the side B electrical power (from the FC) and the total electrical power supplied to the system (which came from both the FC and the batteries connected to side A). Therefore, the expression for the hybridization degree error is given by equation 5.2:

$$\sigma_{hyb.degree} = \frac{1}{(P_A + P_B)^2} \cdot \sqrt{P_B^2 \sigma_{P_A}^2 + P_A^2 \sigma_{P_B}^2}, \tag{5.2}$$

or this value multiplied by 100 for the value in percentage.

Besides this data analysis, a brief discussion of possible aircraft integration will be included. It aims to determine the mass and volume penalty a fuel cell system would impose, and the endurance gain it could achieve for a particular UAV.

5.1 Fuel Cell Performance

Before delving into the data gathered by the different test bench sensors, the fuel cell behaviour was analyzed and compared to previous observations. With that goal, Figure 5.1 shows the FC's voltage and current for each test, in the order they were performed.

Here, the most obvious aspect to notice is the considerably lower voltage observed in these hybrid tests, when compared to the polarization curve previously determined. However, given the propulsion tests performed before, it is known that the fuel cell did not change its behaviour significantly when powering EMs. This indicates that the difference must lie with the initial conditions in which each test was conducted.

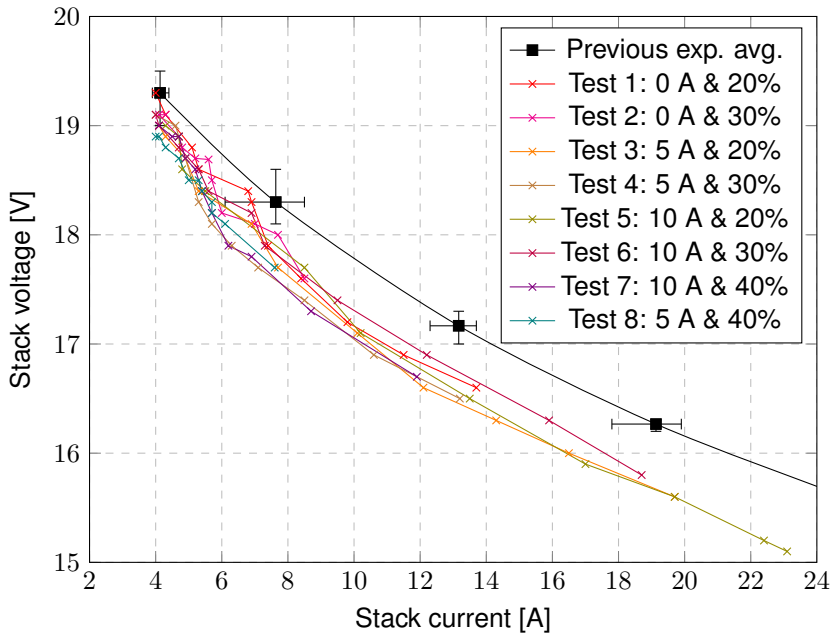

Figure 5.1: Fuel cell current-voltage behaviour during the hybrid tests.

As mentioned in the hybrid test procedure description, for these experiments the programmable load had to be used for the hybrid test bench and could not be connected to the FC stack to warm it up in-between tests. Therefore, given the relatively low current being drawn, the temperature of the stack steadily decreased throughout the tests. In fact, the first test was already performed at a temperature of 47.8 ℃ (instead of the 55 ℃ of previous tests), and only two tests could be run before the temperature of the FC stack dropped below the lower limit given by the manufacturer for operating temperature (45 ℃). By the end of the eight tests, the temperature measured by the stack was as low as 40.6 ℃.

Therefore, due to limitations in the available equipment, it was not possible to perform these tests in the same starting conditions as the previous ones. This, in turn, affected the fuel cell performance, showing a current-voltage curve that is consistently below the one obtained for operation at 55 ℃. For the smallest current (at 0% throttle), for example, the first test showed a stack voltage of 19.3 V, in line with the previous average, but that value became smaller as the tests progressed, with only 18.9 V in the last one. The voltage difference between the curves also grows larger, as more current is being drawn, to about 0.8 V of difference for the largest current observed. While this may represent only about 5% of the total voltage of the FC, it is still a much higher variation in performance than what is observed when the fuel cell is operating consistently at the same temperature.

This behaviour points to the need for a better thermal management strategy, possibly with some heating system, alongside the existing cooling system. While this would naturally add complexity to the setup, a future hybrid integration could try to explore synergies with the other components (batteries, electric motors), by taking advantage of the excess heat generated by these elements.

5.2 Unloaded Tests

In the first couple of tests conducted, there was no load demand from the system by the programmable load. Therefore, as no electrical power was being generated by the dyno, all the power being supplied to the system was being dissipated mechanically. This meant that the electrical motor on sides A and B were only consuming enough electricity to overcome the rotational friction between

the different components of the test bench, as well as the power dissipated on the EMs' coils. For these tests, Figure 5.2 shows the different parameters measured by the test bench sensors.

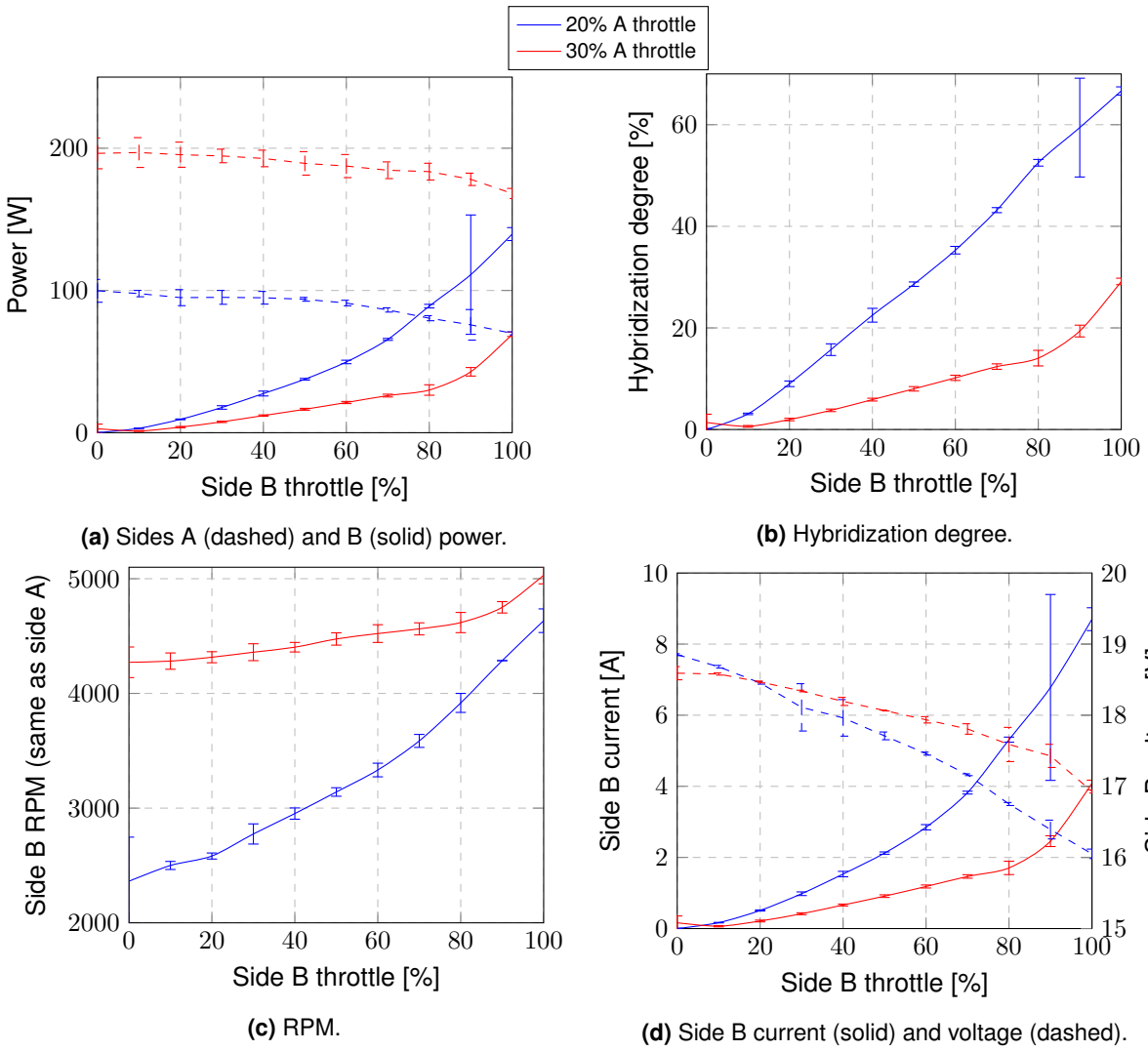

(a) Sides A (dashed) and B (solid) power.

(b) Hybridization degree.

(c) RPM.

(d) Side B current (solid) and voltage (dashed).

Figure 5.2: Test bench variables for the unloaded hybrid tests.

Unlike what was done in the following tests, the side A throttle was not increased beyond 30% when the system was unloaded. This was because, for this throttle setting, the degree of hybridization was already quite low, only at around 30%. Increasing the side A throttle even further would only reduce the overall influence of side B and would result in uninteresting results. Given this, the general trend of the data, with the increases in both A and B throttle will be better described in the loaded tests, as they have extra data points to show these trends.

For these tests the most important thing to note is that it shows how much power the system needs to consume to rotate without any load being applied. Without load, all the power is being consumed mechanically, and corresponds mainly to the power necessary to overcome the rotational friction between components, and to the one dissipated on the coils of the two motors. This value, naturally, is not constant, and increases as the rotational speed of the system increases. This increase in speed derives from the throttle increase or, in other words, the increase in average voltage feeding the EMs. For the fastest rotation observed, of about 5000 RPM, the electrical power being consumed was around 240 W. This, however, was essentially sustained by the batteries' power, since, as previously mentioned, the hybridization degree was only 30%. The highest power drawn from the FC stack in these tests was 140

W, or about two-thirds of the power necessary to spin the system at 4600 RPM with 20% side A throttle.

Regarding this power consumption, it can be analyzed more precisely how it is being consumed by the hybrid test bench system. With the torque values calculated based on the forces measured by the load cells the mechanical power can be determined given the product between torque and rotational speed (in rad/s). This power split is plotted in Figure 5.3.

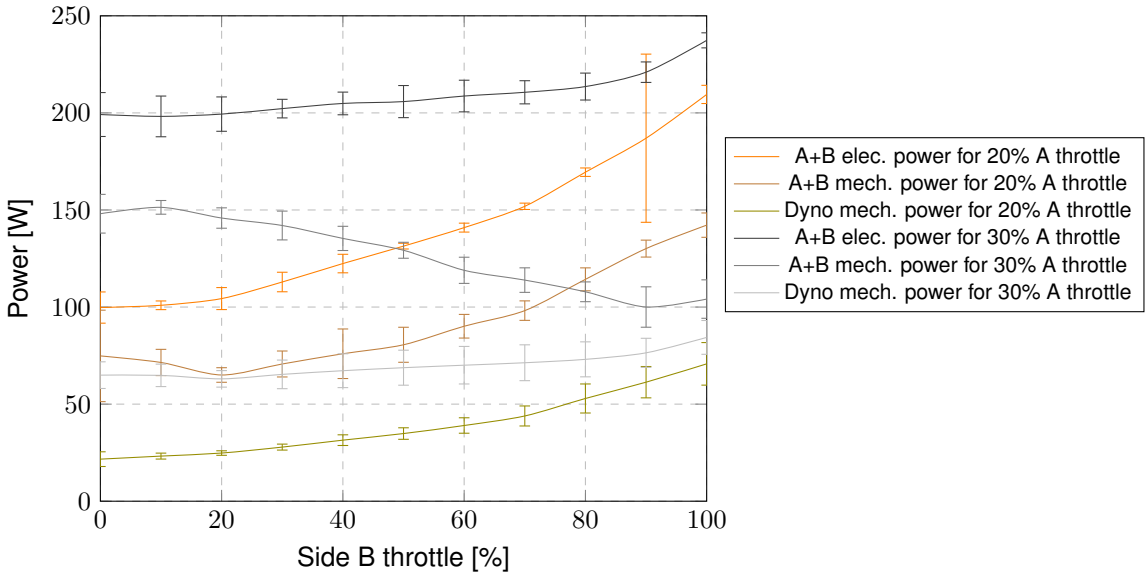

Figure 5.3: Power for the unloaded hybrid tests.

This graph shows an unexpected behaviour, for the 30% A throttle test. As the B throttle was increased, there is an increase in the total electrical power and the dyno mechanical power, but a decrease in the A+B mechanical power. For the 20% A throttle case the A+B mechanical power generally follows the trend of the electrical power, and increases with the throttle. This behaviour seems to be explained by the difference evolution in the rotational speed of the system for the two tests. In general, as the side B throttle was increased, the torque measured on that side (as well as side A) tended to decrease slightly, as the side B motor was no longer just being ”dragged” by the side A, and was actually contributing with power to the system. However, this decrease in the measured torque came with and increase in the RPM of the system. For the test with 20% side A throttle, this increase in rotational speed if very significant, and makes up for the torque decrease, resulting in an overall increase in the mechanical power generated. The other test, however, has a much lower RPM increase, resulting in an overall decrease in the mechanical power (the last test point, where the RPM increase is greater, is an exception to this).

Still, overall the output mechanical power of the dyno follows the same trend as the electrical power supplied to the system. As there was no electrical load, the mechanical power at the dyno was simply the result of its internal friction, which applies a low counter-torque on the system. The permanent gap between the input power and the dyno power points out to the transmission inefficiencies of the system, and the electric power to mechanical power conversion by the motors.

Finally, it is also worth noting that, in general, all results have relatively small uncertainties. This attests the stability of both power sources, after the initial transient phase, showing little variation in each throttle step. The only exception is the large variation for the 20% side A throttle and 90% side B throttle results. In this test point the FC current did not stabilize, and kept great oscillations around its average value (which is in line with the other experimental values). The time variation of the current is plotted in Figure 5.4, which shows clear steps for the other throttle settings, but not for 90% (roughly from 95 to 105

seconds). These variations were too quick and irregular to reflect an oscillation in stack temperature, for example. Thus, it is not clear why this behaviour was displayed, since such an erratic performance was not present for any other throttle setting in this or other tests.

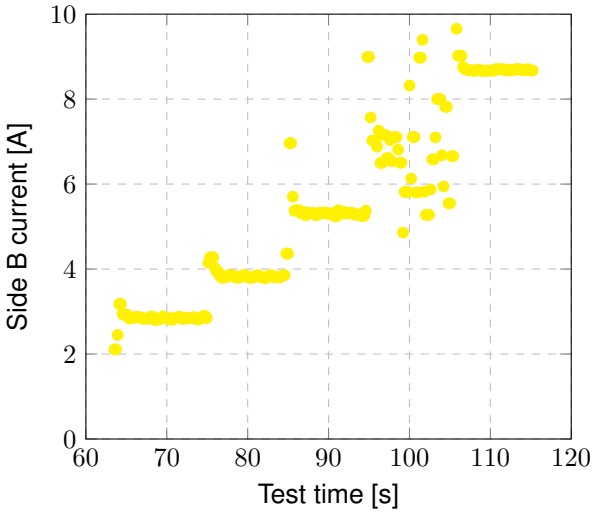

Figure 5.4: Current behaviour over time, for the unloaded 20% A throttle test, between 60% and 100% B throttle.

5.3 Loaded Tests

After these unloaded tests, the programmable load was set to consume electrical power being generated by the system: first set at 5 A and then 10 A, both DC. The data gathered in these series of tests are presented below.

5 A

Similarly to the plots for the unloaded test, Figure 5.5 contains the behaviour of the different variables for each throttle setting, in the loaded 5 A tests.

Here, the overall system behaviour can be analyzed. With the increase in throttle, for either motor, there was an associated increase in the system's rotational speed, as more average voltage was being supplied to the EMs. This, in turn, came with and increase in the power consumed by each motor. For each side A throttle setting, however, the power being consumed decreased when the side B throttle was increased, since more of the power needs of the system were being met by the side B EM. This translates to an increase in the hybridization degree with the side B throttle. Besides, the increase in the side B power came from a large increase in the current observed, while voltage dropped, in line with the fuel cell's polarization curve.

While this general behaviour is observed for all tests, it becomes less pronounced as the side A throttle setting was increased. Given the larger size of the side A motor, and the much higher voltage it was being supplied with, it is natural that as it was generating more power the whole system became less sensitive to variation in the smaller (and undervoltaged) side B motor. That is why no tests were performed beyond 40% side A throttle, as the side B influence in the system would further decrease, and to avoid overspinning side B.

When compared with the unloaded tests, the increase in the load changes the system's behaviour in predictable ways. Firstly, the power necessary to rotate the system increases, for the same throttle

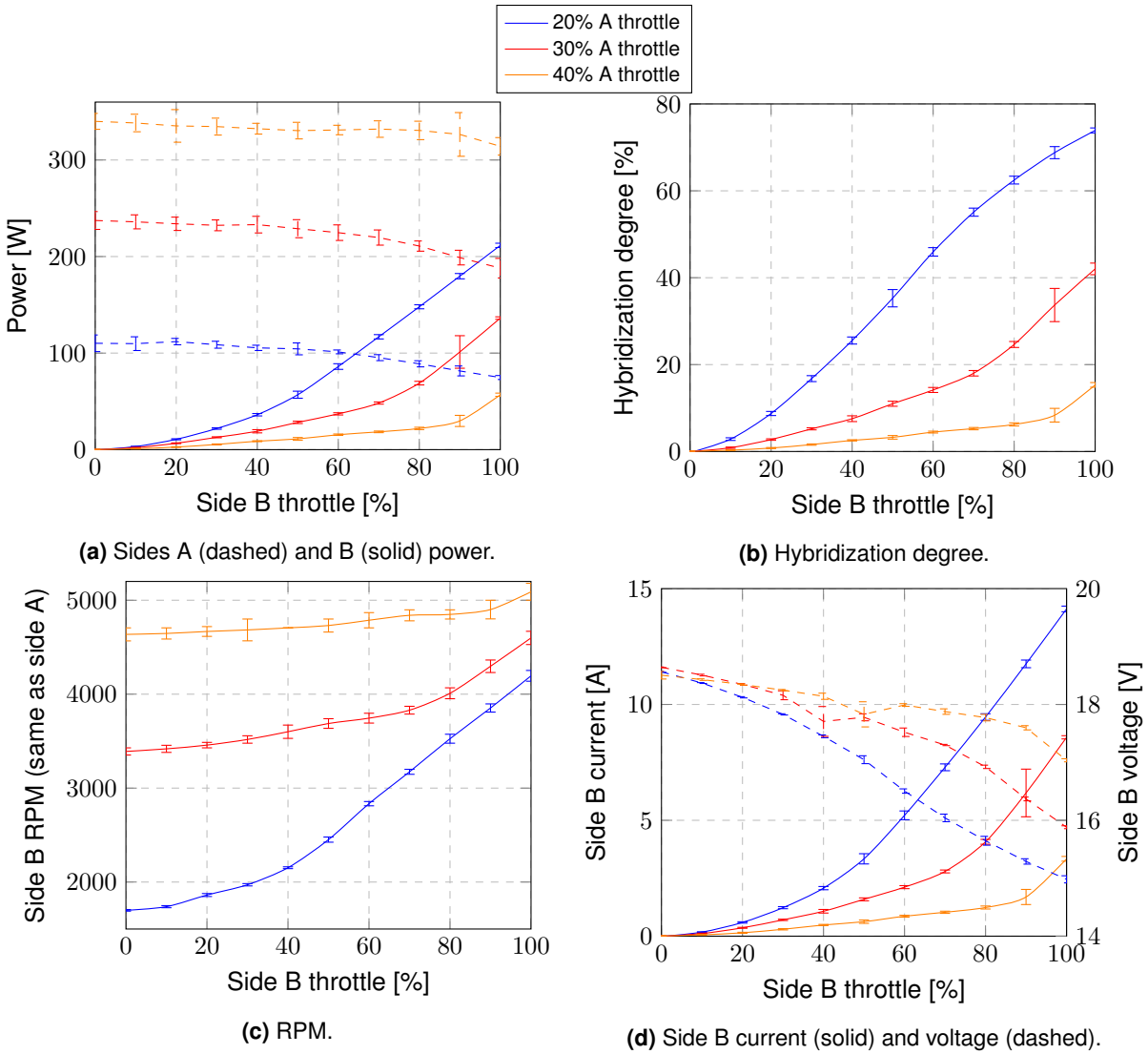

(a) Sides A (dashed) and B (solid) power.

(b) Hybridization degree.

(c) RPM.

(d) Side B current (solid) and voltage (dashed).

Figure 5.5: Test bench variables for the loaded 5 A hybrid tests.

settings. For side B, this increase in power comes from a significant increase in the current being supplied to the motor: for maximum B throttle and 20 % A throttle the current is now above 14 A, compared to about 9 A previously observed. Given the fuel cell performance, this comes with a drop in the voltage of several Volt, much larger than what would be seen in a LiPo battery.

As in these tests the dyno motor was functioning as a generator, the greater torque necessary to rotate the system translated to a decrease in the rotational speed of the whole system by several hundred RPMs.

Finally, with the increase in power demand, there was a larger share of it being drawn from side B, leading to an increase in the hybridization degree. Unlike the unloaded test, for 30% side A throttle the system reached 40% hybridization, which is well above previous results.

10 A

For the loaded 10 A tests, the data gathered is plotted in Figure 5.6.

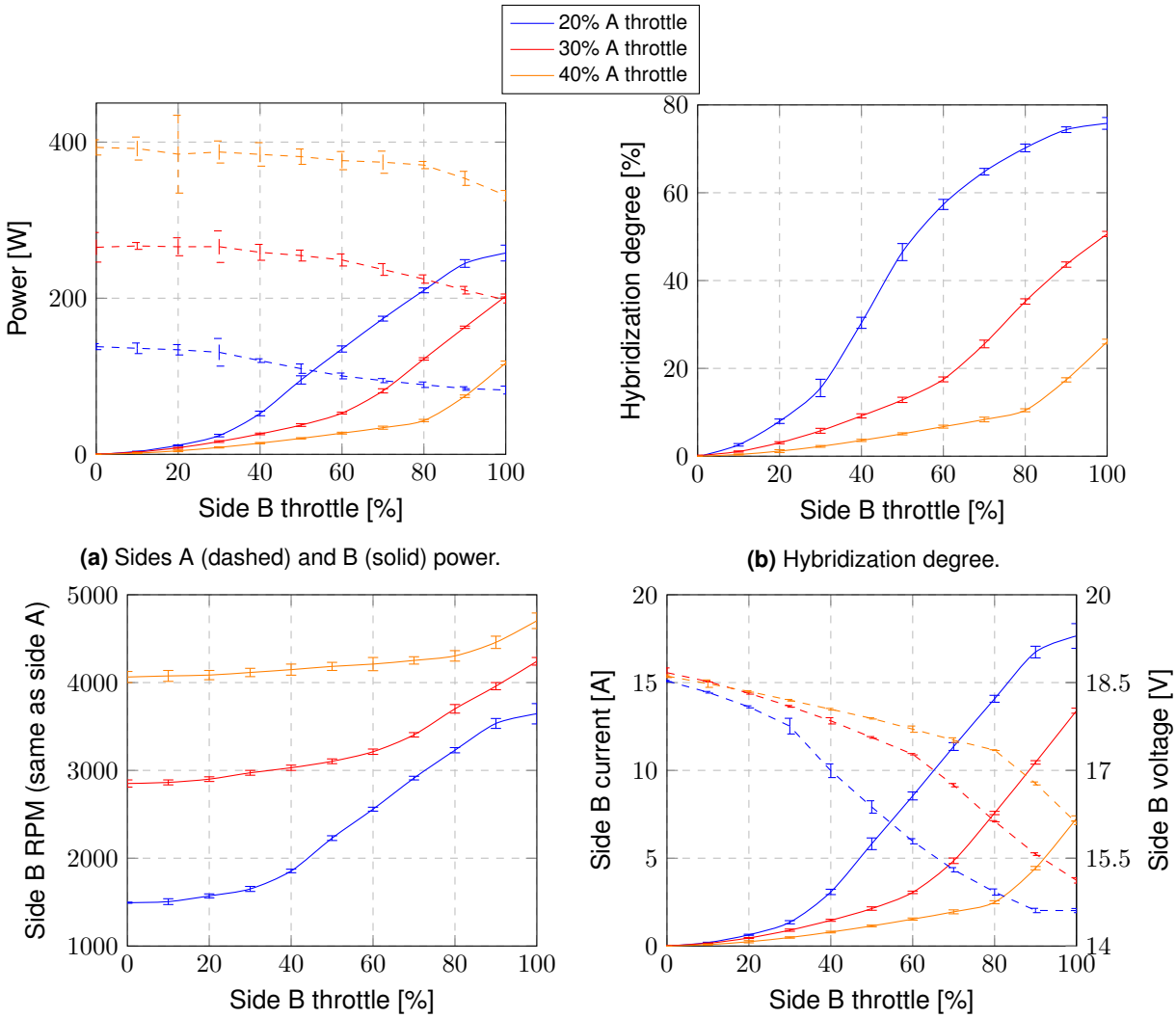

(a) Sides A (dashed) and B (solid) power.

(b) Hybridization degree.

(c) RPM.

(d) Side B current (solid) and voltage (dashed).

Figure 5.6: Test bench variables for the loaded 10 A hybrid tests.

In this data, the same trends observed before are present, with an even greater difference when compared to the unloaded tests. The power and current consumed were greater, while the voltage drop was bigger and the rotational speed smaller. The hybridization degree observed in these tests reached the largest values observed, with nearly 76% for the 20% A throttle test.

For these tests, the power consumption can be analyzed once again, this time with the electrical output of the system, as it is loaded. With this purpose, Figure 5.7 is presented.

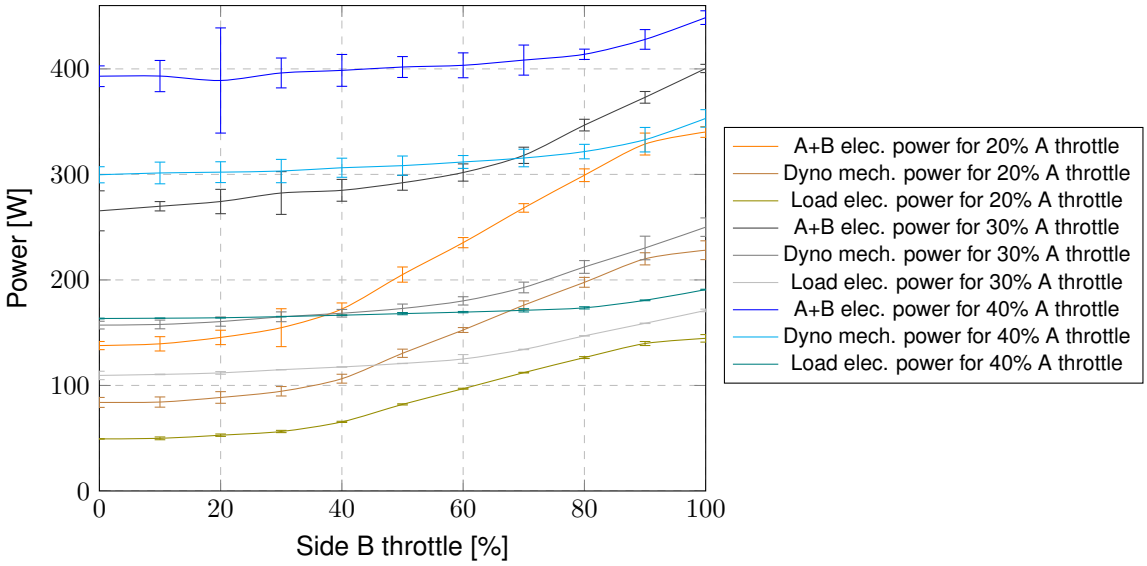

Figure 5.7: Power for the loaded 10 A hybrid tests.

Once again, it can be seen that the mechanical power consumed by the dyno follows the same trend as the electrical power supplied to the system, with a gap in-between them. In these loaded tests, this gap is about 50 to 100 W, which is slightly smaller than the ones observed for the unloaded tests. This can point to the lower friction felt by the system, given its lower rotational speed. In these tests, unlike the unloaded tests, part of the dyno power is converted to electricity, which can be seen in the plot as well. It is relevant to notice that, despite showing the same behaviour as the dyno mechanical power, increasing with the side B throttle, it is significantly lower. In fact, the highest conversion efficiency between mechanical power and electrical power is found for the 30% A throttle tests, at about 70%, while the other two tests show a worse performance, with values as low as 54%. The overall efficiency of the whole system is closer to 40%. While this value can be considered quite low, it is worth remembering that, in a real propulsion system this last conversion step would not exist, as the power would be used mechanically by a propeller.

5.4 Application to an UAV

As with any propulsion system, the final goal is aircraft integration. In the case of this project, the objects of interest are UAVs, so it is important to evaluate how the fuel cell analyzed would behave in such an application.

The first thing to consider is for which aircraft this propulsion system would be designed for, and what are its requirements. As a reference, the *Mini-E* aircraft, developed at CfAR, will be used, and whose propulsion system sizing was done by Sara Pedro [93]. This UAV is a small fully-electric aircraft, used for testing as part of the development of a larger UAV for magnetic anomaly detection. Some relevant values found during the sizing process, for different propulsion configurations, are compiled in Table 5.1.

Immediately, incompatibilities between the fuel cell stack at hand and the UAV requirements can be spotted. To begin with, the setup used is far too heavy to be used in flight. The entire HP 600 fuel cell system has a mass of about 42 kg, with just the stack weighing 9.8 kg. The hydrogen storage solution used is also not appropriate for onboard storage: it has a mass of over 65 kg, the vast majority of which coming from the cylinder itself, and not the hydrogen stored inside (which accounts for less than 1% of the total mass).

Table 5.1: *Mini-E* specifications.

Parameter		Value
Maximum take-off mass (MTOM)		7 kg
Minimum thrust to weight ratio (T/W)		1.3
Battery type		6S (22.2 V)
Endurance	**cruise**	20 min
	max. throttle	10 s
	take-off & landing	90 s
Energy backup		20%
Energy requirements		70∼80 Wh
Power requirements	**cruise**	90∼115 W
	dash	390∼480 W
	VTOL	1000∼1100 W
Chosen conf. installed power		2490 W
Battery energy density		170.33 Wh/kg
Propulsion system mass		1.2∼1.7 kg
Battery mass		∼0.45 kg

Besides this, the electrical capabilities of the stack are also not in line with what is necessary for this application. While the power it can provide is enough for both the cruise and dash requirements, being a vertical take-off and landing (VTOL) aircraft, the power consumption in those flight segments is well above what the stack generates. Moreover, the stack's voltage is too low for the reference value used in this sizing.

However, while this indicates that the setup tested is not suitable for an UAV integration, this should not be taken as an impossibility to utilize this type of technology as the basis of a propulsion system. Simply, the fuel cell system available was never designed for such an application. The stack and surrounding system were made for educational purposes, to be used in a classroom or on a lab setting, so its components are oversized when compared to what could be designed for airborne operations. It is also worth mentioning that the stack itself is quite old, reflecting the state of FC technology in the early 2000s. Much progress has been made since, allowing for better alternatives to be found on the market. The hydrogen storage choice was also made based on the availability of the compressed gas cylinder, and only with ground testing in mind. It was obvious from the beginning that such a heavy metal cylinder was not what would be used in an eventual UAV integration.

With this in mind, it is important to investigate some of the options available in the market, that can satisfy the propulsion requirements of the UAV in question. A few different suitable options were identified, including: Doosan's Powerpack Module DM15/DP15, Honeywell's 600U Hydrogen Fuel Cell, Intelligent Energy's IE-SOAR 800W Second Generation, and H3 Dynamics' Aerostak A-250 and A-500. Some important characteristics publicly available from these different FCs are summarized in Table 5.2, and their pictures are in Figure 5.8.

Table 5.2: Specifications for different commercially available fuel cells [94][95][96][97].

Fuel Cell	Rated Power [W]	Peak Power [W]	Output Voltage [V]	Weight [kg]
DM15/DP15	1250	9000	-	2.9
600U	600	-	12-33.6	1.8
IE-SOAR 800	800	2400	24∼28	1.45
Aerostak 250	250	300	24.5∼35.2	0.72
Aerostak 500	500	600	28∼42.8	1.58

Out of these options, only one can accommodate, in continuous power, all the flight segments of the UAV. However, it is important to remember that a FC integration in a propulsion system is likely

(a) DM15/DP15 [94].

(b) 600U [95].

(c) IE-SOAR 800 [96].

(d) Aerostak 250 [97].

(e) Aerostak 500 [97].

Figure 5.8: Different fuel cells analyzed.

going to include at least a battery, which can make up for the extra needed power during take-off and climb. In fact, some of the FCs presented here already include the option to be purchased with a battery included in a hybrid configuration. On the other hand, they can all more than satisfy the cruise power requirements, which could allow for any battery part of the propulsion system to be recharged by the fuel cell during this flight phase. With the exception of the Aerostak 250, they all can supply the full amount of power necessary during dash operation as well.

Given the mission requirements, that include only about 10 seconds of dash flight, a FC stack like the Aerostak 250 might still be considered as the solution for the given UAV. The extra power needed during this phase could be supplied by a LiPo battery, that would already be necessary anyway, to complement the larger power requirements during take-off. This stack's reduced mass, by far the lowest of the ones considered, makes it a very attractive option given the mass constraints of such a small aircraft. Otherwise, the next lightest stack is the IE-SOAR 800, with about double the mass, but more than three times the power output. This stack could fully cover the power demand during dash, and could supply the majority of power for VTOL, requiring less backup battery capacity. Still, with either of these options, it is already obvious that the propulsion system mass will suffer a significant increase with the inclusion of a FC, and the respective hydrogen storage and complimentary batteries necessary.

To estimate the battery mass necessary in a hybrid configuration with these different FC stacks, the same energy consumption estimations made in Sara Pedro's work can be used. In it, it shows that about 30% of the batteries was to be consumed during take-off. If the hybrid configuration chosen used solely the batteries during this phase, and then relied on the fuel cell for the remaining flight, the initial estimation of 450 g of battery could be reduced to about 135 g. If the Aerostak 250 was being used, little further reduction in battery mass could be achieved, as during take-off the stack could help with, at most, a quarter of the power requirements, while battery power would also be needed for dash mode. With a

different stack, such as the IE-SOAR 800, much more power could come from the fuel cell, with mass gains on the battery side. Given that this stack could produce as much as 80% of the take-off power demand, it its not unreasonable to think that less than half of the 135 g of battery could be used, without compromising the UAV operation. However, when considering the total mass of both the batteries and FC, the Aerostak 250 still would have a lower value, with around 0.85 kg compared to around 1.5 kg.

Despite these first values, the largest mass penalty to the propulsion system will come from the hydrogen storage. As already discussed in Chapter 2, onboard storage poses one of the main challenges to hydrogen usage, and can generally come in either of three different options: as a compressed gas, as a liquid, or chemically bounded in hydrides. Out of these, the simplest one is the compressed gas cylinder, the same option used in the experiments previously presented. With this alternative, only a pressure regulator is necessary to deliver the gas from its storage to the FC, unlike hydrides that require some chemical reaction to obtain the hydrogen stored. Moreover, no additional thermal management systems are needed, like it would be with liquid hydrogen.

Out of different cylinder providers, by far the most suitable alternatives, given their light weight, were the series A and F cylinder, by H3 Dynamics, one of the manufacturers of the FCs analyzed. The three hydrogen cylinders weighing less than 2 kg have their specifications shown in Table 5.3.

Table 5.3: Specifications for H3 Dynamics' compressed hydrogen cylinders [98].

Cylinder	F2	F3	A5
Capacity [L]	2	3	5
Weight [kg]	1.46	1.75	1.65
Max. Pressure [bar]	300	300	350
Hydrogen Mass [g]	42	63	120
Specific Energy [kJ/kg]	3173	4008	8725
Specific Energy [kWh/kg]	0.88	1.11	2.42

Given the higher storage pressure of the series A cylinders, and the higher capacity of its smallest size, the A5 cylinder can store about three time as much hydrogen as the F2, and nearly double the F3, with a mass value that falls in-between these two alternatives. Thus, it has a much higher specific energy than both, about 2.7 times greater than the lightest F2 cylinder. If the desired integration can accommodate the extra 200 g of the A5 cylinder, then this appears to be the best alternative. Still, even the F2 cylinder has a much higher energy density than what was considered for batteries (170.33 Wh/kg).

Finally, to estimate the total mass of the propulsion system, the pressure regulator also has to be counted. For the same manufacturer, this value is 250 g, with accessories [98]. Therefore, it can be estimated that the electrical supply system will have between 2.56 kg, using the lightest FC stack and hydrogen tank, and 3.4 kg, with the IE-SOAR stack and the A5 cylinder. This means there is an overall mass increase of between 2 and 3 kg, when compared to the initial estimation of battery mass of around 0.45 kg.

The other penalty to the system, that cannot be ignored, comes with the increase in volume dedicated to this system. Once again, storage presents itself as the hardest element to accommodate. The smallest cylinder has a length of 371 mm and 114 mm of diameter, while the larger A5 measures 395 mm with 152 mm of diameter. The stacks are considerably smaller, with the IE-SOAR 800 being 210x105x105 mm, and the Aerostak 250 being only 122x123x112 mm. These dimensions, as well as the added mass, might be difficult to currently integrate in the *Mini-E* aircraft. However, following iterations of this UAV, with a larger dimension, such as the one analyzed in [23], with a 25 kg MTOM and a 3 m wingspan, may be better able to accommodate such a system.

The final aspect to consider is the main benefit that a FC would bring to the propulsion system for this aircraft, which is extended endurance. As a first approximation, an estimated endurance will be

calculated considering only the cruise flight phase, as the 10 seconds of dash consume much less total energy than this phase, and the take-off would be accomplished together with the installed battery. Like before, some energy backup will be considered. Given higher total energy stored in the hydrogen cylinder, and the presence of a backup battery which can be recharged during flight and used in an emergency, a lower value of only 5% (of the total hydrogen stored) will be used.

Firstly, for the Aerostak 250 the maximum hydrogen consumption is 2.8 L/min. Being unclear what temperature and pressure conditions are considered in this measurement, the most pessimistic scenario was assumed, giving a maximum consumption of 0.252 g/min. Calculating how long 95% of the hydrogen stored in each cylinder would last in this case returns 158 min (2.6 h) for the F2 cylinder, and 452 min (7.5 h) for the A5. This simple analysis has the FC stack consuming its maximum value throughout the entire cruise flight. As was observed during experiments in this project, or as corroborated by data from other manufacturers (such as Honeywell [95]), this maximum consumption will occur for the maximum power output of the stack. While this may occur for some periods of time, for example during onboard recharging of the battery, the power demand during most of cruise is much lower, below half the maximum output of the FC. Thus, it is reasonable to assume that the average hydrogen consumption during this phase could be lower, further extending the endurance time of the aircraft.

For the IE-SOAR 800 stack, the hydrogen consumption data is not readily available, but the manufacturer provides some integration example values for UAV endurance. One example has a 5 L cylinder, and a total system mass of 3.9 kg, which is in line with the value reached here with the A5 cylinder. This has a flight time of 4.9 hours. The smallest cylinder the manufacturer mentions has 3 L, with a higher system mass of 4 kg, for a flight time of 2.6 hours. The F2 cylinder could give a lighter system, but also has a smaller storage capacity than this example. However, the main difference between the scenarios provided by the manufacturer and the *Mini-E* is the power considered: these estimations were based on an integration at 400 W, while the cruise phase of this UAV consumes around a quarter of that.

Nevertheless, these rough estimations can indicate the scale at which an UAV endurance can be extended by using a fuel cell as part of its propulsion system. In the battery-only configuration, the minimum endurance of 20 min could only be extended to about 40 min when converting every mass gain of its most advantageous configuration in extra battery mass. In stark contrast, the lowest estimated endurance for a FC configuration was above two and a half hours, and with an additional 200 g the system could almost triple its endurance. This estimation already highlights the potential of FC to increase the endurance (and range) of UAVs when compared to a battery-only configuration.

The analysis presented constitutes a preliminary study on the use of fuel cells in a small UAV. A more detailed analysis will need to be performed, to better quantify the different aspects of the planned propulsion system, as well as how its physical integration into the aircraft can be accomplished. One final aspect that was not mentioned here is cost, as this information is not publicly available, and a quote would have to be requested from the manufacturers. While it can be expected that the system will have a higher price tag than if it used only batteries, it is not clear what is the difference in price between the different manufacturers. Naturally, this variable might have some influence when finally choosing the stack to be used.

Chapter 6

Conclusion

This chapter presents the conclusions drawn from the current research. It summarizes the achievements in this experimental research, its main results, and how the objectives were achieved. It also proposes recommendations for future work.

6.1 Achievements

The main goal of this research project was to study the feasibility of using fuel cell technology for electrification of UAV propulsion. In particular, the goal was to evaluate the performance of a fuel cell stack as a power source in a hybrid propulsion system.

In order to fulfill these goals, several important steps were taken. This began with getting acquainted with the different components that would be used during the experimental tests. It was necessary to study some of the theoretical background for the technology used, and the necessary precautions. This included reviewing all safety documents and operation manuals for the critical components. Only then, after ensuring the safety of all those involved, it was finally possible to start testing the fuel cell system.

The first tests performed concerned only the fuel cell system behaviour. Several different aspects of its performance were studied. First, as some of the components had never been used before, and as the FC system itself had a considerable lifespan as well, some simple safety tests were run, to verify that the different components functioned correctly. Then, data could begin to be gathered.

The first set of data collected concerned the current and voltage of the stack, over its entire operating range. It proved that, for the three tests performed, the stack showed a consistent and predictable behaviour. This predictability is extremely important, as it allowed for its benchmark current-voltage and current-power curves to be determined, which can be used to estimate the operating point for the stack under different conditions. Based on the same tests, the efficiency of the FC stack could be calculated, showing how much of the hydrogen energy was being converted to electricity. Given the increase in losses with the current, the efficiency dropped from over 60% for the lower loads, to about 40% for the highest current drawn.

To fully test the capabilities of the FC system, the regulated operating mode of the system was also tested. This offered a better insight into how the internal controller of the system worked, in what can be essentially classified as a semi-active hybrid configuration. It was observed that this mode can offer some advantages when compared to the stack on its own. Particularly, the output voltage showed very little variation, due to the battery present, without compromising the current output, which came essentially from the fuel cell, as before. However, for the same current, the power output was smaller (given the lower voltage), though for the highest load the maximum power output was the same, about

500 W, given the significant voltage reduction observed in the FC's polarization curve.

The fuel cell system was connected to several different electric motors, to observe its response, and compare it to conventional LiPo batteries. The data collected showed that the thrust generated by the motors was closely related to the voltage being supplied. This means that the fuel cell proved more powerful than a 4S battery for low throttle, while being less powerful for higher settings, while the regulated mode was in-between a 3S and a 4S battery. While these tests were successful, and once again showed the FC stack behaving in a predictable way, its relatively low voltage output limited the choice of EMs that were adequate for such tests. These, in turn, only reached a maximum thrust of about 25 N with the FC as a power source, for the AXI 2826 motor.

As part of these propulsion tests, the response time of the fuel cell was analyzed. For the throttle demand used (of 50%), negligible difference was observed between a 4S battery and the stack. However, it was noted that, for higher power demands, there could be a bigger delay when using the FC. Still, given the small difference, and the possibility for a fuel cell to be easily implemented together with a battery, this does not seem to be a significant concern when considering this technology for anUAV propulsion system.

This first results collected show some promise for a FC-powered propulsion system, for small UAV. It confirmed that a fuel cell stack can correctly power an electrical motor and propeller, such as the ones found on small UAV. When combined with a battery, it even demonstrated that the system can have the same behaviour as one in terms of response time, for example, while maintaining the state of charge by drawing the necessary current from the stack. However, it was noted that the fuel cell in question could not be directly equipped in an aircraft. The stack itself, along with the setup it was on, and the method used to store the hydrogen gas, were all very heavy, and much more so than the thrust obtained in the propulsion tests. Still, this does not mean that a different setup could not achieve flight-readiness, as it had been previously discovered in the literature review, chapter 2.

Having successfully concluded these experiments, it was possible to test a parallel hybrid architecture, composed of two electrical motors. One was powered using the fuel cell stack, while the other was connected to two 6S batteries. This experiment allowed for a better understanding of how such a configuration functions, and how the power from two different sources can be mechanically combined. While a configuration such as the ones discussed in section 2.2.2 might be more likely used if only electrical power sources are being combined, this parallel configuration is relevant as it might be used with an internal combustion engine, for example.

With that being said, although the tests conducted were successful, the FC's voltage capabilities are undersized for the motor to which its output was connected. This limitation did not allow to draw the total possible power from the stack. Nevertheless, as shown by the individual power evolution of both sides throughout the throttle sweeps, the FC was able to significantly reduce the power drawn on the side A, without changing the system loading or the side A settings.

This dynamic power splitting shows promise in lessening fuel consumption in a possible hydrogen–ICE configuration. In such a configuration, the fuel cell can provide power to the electric components, similarly to a battery, but with the added benefit of longer endurance, given the higher energy density of hydrogen. In a fully electric hybrid system, this fact means a FC can serve as the main energy source for the system, while being complimented by batteries, or other electrical components, which were not yet studied as part of this project.

Finally, the possibility of aircraft integration was briefly analyzed, to better understand what benefits and challenges exist when applying this technology to small UAVs. It was found that, while the FC stack used in the tests was not designed for such an application, and therefore not suitable for that, it already pointed at the main issues in doing so. While alternative stacks and storage solutions were found to be commercially available, the mass added to the system was never less than 2 kg, with a sig-

nificant increase in the volume dedicated to energy storage as well. Even so, very significant endurance gains were estimated, which indicate that such a technology is worth pursuing, for the promise of long endurance electric aircraft.

6.2 Future Work

All the work presented in this document was, as mentioned previously, part of a larger hybrid propulsion research effort being conducted at CfAR for the past few years. In particular, the experiments described here were the first ones conducted at the centre using a fuel cell, and using hydrogen as a fuel in general. These first tests, and the methodology developed for them, allow the possibility of further testing, using the available fuel cell system or after acquiring a new FC stack.

With the current setup, there are still some tests that can be performed, to deepen our understanding of how a fuel cell hybrid system can work. With that goal, it would be convenient to design a hybrid test bench better sized for the fuel cell capabilities. The available test bench, used in this project, includes EMs suitable for much higher voltages than the ones supplied by the FC. Given this fact, a system accommodating smaller motors, similar to the ones used in the propulsion tests of chapter 4.2, could provide better results, with a more balanced power split for a wider range of throttle settings. Particularly, the AXI 2826/10 motor already acquired allows for the full utilization of the fuel cell operating range, with a more adequate voltage rating than the AXI 4130/20 used in the test bench.

Another configuration of interest, that could not yet be studied during this project, is a FC-ICE hybrid system. The hybrid test bench utilized was adapted to include a two-stroke internal combustion engine, and some tests were performed, as can be read in [84]. However, due to some issues associated with the ICE, the tests on the battery-ICE parallel system could not be fully completed, and no experiments were made using the FC stack. Some of the challenges encountered were the high vibration of the engine, the difficulty in starting the engine, and the torque spikes which were too great for the electromagnetic clutch to withstand without slipping. Efforts to address these issues have began, for example, by procuring a new clutch for the test bench.

To fully test hybrid configurations, there was also the desire to analyze a series configuration. For such, some changes would need to be made to the test bench, to accommodate for the new design. The ICE should me mechanically coupled only to a generator, like the only used in the dyno section of the test bench. Then, its electrical output could be connected to an EM, which would power the propeller. In this connection, there should be one or more batteries, to store the power, and at a latter stage the hydrogen fuel cell can be included as well, to generate additional electricity for the propulsion system.

Both these configurations require further study, when it comes to the most adequate control strategies to be used. In this front, some initial open-loop iterations were developed for the parallel configuration [14], but further research effort is still necessary to reach state of the art solutions.

On the other hand, given the ultimate goal of flying an aircraft with a propulsion system derived from this hybrid project, it might be beneficial to acquire a new and more modern fuel cell. This should be procured given the specific requirements of a UAV, when it comes to both power output and weight.

In this case, if a different FC is obtained, the characterization process should be repeated, following the same guidelines that were developed during this project. Some changes might need to be made to the test procedures, to adapt them to a new stack. Some more tests might be possible to be performed, to better determine the full behaviour of the stack. These can include pressure, temperature, and humidification level tests, or fuel and oxidant stoichiometry tests. Being an educational model, the system currently available did not allow for the user variation of these variables, which limited the tests that could be conducted, but in a new system these factors should be studied.

In a new FC it may also be necessary to assemble the peripheral systems, that in the case of the HP 600 fuel cell system were already included. These can include a hydrogen delivery system or a thermal management system.

A new system should also include a better method for data collection. In this project, all variables measured by the FC system's sensors had to be recorded manually by the test operator. When compared to the capabilities of LabVIEW, explored in the data collection for the hybrid test bench, this method was less accurate and much more time consuming. For the future, it is recommended, if possible, to develop a similar computational resource to measure data, visualize it in real time, and log it, in line with what was achieved by the test bench's LabVIEW VI.

Finally, after all desired tests are completed on the ground, it will be necessary to adapt the different components used for aircraft integration, in a feasible propulsion system for a UAV. Since the system designed on the test bench has aircraft integration as its final goal, when this stage is reached the transition should be relatively straight forward.

Bibliography

[1] ICAO. *Presentation of 2019 Air Transport Statistical Results*. https://www.icao.int/annual-report-2019/Documents/ARC_2019_Air%20Transport%20Statistics.pdf. Last accessed on 11.05.2022. 2020.

[2] Airbus. *Airbus Global Market Forecast 2021-2040*. https://www.airbus.com/sites/g/files/jlcbta136/files/2021-11/Airbus-Global-Market-Forecast-2021-2040.pdf. Last accessed on 11.05.2022. 2021.

[3] J. E. Penner et al. *IPCC Special Report Aviation and the Global Atmosphere - Summary for Policymakers*. Cambridge University Press, 1999.

[4] R. Sims et al. "Climate Change 2014: Mitigation of Climate Change. Contribution of Working Group III to the Fifth Assessment Report of the Intergovernmental Panel on Climate Change". In: ed. by O. Edenhofer et al. Cambridge, United Kingdom and New York, NY, USA: Cambridge University Press, 2014. Chap. Transport.

[5] J. E. Penner et al. *Aviation and the Global Atmosphere*. Cambridge, United Kingdom and New York, NY, USA: Cambridge University Press, 1999.

[6] S. H. L. Yim et al. "Global, regional and local health impacts of civil aviation emissions". In: *Environmental Research Letters* 10.3 (2015), p. 034001. DOI: 10.1088/1748-9326/10/3/034001.

[7] The European Parliament and The Council of the European Union. "Regulation (EU) 2017/2392 of the European Parliament and of the Council of 13 December 2017 amending Directive 2003/87/EC to continue current limitations of scope for aviation activities and to prepare to implement a global market-based measure from 2021". In: *Official Journal of the European Union* (Dec. 2017). Last accessed on 13.05.2022.

[8] Croatia and the European Commission on behalf of the European Union and its Member States. *Long-term low greenhouse gas emission development strategy of the European Union and its Member States*. https://unfccc.int/sites/default/files/resource/HR-03-06-2020%20EU%20Submission%20on%20Long%20term%20strategy.pdf. Last accessed on 13.05.2022. Mar. 2020.

[9] IATA. *IATA Economic Briefing Airline Fuel and Labour Cost Share*. https://www.iata.org/en/iata-repository/publications/economic-reports/airline-fuel-labourcosts/. Last accessed on 11.05.2022. Feb. 2010.

[10] U. S. Energy Information Administration EIA. *Independent Statistics & Analysis Short-Term Energy Outlook*. https://www.eia.gov/outlooks/steo/pdf/steo_full.pdf. Last accessed on 12.05.2022. May 2022.

[11] H. Aliaga Aguilar and J. Cubas Cano. "UAV influence in the emissions of airborne cargo transportation". In: *8th European Conference for Aeronautics and Space Sciences*. Madrid, Spain, July 2019. DOI: 10.13009/EUCASS2019-306.

[12] C. C. Chan and K. T. Chau. *Modern electric vehicle technology*. Oxford, United Kingdom: Oxford University Press, 2001.

[13] Y. Demirel. *Energy: Production, Conversion, Storage, Conservation, and Coupling*. Springer Nature Switzerland AG, 3rd edition, 2021. DOI: 10.1007/978-1-4471-2372-9.

[14] L. M. G. Machado. *Design and Development of a Hybrid Electric Propulsion System for Unmanned Aerial Vehicles*. Master's thesis, Instituto Superior Técnico. May 2019.

[15] M. Moran et al. *Fundamentals of Engineering Thermodynamics*. John Wiley & Sons, Inc., eighth edition, 2014.

[16] Z.F. Pan, L. An, and C.Y. Wen. "Recent advances in fuel cells based propulsion systems for unmanned aerial vehicles". In: *Applied Energy* 240 (2019), pp. 473–485. DOI: 10.1016/j.apenergy.2019.02.079.

[17] E. H. Wakefield. *History of the Electric Automobile*. Society of Automotive Engineers, 1998.

[18] T. A. Rotramel. *Optimization of Hybrid-Electric Propulsion Systems for Small Remotely-Piloted Aircraft*. Master's thesis, Air Force Institute of Technology. Nov. 2011.

[19] Diamond Aircraft Inudstries GmbH. *Diamond Aircraft 1st Flight Multi-engine Hybrid Electric Aircraft*. https://www.diamondaircraft.com/en/about-diamond/newsroom/news/article/diamond-aircraft-1st-flight-multi-engine-hybrid-electric-aircraft/. Last accessed on 22.09.2022. Nov. 2018.

[20] National Reseach Council Canada. *Battling the headwinds of climate change with electric aviation*. https://nrc.canada.ca/en/stories/battling-headwinds-climate-change-electric-aviation. Last accessed on 09.10.2022. May 2021.

[21] Skies Magazine, NRC Press Release. *NRC supports the fight against climate change with hybrid-electric Cessna*. https://skiesmag.com/press-releases/nrc-flies-hybrid-electric-cessna-sporting-one-of-the-worlds-highest-voltage-electric-propulsion-systems-to-date/. Last accessed on 09.10.2022. Apr. 2022.

[22] J. M. T. Matlock. *Evaluation of Hybrid-Electric Propulsion Systems for Unmanned Aerial Vehicles*. Marter's thesis, Department of Mechanical Engineering, University of Victoria. 2019.

[23] P. M. M. Fernandes. *Development, Computational and Experimental Characterization of a Canard Aircraft Configuration*. Marter's thesis, Instituto Superior Técnico. Nov. 2021.

[24] J. Schömann. *Hybrid-Electric Propulsion Systems for Small Unmanned Aircraft*. PhD Thesis, Technische Unisersität München. July 2014.

[25] C. Kim et al. "Fuel Economy Optimization for Parallel Hybrid Vehicles with CVT". In: *SAE Technical Paper Series* (1999). DOI: 10.4271/1999-01-1148.

[26] H. D. Kim, A. T. Perry, and P. J. Ansell. "A Review of Distributed Electric Propulsion Concepts for Air Vehicle Technology". In: *2018 AIAA/IEEE Electric Aircraft Technologies Symposium (EATS)*. Cincinnati, Ohio, USA, July 2018. DOI: 10.2514/6.2018-4998.

[27] F. G. Harmon, A. A. Frank, and S. S. Joshi. "Application of a CMAC neural network to the control of a parallel hybrid-electric propulsion system for a small unmanned aerial vehicle". In: *2005 IEEE International Joint Conference on Neural Networks* 1 (2005), 355–360 vol. 1. DOI: 10.1109/IJCNN.2005.1555856.

[28] C. J. Brace et al. “An operating point optimizer for the design and calibration of an integrated diesel/continuously variable transmission powertrain”. In: *Proceedings of the Institution of Mechanical Engineers, Part D: Journal of Automobile Engineering* 213 (1999), pp. 215–226. DOI: 10.1243/0954407991526810.

[29] D. Cecere, E. Giacomazzi, and A. Ingenito. “A review on hydrogen industrial aerospace applications”. In: *International Journal of Hydrogen Energy* 39.20 (2014), pp. 10731–10747. DOI: 10.1016/j.ijhydene.2014.04.126.

[30] National Aeronautics and Space Administration. *Space Applications of Hydrogen and Fuel Cells*. https://www.nasa.gov/content/space-applications-of-hydrogen-and-fuel-cells. Last accessed on 19.05.2022.

[31] K. A. Burke. *Fuel Cells For Space Science Applications*. https://ntrs.nasa.gov/api/citations/20040010319/downloads/20040010319.pdf. Last accessed on 19.05.2022. Nov. 2003.

[32] A. Baroutaji et al. “Comprehensive investigation on hydrogen and fuel cell technology in the aviation and aerospace sectors”. In: *Renewable and Sustainable Energy Reviews* 106 (2019), pp. 31–40. DOI: 10.1016/j.rser.2019.02.022.

[33] Airbus Deutschland GmbH. *Liquid Hydrogen Fuelled Aircraft – System Analysis FINAL TECHNICAL REPORT*. https://www.fzt.haw-hamburg.de/pers/Scholz/dglr/hh/text_2004_02_26_Cryoplane.pdf. Last accessed on 19.05.2022. 2003.

[34] A. Contreras et al. “Hydrogen as aviation fuel: A comparison with hydrocarbon fuels”. In: *International Journal of Hydrogen Energy* 22.10 (1997), pp. 1053–1060. DOI: 10.1016/S0360-3199(97)00008-6.

[35] M. G. Sürer and H. T. Arat. “State of art of hydrogen usage as a fuel on aviation”. In: *European Mechanical Science* 2.1 (2018), pp. 20–30. DOI: 10.26701/ems.364286.

[36] O. Bičáková and P. Straka. “Production of hydrogen from renewable resources and its effectiveness”. In: *International Journal of Hydrogen Energy* 37.16 (2012), pp. 11563–11578. DOI: 10.1016/j.ijhydene.2012.05.047.

[37] N. Belmonte et al. “Fuel cell powered octocopter for inspection of mobile cranes: Design, cost analysis and environmental impacts”. In: *Applied Energy* 215 (2018), pp. 556–565. DOI: 10.1016/j.apenergy.2018.02.072.

[38] B. Wang et al. “Current technologies and challenges of applying fuel cell hybrid propulsion systems in unmanned aerial vehicles”. In: *Progress in Aerospace Sciences* 116 (2020), p. 100620. DOI: 10.1016/j.paerosci.2020.100620.

[39] Ó. González-Espasandín et al. “Direct methanol fuel cell (DMFC) and H2 proton exchange membrane fuel (PEMFC/H2) cell performance under atmospheric flight conditions of Unmanned Aerial Vehicles”. In: *Renewable Energy* 130 (2019), pp. 762–773. DOI: 10.1016/j.renene.2018.06.105.

[40] X. Cheng et al. “A review of PEM hydrogen fuel cell contamination: Impacts, mechanisms, and mitigation”. In: *Journal of Power Sources* 165.2 (2007). IBA – HBC 2006, pp. 739–756. DOI: 10.1016/j.jpowsour.2006.12.012.

[41] A. Gong and D. Verstraete. “Fuel cell propulsion in small fixed-wing unmanned aerial vehicles: Current status and research needs”. In: *International Journal of Hydrogen Energy* 42.33 (2017), pp. 21311–21333. DOI: 10.1016/j.ijhydene.2017.06.148.

[42] A.B. Bose and X. Zhu. “Design of stable and durable polymer electrolyte membrane fuel cells by embedding hydrophobic cage-structured material in cell components”. In: *Fuel* 235 (2019), pp. 954–961. DOI: 10.1016/j.fuel.2018.08.051.

[43] H. Barthelemy, M. Weber, and F. Barbier. “Hydrogen storage: Recent improvements and industrial perspectives”. In: *International Journal of Hydrogen Energy* 42.11 (2016). Special issue on The 6th International Conference on Hydrogen Safety (ICHS 2015), 19-21 October 2015, Yokohama, Japan, pp. 7254–7262. DOI: 10.1016/j.ijhydene.2016.03.178.

[44] A. M. Abdalla et al. “Nanomaterials for solid oxide fuel cells: A review”. In: *Renewable and Sustainable Energy Reviews* 82 (2018), pp. 353–368. DOI: 10.1016/j.rser.2017.09.046.

[45] Z. Ji et al. “Thermodynamic analysis of a solid oxide fuel cell jet hybrid engine for long-endurance unmanned air vehicles”. In: *Energy Conversion and Management* 183 (2019), pp. 50–64. DOI: 10.1016/j.enconman.2018.12.076.

[46] Z. Ji et al. “Comparative performance analysis of solid oxide fuel cell turbine-less jet engines for electric propulsion airplanes: Application of alternative fuel”. In: *Aerospace Science and Technology* 93 (2019), p. 105286. DOI: 10.1016/j.ast.2019.07.019.

[47] G. Genç and S. Sarikoç. “Energy and exergy analysis of a solid-oxide fuel cell power generation system for an aerial vehicle (ISSA- 2015–139)”. In: *International Journal of Green Energy* 15.3 (2018), pp. 151–160. DOI: 10.1080/15435075.2017.1324789.

[48] M.D. Fernandes et al. “SOFC-APU systems for aircraft: A review”. In: *International Journal of Hydrogen Energy* 43.33 (2018), pp. 16311–16333. DOI: 10.1016/j.ijhydene.2018.07.004.

[49] M. Zago et al. “On the actual cathode mixed potential in direct methanol fuel cells”. In: *Journal of Power Sources* 325 (2016), pp. 714–722. DOI: 10.1016/j.jpowsour.2016.06.093.

[50] S. H. Seo and C. S. Lee. “A study on the overall efficiency of direct methanol fuel cell by methanol crossover current”. In: *Applied Energy* 87.8 (2010), pp. 2597–2604. DOI: 10.1016/j.apenergy.2010.01.018.

[51] H. Kim, T. H. Oh, and S. Kwon. “Simple catalyst bed sizing of a NaBH4 hydrogen generator with fast startup for small unmanned aerial vehicles”. In: *International Journal of Hydrogen Energy* 41.2 (2016), pp. 1018–1026. DOI: 10.1016/j.ijhydene.2015.11.134.

[52] D. Verstraete et al. “Experimental investigation of the role of the battery in the AeroStack hybrid, fuel-cell-based propulsion system for small unmanned aircraft systems”. In: *International Journal of Hydrogen Energy* 40.3 (2015), pp. 1598–1606. DOI: 10.1016/j.ijhydene.2014.11.043.

[53] S. Njoya Motapon, L.-A. Dessaint, and K. Al-Haddad. “A Comparative Study of Energy Management Schemes for a Fuel-Cell Hybrid Emergency Power System of More-Electric Aircraft”. In: *IEEE Transactions on Industrial Electronics* 61.3 (2014), pp. 1320–1334. DOI: 10.1109/TIE.2013.2257152.

[54] S. Huang et al. “Challenges and opportunities for supercapacitors”. In: *APL Materials* 7.10 (2019), p. 100901. DOI: 10.1063/1.5116146.

[55] M. Gadalla and S. Zafar. “Analysis of a hydrogen fuel cell-PV power system for small UAV”. In: *International Journal of Hydrogen Energy* 41.15 (2016), pp. 6422–6432. DOI: 10.1016/j.ijhydene.2016.02.129.

[56] P. Rajendran and H. Smith. “Implications of longitude and latitude on the size of solar-powered UAV”. In: *Energy Conversion and Management* 98 (2015), pp. 107–114. DOI: 10.1016/j.enconman.2015.03.110.

[57] F. H. Alharbi and S. Kais. “Theoretical limits of photovoltaics efficiency and possible improvements by intuitive approaches learned from photosynthesis and quantum coherence”. In: *Renewable and Sustainable Energy Reviews* 43 (2015), pp. 1073–1089. DOI: 10.1016/j.rser.2014.11.101.

[58] S. Howroyd and R. Chen. “Powerpath controller for fuel cell & battery hybridisation”. In: *International Journal of Hydrogen Energy* 41.7 (2016), pp. 4229–4238. DOI: 10.1016/j.ijhydene.2016.01.038.

[59] B. Lee et al. “Power managements of a hybrid electric propulsion system for UAVs”. In: *Journal of Mechanical Science and Technology* 26 (2012), pp. 2291–2299. DOI: 10.1007/s12206-012-0601-6.

[60] T. Lei et al. “State of art on energy management strategy for hybrid-powered unmanned aerial vehicle”. In: *Chinese Journal of Aeronautics* 32.6 (2019), pp. 1488–1503. DOI: 10.1016/j.cja.2019.03.013.

[61] L. Gao, Z. Jiang, and R. A. Dougal. “An actively controlled fuel cell/battery hybrid to meet pulsed power demands”. In: *Journal of Power Sources* 130.1 (2004), pp. 202–207. DOI: 10.1016/j.jpowsour.2003.12.052.

[62] D. F. Waters and C. P. Cadou. “Engine-integrated solid oxide fuel cells for efficient electrical power generation on aircraft”. In: *Journal of Power Sources* 284 (2015), pp. 588–605. DOI: 10.1016/j.jpowsour.2015.02.108.

[63] J. Y. Hung and L. F. Gonzalez. “On parallel hybrid-electric propulsion system for unmanned aerial vehicles”. In: *Progress in Aerospace Sciences* 51 (2012), pp. 1–17. DOI: 10.1016/j.paerosci.2011.12.001.

[64] E. Baharozu, G. Soykan, and M. B. Ozerdem. “Future aircraft concept in terms of energy efficiency and environmental factors”. In: *Energy* 140 (2017). Advanced Energy Technologies in Aviation, pp. 1368–1377. DOI: 10.1016/j.energy.2017.09.007.

[65] “Boeing fuel cell plane in manned aviation first”. In: *Fuel Cells Bulletin* 2008.4 (2008), p. 1. DOI: 10.1016/S1464-2859(08)70146-9.

[66] “First flight of DLR’s HY4 fuel cell light aircraft”. In: *Fuel Cells Bulletin* 2016.10 (2016), p. 1. DOI: 10.1016/S1464-2859(16)30261-9.

[67] “AeroVironment flies world’s first hydrogen powered plane”. In: *Fuel Cells Bulletin* 2005.9 (2005), pp. 2–3. DOI: 10.1016/S1464-2859(05)70731-8.

[68] T. H. Bradley et al. “Development and experimental characterization of a fuel cell powered aircraft”. In: *Journal of Power Sources* 171.2 (2007), pp. 793–801. DOI: 10.1016/j.jpowsour.2007.06.215.

[69] M. K. Furrutter and J. Meyer. “Small fuel cell powering an unmanned aerial vehicle”. In: *IEEE AFRICON 2009*. Nairobi, Kenya, Sept. 2009. DOI: 10.1109/AFRCON.2009.5308096.

[70] M. Dudek et al. “Hybrid fuel cell–battery system as a main power unit for small unmanned aerial vehicles (UAV)”. In: *International Journal of Electrochemical Science* 8.6 (2013), pp. 8442–8463.

[71] K. Kim et al. “Fuel cell system with sodium borohydride as hydrogen source for unmanned aerial vehicles”. In: *Journal of Power Sources* 196.21 (2011). Fuel Cells Science & Technology 2010, pp. 9069–9075. DOI: 10.1016/j.jpowsour.2011.01.038.

[72] A. Nishizawa et al. “Fuel cell and Li-ion battery direct hybridization system for aircraft applications”. In: *Journal of Power Sources* 222 (2013), pp. 294–300. DOI: 10.1016/j.jpowsour.2012.09.011.

[73] D. Verstraete et al. “Characterisation of a hybrid, fuel-cell-based propulsion system for small unmanned aircraft”. In: *Journal of Power Sources* 250 (2014), pp. 204–211. DOI: 10.1016/j.jpowsour.2013.11.017.

[74] B. Lee et al. “The flight test and power simulations of an UAV powered by solar cells, a fuel cell and batteries”. In: *Journal of Mechanical Science and Technology* 28 (2014), pp. 399–405. DOI: 10.1007/s12206-013-0936-7.

[75] Y. Zhou et al. “Design and Implementation of UAV Based on Fuel Cell Power Supply”. In: *Communications, Signal Processing, and Systems*. Ed. by Q. Liang et al. Singapore: Springer Singapore, 2022, pp. 1027–1032. DOI: 10.1007/978-981-19-0390-8_129.

[76] S. Eelman, I. del Pozo y de Poza, and T. Krieg. “Fuel Cell APU’s in Commercial Aircraft – an Assessment of SOFC and PEMFC Concepts”. In: *24th Congress of International Council of the Aeronautical Sciences* (Aug. 2004).

[77] Airgas. *Safety Data Sheet - Hydrogen*. Version 1.01. Nov. 2020.

[78] Troy Hasanen. *Safe Work Procedure (SWP – 002) - Compressed Gas Cylinder Safe Handling and Use*. https://www.uvic.ca/ohse/assets/docs/laboratory/swp002_compressed.gas.cylinder.use.pdf. Last accessed on 13.05.2022. Nov. 2019.

[79] Heliocentris Energy Systems GmbH. *Operation Guide - HP 600 Fuel Cell System*. third edition, January 2008.

[80] How To Mechatronics. *How Brushless Motor and ESC Work*. https://howtomechatronics.com/how-it-works/how-brushless-motor-and-esc-work/. Last accessed on 16.06.2022. 2019.

[81] L. Machado, J. Matlock, and A. Suleman. “Experimental evaluation of a hybrid electric propulsion system for small UAVs”. In: *Aircraft Engineering and Aerospace Technology* 92.5 (2019), pp. 727–736. DOI: https://doi.org/10.1108/AEAT-06-2019-0120. URL: https://www.emerald.com/insight/content/doi/10.1108/AEAT-06-2019-0120/full/html.

[82] A. Beagley et al. *Mech 400 - Design Project Final Report Package*. Team 3, Professor Dr. Curran Crawford, TA Mehran Farhadmanesh. Apr. 2020.

[83] C. Brisebois et al. *Mech 400 - Hybrid Test Bench Dynamometer Final Report*. Aug. 2021.

[84] J. Farinha. *On the Design and Study of a Parallel Hybrid Electric Propulsion Rig for UAVs*. Master’s thesis, Instituto Superior Técnico. Oct. 2022.

[85] M. Råberg-Hellsing and C. Kaijser. *Specification of Test Procedures for Polymer Electrolyte Fuel Cell Stacks*. June 2004.

[86] P. Sharikov. *Fuel Cell Hybrid-Electric Propulsion for Unmanned Aerial Vehicles*. Honours thesis, Department of Engineering, University of Victoria. Aug. 2021.

[87] HyperPhysics, Georgia State University. *Electrical Wire Gauges*. http://hyperphysics.phy-astr.gsu.edu/hbase/Tables/wirega.html. Last accessed on 14.09.2022. 2016.

[88] M. H. Nehrir and C. Wang. *Modeling and Control of Fuel Cells: Distributed Generation Applications*. John Wiley & Sons, Inc., 2009.

[89] iFlight. *XING2 1404 Toothpick Ultralight Build (unibell)*. https://shop.iflight-rc.com/quad-parts-cat20/motors-cat26/xing2-motors-cat334/xing2-1404-toothpick-ultralight-build-unibell-pro1482. Last accessed on 30.08.2022.

[90] E-flite. *Power 46 Brushless Outrunner Instructions*. https://www.horizonhobby.com/on/demandware.static/-/Sites-horizon-master/default/dw50225888/Manuals/EFLPower46OutrunnerInstruct pdf. Last accessed on 30.08.2022.

[91] AXI MODEL MOTORS s. r. o. *AXI 2826/10 GOLD LINE V2 LONG*. https://www.modelmotors.cz/product/detail/480/. Last accessed on 30.08.2022.

[92] Universidade de São Paulo. *Propagação de incertezas*. https://edisciplinas.usp.br/pluginfile.php/1740045/mod_resource/content/1/incerteza.pdf. Last accessed on 30.08.2022.

[93] S. de Almeida Pedro. *Sizing and Integration of an Electric Propulsion System for a VTOL UAV*. Marter's thesis, Instituto Superior Técnico. Dec. 2020.

[94] Doosan Mobility Innovation. *DM15/DP15 : Powerpack : Doosan Mobility Innovation*. https://www.doosanmobility.com/en/products/powerpack-dm15/. Last accessed on 13.10.2022.

[95] Honeywell Aerospace. *600U HYDROGEN FUEL CELL*. N61-3014-000-000 — 07/21. 2021.

[96] Intelligent Energy. *IE-SOAR 800W second generation*. https://www.intelligent-energy.com/wp-content/uploads/2022/09/ie-soar-800w-gen2.pdf. Last accessed on 13.10.2022.

[97] H3 Dynamics. *Hydrogen Fuel Cell Systems by H3 Dynamics — Super Lighweight and Power Dense For Air Mobility Needs*. https://www.h3dynamics.com/hydrogen-fuel-cell-systems-for-air-mobility. Last accessed on 13.10.2022.

[98] H3 Dynamics. *H3D Brochure Complete 2022 V8*. https://www.h3dynamics.com/_files/ugd/3029f7_db7f1517df744509b837916c4d939ae3.pdf. Last accessed on 17.10.2022. 2022.

Appendix A

Experimental Test Cards

Cylinder Bubble Test

Project:
Aircraft S/N:
Date:
Test lead:
One Up:

#	TPname	Description	Complete	Notes
1	Safety Discussion	Inspect all elements for damage, clean debris at connections, ground cylinder, use PPE. Keep sources of ignition away, have designated person for fire extinguisher (+ backup), ventilated area (open hangar door), other CfAR personnel informed of evacuation procedures		
2	Test Points Discussion	Check test points name and location		
3	Connect Regulator	No flow, all valves closed (regulator counter clockwise), do not use teflon tape		
4	**Pressure Test Regulator**			
4.1	Check source pressure	2400 psi/165.5 bar		Pressure observed: [ ]
4.2	Check regulator pressure	0 bar		Pressure observed: [ ]
4.3	Check outlet valve closed	Close it if necessary		
4.4	Turn regulator clockwise to adjust pressure	Adjust to 8 bar/116 psi (FC inlet 2-8 bar)		Pressure observed: [ ]
4.5	Close cylinder source valve			
4.6	Check if it maintains the pressure	8 bar/116 psi in regulator (for at least 60 seconds)		Maintained pressure? [ ]
⚠ CAUTION ⚠	**Do not continue if leak is identified**	Close source cylinder valve		
5	**If Pass,** Bubble Test Points 0-9	Apply water-soap solution to the test points, wait for a few minutes and check for bubbles		Bubble test passed? [ ]
⚠ CAUTION ⚠	**Do not continue if leak is identified**	Close source cylinder valve		
6	**If Pass,** Open Cylinder Source	Keep regulator at 8 bar, and check 8 bar		
7	Open Outlet Valve, Bubble Test 10-15	Same procedure as #5		Bubble test passed? [ ]
8	Close Source Cylinder Valve	Leave regulator and outlet valve open		
9	Depress Parker	To drain hydrogen inside the regulator, press the Parker to vent		
10	Close Outlet, Close Regulator	Regulator counter clockwise		
11	Remove Regulator			
12	Install Hydrogen Safety Cap			

NOTES

Date Completed:
Test lead signature:
One up signature:

Bubble Test Card

Project:
Aircraft S/N:
Date:
Test lead:
One Up:

Test Point #	Name	Part	BT Performed	BT Passed	Notes
0	Source stem	Hydrogen Cylinder, Praxair HY5.0UH T	[ ]	[ ]	
1	Source outlet	Hydrogen Cylinder, Praxair HY5.0UH T	[ ]	[ ]	
2	Regulator inlet thread	Regulator, Harris HP721-125-350-BE KH1130	[ ]	[ ]	
3	Source sink	Regulator, Harris HP721-125-350-BE KH1130	[ ]	[ ]	
4	Source pressure gauge stem	Regulator, Harris HP721-125-350-BE KH1130	[ ]	[ ]	
5	Outlet pressure gauge stem	Regulator, Harris HP721-125-350-BE KH1130	[ ]	[ ]	
6	Regulator outlet	Regulator, Harris HP721-125-350-BE KH1130	[ ]	[ ]	
7	Low pressure vent thread	Regulator, Harris HP721-125-350-BE KH1130	[ ]	[ ]	
8	High pressure vent thread	Regulator, Harris HP721-125-350-BE KH1130	[ ]	[ ]	
9	Outlet valve upstream	Regulator, Harris HP721-125-350-BE KH1130	[ ]	[ ]	
10	Outlet valve downstream	Regulator, Harris HP721-125-350-BE KH1130	[ ]	[ ]	
11	Outlet swage	Hose	[ ]	[ ]	
12	Fuel cell swage	Hose	[ ]	[ ]	
13	Hose parker	Hose	[ ]	[ ]	
14	Fuel cell parker	Fuel Cell System, Heliocentris HP 600	[ ]	[ ]	
15	GSM inlet thread	Fuel Cell System, Heliocentris HP 600	[ ]	[ ]	
16	Flow meter outlet	Fuel Cell System, Heliocentris HP 600	[ ]	[ ]	
17	Pressure regulator inlet	Fuel Cell System, Heliocentris HP 600	[ ]	[ ]	
18	Pressure regulator outlet	Fuel Cell System, Heliocentris HP 600	[ ]	[ ]	
19	FC hydrogen inlet	Fuel Cell System, Heliocentris HP 600	[ ]	[ ]	
20	FC hydrogen outlet	Fuel Cell System, Heliocentris HP 600	[ ]	[ ]	
21	Purge valve inlet	Fuel Cell System, Heliocentris HP 600	[ ]	[ ]	

NOTES

Date Completed:
Test lead signature:
One up signature:

Standard Cycle

Project:
Aircraft S/N:
Date:
Test lead:
One Up:

#	TPname	Description	Complete	Notes
1	Safety Discussion	Inspect all elements for damage, clean debris at connections, ground cylinder and FC system, use PPE. Keep sources of ignition away, have designated person for fire extinguisher (+ backup), ventilated area (open hangar door), other CfAR personnel informed of evacuation procedures		After a long time without use check battery charge (12V) Check cooling water level and conductivity every 6 months/50 hours of use
2	Test Procedure Discussion	Check test points name and location, review test procedure		
3	**If Necessary,** Refill Cooling Circuit	Use demineralized water (conductivity < 1µS/cm)		
4	Connect Hydrogen Supply	Open necessary valves in the cylinder and regulator Inlet pressure between 2 and 8 bar		Pressure observed: [ ]
5	Start the Fuel Cell System	Press start button for 5 seconds Wait for the start up procedure to be finished		Purge valve will open until the voltage level ok, make sure there is proper ventilation After a long time without use it may take a longer time to reach full power due to dry FC membranes
⚠ CAUTION ⚠	**If an error occurs, the start up procedure will stop**	Check the error message and follow the procedure in the HP 600 operation guide		
6	**If Necessary,** Bubble Test Hydrogen Circuit Test Points 14-21	Apply water-soap solution to the test points, wait for a few minutes and check for bubbles. Be careful to keep the electronic components below dry		If a leak is suspected or after a long time without use a bubble test should be performed Bubble test passed? [ ]
⚠ CAUTION ⚠	**Do not continue if leak is identified**	Close source cylinder valve. Seal the leak if possible, otherwise contact the manufacturer		
7	Connect/Switch On the Load			
8	Warm Up the FC Stack to the Operating Temperature (at least 47°C)	Operate at 60% (27 A unregulated; 25.2 A regulated) of the maximum continuous current, preferably at the reference condition (alternatively at the condition of the test)		Current observed: [ ] Temperature reached: [ ]
9	Wait 30 Minutes	Operate at the rated operating temperature in the same conditions as above		30 minutes complete? [ ]
Current-Voltage Polarization Curve		For the first time, repeat the test 3 times to check the results Carry out standard cycle regularly to check if the FC stack is degrading		
10	Set Current to the Obtained When Minimum Average Cell Voltage is Reached	Operate the stack until temperature distribution is stable, and read current and voltage under stationary conditions [(ΔU/U0)/Δt ≤ 10-4 sec-1]		Fill in Test Card [ ]
11	Decrease the Current in Steps of 50mA/cm2 (6.3 A)	Read the measurements like above, repeat until OCV is reached		Fill in Test Card [ ]
12	Set the Average Cell Voltage to 0.7V/cell (16.8 V)	Measure the current, when temperature distribution is stable		Current observed: [ ]
13	Set OCV Conditions	Read voltage after 2 minutes		Voltage observed: [ ]
14	Turn Off the Load			
15	Switch Off the Fuel Cell System	Push the stop button The shut-down sequence takes 250 seconds to be completed (4 minutes and 10 seconds)		Shut-down complete? [ ]
16	**Close Hydrogen Supply**			
16.1	Shut Off Cylinder Valve	Leave regulator and outlet valve open		
16.2	Disconnect Hose			
16.3	Depress the Parker	To drain hydrogen inside the regulator, press the Parker to vent		
16.4	Close Regulator Valves and Remove It	Regulator counter clockwise		
16.5	Install Cylinder Safety Cap			

NOTES

Date Completed:
Test lead signature:
One up signature:

Polarization Curve Test Card

Project:
Aircraft S/N:
Date:
Test lead:
One Up:

Setpoint Stack Temperature [°C]:
Setpoint Recirculation Humidity [%]:

Test Point #	Current [A]	Voltage [V]	Power [W]	Current Density [A/cm2]	Average Cell Potential [V/cell]	Cell Power [W]		
Nominal Conditions		16.8	0	0	0.7	0		
OCV Conditions	0		0	0	0	0		
1			0	0	0	0		
2			0	0	0	0		
3			0	0	0	0		
4			0	0	0	0		
5			0	0	0	0		
6			0	0	0	0		
7			0	0	0	0		
8			0	0	0	0		
9			0	0	0	0		
10			0	0	0	0		
11			0	0	0	0		
12			0	0	0	0		
13			0	0	0	0		
14			0	0	0	0		
15			0	0	0	0		
16			0	0	0	0		
17			0	0	0	0		
18			0	0	0	0		
19			0	0	0	0		
20			0	0	0	0		

NOTES

Date Completed:
Test lead signature:
One up signature: